Friedrich-Alexander-Universität Erlangen-Nürnberg
Technische Fakultät

Chair of Fluid Mechanics(LSTM)
Prof. Dr. Sc. Techn. Philipp Schlatter

Sensitisation and Analysis of the Differential Reynolds Stress Model SSG/LRR − ω for flows with mean-streamline curvature using local Richardson number

prepared by

Laxmi Srinivas Vellala

at

Institute of Aerodynamics and Flow Technology, DLR

submitted to LSTM in fulfilment of the requirements for the Master's degree in Computational Engineering

Erklärung:

Ich versichere, dass ich die Arbeit ohne fremde Hilfe und ohne Benutzung anderer als der angegebenen Quellen angefertigt habe und dass die Arbeit in gleicher oder ähnlicher Form noch keiner anderen Prüfungsbehörde vorgelegen hat und von dieser als Teil einer Prüfungsleistung angenommen wurde. Alle Ausführungen, die wörtlich oder sinngemäß übernommen wurden, sind als solche gekennzeichnet.

Erlangen, den 02.05.2024

Laxmi Srinivas Vellala

Abstract

The present study focuses on the effects of streamline curvature in curved turbulent boundary layers. Bradshaw's gradient Richardson number was used to identify zones of convex and concave curvatures. A Galilean-invariant version of Richardson number (Ri_{local}) augmented by the direction information of Spalart & Shur's [43] rotation/curvature correction framework was derived. The behaviour of the Richardson number was investigated by conducting a sensitivity study by parameterizing the Monson's [23] U-duct test case for varying curvature magnitude. The capability of Ri_{local} to identify the sign and magnitude of curvature is demonstrated for different curvature magnitudes of U-duct test case.

Suitable test cases (both convex and concave curvature) from the experiments in the literature namely Monson (1990), Gillis & Johnston (1981) and So & Mellor (1972) were chosen. The geometries were built and CFD setups were developed and validated using RANS models. Using the validation cases, rotation/curvature corrections to SA, SST were compared and the SSG/LRR-ω was assessed for convex and concave curvatures. It was determined that SSG/LRR-ω gives better agreement with the experimental data than SA-RC and SST-RC for the convex curved turbulent boundary layers. For the concave curvature test case, SSG/LRR-ω gives a good agreement with the trough region of Taylor-Görtler vortex where effects of these longitudinal vortices are minimal. The double peak structure of Reynolds shear stress in longitudinal vortices on a concave wall was not captured by any of the RANS models in the present work.

Moreover, different redistribution models namely Speziale-Sarkar-Gatski (SSG), Launder-Reece-Rodi (LRR) and SSG/LRR-ω were compared for convex and concave curvatures where SSG/LRR-ω gives the best agreement with the experimental profiles of mean-velocity, Reynolds shear stress and Reynolds stress anisotropy. The Generalized Gradient Diffusion Hypothesis (GGDH) and the Simple Gradient Diffusion Hypothesis (SGDH) were examined for both convex and concave turbulent boundary layers. GGDH gives better agreement with the experimental data compared to SGDH for different Reynolds stress models.

Based on the insights from the validation cases, prospects for curvature sensitsation of SSG/LRR-ω were explored. Modifications to the turbulent transport term using the Ri_{local} were investigated based on the comments from Zeman [56]. Trials were conducted to modify the production of length scale P_ω, thus modifying dissipation thereby and further changing the production of Reynolds shear stress. Insights into further modification of SSG/LRR-ω for complex flows were provided.

Acknowledgements

Firstly, I would like to express my sincere gratitude to my thesis advisor Dr. Tobias Knopp from $C^2A^2S^2E$ department at DLR Göttingen for guiding me through the intricacies of rotation and curvature effects in turbulence. His constant support and supervision were highly influential in carrying out this work at DLR. Regular discussion with him have helped me understand the complicated concepts of turbulence and navigate through the challenges that came along with it.

I am grateful to Dr. Cornelia Grabe, the Head of $C^2A^2S^2E$ department and Dr. Andreas Krumbein, the Head of 'Turbulence and Transition Modelling' research group at $C^2A^2S^2E$ for providing me an opportunity to pursue my Master Thesis at the Institute of Aerodynamics and Flow Technology, DLR, Göttingen.

I am happy that I have found an amazing group of colleagues: Niels, Keerthana, El Rawy, Roberto, Deepak, Sebastian, Daniela, Marius, Jonathan, Helena etc. who helped me in this journey. I can't forget the long discussions we had during lunch break or scribbling on the coffee sheet in the kitchen questioning our understanding of Aerodynamics and Turbulence.

Besides my DLR colleagues, I am grateful to my internal supervisor at FAU, Dr. Manuel Münsch for his constant support from the university in courses, seminar and the thesis.

Finally, I would like to express my gratitude to my family for their continuous support and love. Their encouragement helped me to pursue my goals.

Contents

List of Figures

List of Tables

Chapter 1

Introduction

1.1   Motivation

Fluid turbulence is one of the most complicated topics which has kept both physicists and engineers busy for several decades. Turbulent flow simulation is one of the most complex problems in engineering simulations. These simulations come at high computational cost. In fact, fluid flow simulation is one of the top 10 problems to consume CPU time in supercomputers all around the world. Accurately simulating turbulence involves resolving all the scales of fluid motion down to the smallest scale. This is expensive to several problems such as flow over an aircraft wing in high-lift configuration. So, there is an ever-growing need to find cost-efficient techniques for simulating turbulent flows. The main motivation of the present work is to make turbulence model accurate for such flow conditions. Two important flow features of an aircraft wing in high-lift configuration are adverse pressure-gradient (APG) flow and curved streamlines. Flows with streamline curvature are very common in nature and curvature has considerable influence on turbulence production. Convex surface curvature suppresses turbulence and concave curvature amplies it.

1.2   Literature review

Effects of surface curvature has been extensively studied in the history of research in fluid dynamics dating back to Ludwig Prandtl [30] who investigated the effects of stabilizing forces on turbulence to devise modifications to Mixing-length model. Wattendorf [53] identified strong influence of curvature on velocity distribution, increased mixing at the outer walls of curved channels and reduced mixing at the inner wall.

Görtler [15] identified an instability in laminar boundary layers on concave walls due to three-dimensional perturbations. Later several experiments [39], [3] have confirmed the existence of Görtler on concave walls even in fully turbulent flows. A detailed treatise of Görtler vortices is provided by Saric [33]. Patel [28] performed experiments on a 90° curved duct and report quite significant effects of longitudinal surface curvature on the development of turbulent boundary layer.

So & Mellor [39] performed experiments on convex and concave curved turbulent boundary layer in an almost 150° curved duct with surface curvature magnitude δ/R_c (ratio of boundary layer thickness δ to radius of the curvature R_c) of 0.075 at convex wall and 0.1 at concave wall. The drop in static pressure was maintained at 23% of reference dynamic head at the onset of the curvature. Distinctive longitudinal vortices were observed in the concave turbulent boundary layer at high curvature. Ramaprian & Shivaprasad [31] investigated two-dimensional turbulent boundary layer characteristics experimentally for mild curvatures $\delta/R_c \approx 0.013$ and noted that the region close to the convex wall was not affected significantly but the outer part of the turbulent boundary layer was sensitive to even mild curvature. Gillis & Johnston [13] performed experiments on convex curved turbulent boundary layers using a 90° curved duct at $\delta/R_c \approx 0.1$ with static-pressure drop less than 5% of the reference dynamic head at the onset of the curvature that makes it an almost Zero-

Pressure-Gradient (ZPG) curvature case. Later Monson et al. [23] performed an experiment on a U-shaped curved channel at high curvature and Reynolds number of 10^5 and 10^6 based on duct height which was used to validate rotation-corrections of several RANS models.

Bradshaw [4] proposed an algebraic analogy between streamline curvature and buoyancy thus giving a version of gradient Richardson number that identifies and quantifies streamline curvature. Hellsten [16] provided a Galilean-invariant version of Richardson number using the magnitudes of vorticity, strain-rate tensors and used it to sensitise Menter's Shear Stress Transport (SST) model. Ströer & Knopp [46] have derived a Galilean-invariant formulation for the Bradshaw's Richardson number.

In flows with streamline curvature, there exists a misalignment in the principal axes of Reynolds stress and turbulent strain-rate tensors. Knight & Saffman [18] provided an estimation of stress-strain misalignment angle in polar coordinates. Later, Spalart & Shur [43] developed this formulation into a Galilean-invariant framework to modify RANS turbulence models. This rotation/curvature correction was applied to Spalart-Allmaras (SA) turbulence model to make SA-RC which was validated using several test cases in Ref. [36]. Smirnov & Menter used the rotation/curvature correction of Spalart & Shur [43] to propose SST-RC [38]. Durbin [10] provides a comprehensive review of rotation/curvature corrections to several scalar turbulence closure models. Zeman [56] studied modelling of Reynolds stress closures particularly for modelling turbulent wing-tip vortices in a far-field region of vortex evolution.

Cecora et al. [7] developed the SSG/LRR-ω Reynolds stress model by blending Speziale-Sarkar-Gatski (SSG) [44] and Launder-Reece-Rodi (LRR) [21]. Knopp [19] presented a modification to SSG/LRR-ω model for turbulent boundary layers in adverse pressure gradient. Ströer & Knopp [45] explored modifications to SSG/LRR-ω model using a Galilean-invariant Richardson number from Ref. [46].

1.3   Organisation

In the present work, chapter 2 explains the governing equations of fluid dynamics, an introduction to turbulence modelling with a few well known turbulence models in CFD and the computational tools used.

In chapter 3, the quantitative and qualitative effects of streamline curvature, structure of curved turbulent boundary layers and a deeper insight into turbulence in flows is streamline curvature is discussed. In this chapter, the significance of the Richardson number is for curved flows, the calculation/derivation of different versions of Richardson number is presented. Some of the prominent curvature modifications in RANS turbulence models are explained.

In chapter 4, experiments from literature and development of simulation setup is discussed which covers different techniques employed to replicate complex experimental setups and the validation of geometries is shown. One of these validation test case is taken and the parameter of Richardson number is analysed. Sensitivity studies have been performed to understand the behaviour of Richardson number in different types of curvatures and various curvature magnitudes which are discussed in chapter 5.

Chapter 6 validates SSG/LRR-ω for the test cases and compares it's performance to other prominent curvature corrected RANS models like SA-RC and SST-RC. Using the profiles of mean-velocity and turbulent shear stress from the test cases, the effect of different redistribution models for the pressure-strain correlation and the effect of diffusion model for turbulent transport is debated. Using the findings from test cases, some implications on how to modify SSG/LRR-ω are specified.

In chapter 7, prospects for curvature modifications to SSG/LRR-ω are understood by using different trials to modify the turbulence model. Chapter 8 concludes the thesis by providing a summary of the work done, main conclusions from the discussions and some future direction to work on this problem.

Chapter 2

Physical models and Numerical setup

The mathematical model for compressible viscous fluid flow in aerospace applications are the compressible Navier-Stokes equations. These equations describe the space-time evolution of density, momentum and energy of the fluid based on conservation laws. The solution of the Navier-Stokes equations becomes turbulent if the Reynolds number is above some critical value. There are two approaches for tackling the problem of turbulence.

On the one hand, there are scale resolving simulations. They resolve the turbulent motion down to some small scale, which can be the Kolmogorov scale (Direct Numerical Simulation) or a used defined length scale in the inertial subrange (Large-Eddy Simulation). Scale-resolving approaches are based on the Navier-Stokes equations. Some LES methods add a so-called subgrid-scale formulation to model physical effects smaller than the smallest resolved scales.

On the other hand, there are statistical turbulence models. They seek an approximation to a statistically-averaged solution of the Navier-Stokes equations. The statistically averaged Navier-Stokes equations involve an additional term, the so-called Reynolds stress tensor. Hence there are more unknowns than equations and a closure model arises. The Reynolds stress tensor describes the statistically-averaged effects of the fluctuating turbulent motion on the mean flow. There are basically two approaches to account for the Reynolds stresses. The first approach uses the so called by some closure model for the Reynolds stress tensor directly, called models based on the turbulent-viscosity hypothesis or Boussinesq assumption. The most complete approach of practical relevance today is to solve the system of transport equations for the Reynolds stress tensor. However, this equation also requires for some closure models.

This chapter describes the RANS models used in this work and provides the necessary background for the following sections.

2.1   Navier-Stokes equations for Compressible flows

This section describes the Navier-Stokes equations for compressible flows. The governing equations for compressible Newtonian fluids can be written in tensorial form as:

$$\frac{\partial \rho}{\partial t} + \frac{\partial (\rho \tilde{u}_i)}{\partial x_i} = 0 \tag{2.1}$$

$$\frac{\partial (\rho \tilde{u}_i)}{\partial t} + \frac{\partial (\rho \tilde{u}_i \tilde{u}_j)}{\partial x_j} = -\frac{\partial \tilde{p}}{\partial x_i} + \frac{\partial \tau_{ij}}{\partial x_j} + \rho g_i \tag{2.2}$$

$$\frac{\partial (\rho E)}{\partial t} + \frac{\partial (\rho \tilde{u}_j (E + p/\rho))}{\partial x_j} = \frac{\partial (\tilde{u}_i \tau_{ij})}{\partial x_j} + \frac{\partial}{\partial x_j} \left(k \frac{\partial T}{\partial x_j} \right) \tag{2.3}$$

9

$$\tilde{p} = \rho R T \tag{2.4}$$

Here $\tilde{u}$ and $\tilde{p}$ are the instantaneous velocity and pressure; g_i is the body force, E is the energy, k is the coefficient of thermal conductivity, T is the temperature, ρ is the density, R is the specific gas constant. τ_{ij} is the viscous stress tensor which is proportional to the rate of deformation in a Newtonian fluid and is written as:

$$\tau_{ij} = \mu \left(\frac{\partial \tilde{u}_i}{\partial x_j} + \frac{\partial \tilde{u}_j}{\partial x_i} \right) - \frac{2}{3} \mu \delta_{ij} \frac{\partial \tilde{u}_k}{\partial x_k} \tag{2.5}$$

where μ is the coefficient of dynamic viscosity. 2.4 shows the equation of state obtained through the thermodynamic equilibrium assumption. 2.1, 2.2 and 2.3 are the equations of conservation of mass, momentum and energy respectively.

2.2 Navier-Stokes equations for Incompressible flows

Present study concentrates on low Mach number (Ma) flows. Flows with Ma < 0.3 can be considered as incompressible flows where the density changes are quite negligible due to the relative pressure changes being very low. For an incompressible Newtonian fluid, ρ, μ, k are independent of temperature. Due to the continuity assumption mentioned in 2.6, momentum and energy equations decouple when $\tilde{p} \frac{\partial \tilde{u}_j}{\partial x_j} = 0$. For fluid dynamic application where there is negligible heat transfer, temperature changes, the energy equation can be ignored. Therefore, we can rewrite the Navier-Stokes equations for an incompressible Newtonian fluid as follows:

$$\frac{\partial \tilde{u}_i}{\partial x_i} = 0 \tag{2.6}$$

$$\frac{\partial \tilde{u}_i}{\partial t} + \tilde{u}_j \frac{\partial \tilde{u}_i}{\partial x_j} = -\frac{1}{\rho} \frac{\partial \tilde{p}}{\partial x_i} + \nu \frac{\partial^2 \tilde{u}_i}{\partial x_j \partial x_j} + \rho g_i \tag{2.7}$$

2.3 Turbulence and its modelling in fluid flows

For all kinds of flows observed in engineering, flows are stable with parallel streamlines only for low Reynolds Number ($Re = UL/\nu$ where U is the characteristic mean flow velocity, L is the characteristic length scale of mean flow and ν is the kinematic viscosity). When Reynolds number increases, flow undergoes several complex stages of Transition such as distortion of Tollmien–Schlichting waves, evolution of hairpin vortices, formation and merging of turbulent spots which finally leads to a Turbulent flow. A fully turbulent flow comprises of irregular, chaotic fluid motion with velocity and pressure fluctuations that lead to increased mixing, momentum and energy transport. The main features of a fully turbulent flow are: Velocity fluctuations, Vorticity, Three-dimensional nature, Mixing, Energy cascade across scales, Diffusivity and Dissipation [48].

Navier-Stokes equations can be used to simulate a fully turbulent flow. In fact, problem of turbulence is the complete solution to these equations. But, one needs to run the discretized version of Navier-Stokes equations using numerical methods for the finest grid of an engineering system on massively parallel supercomputer to obtain the solution of flow field. The requirement of finest grid poses a problem of computational labour. One needs to discretize the domain into very small sub-domains such that all scales of fluid motion are captured. This requirement goes higher with the Reynolds number. So, an accurate solution of flow field for a aircraft at high-lift configuration might take more than a life time. Simulations of a turbulent flows are one of the top energy demanding computations which are done on any supercomputer. Data centers account for more than 200 Terawatt hours of electricity consumption globally. This pushes the need to further model Turbulence such that one can obtain near-accurate flow fields of velocity, pressure on coarses grids instead of resolving all scales of a turbulent flow.
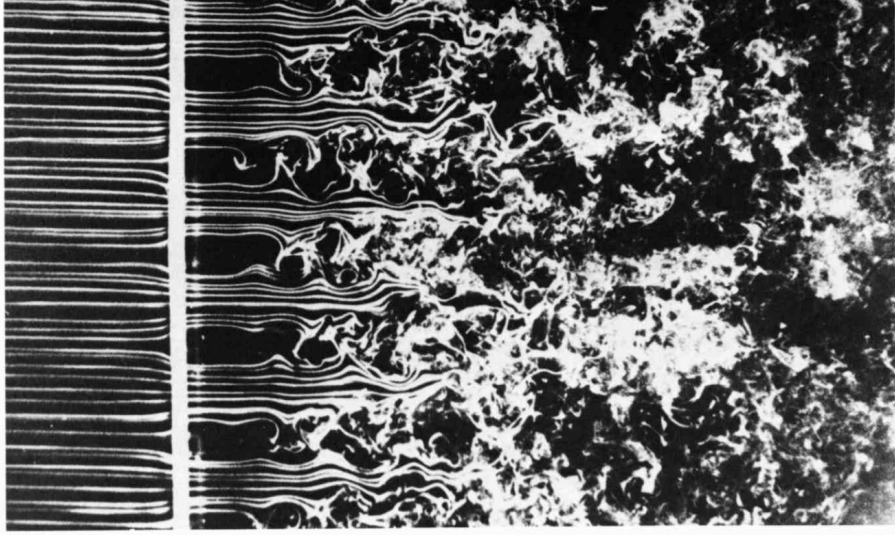
Figure 2.1: Grid generated turbulence due to the instability of shear layers downstream a plate with square perforations. [50]

Luckily, the chaotic motion and fluctuations of a turbulent flow are statistical in nature. The averages of these fluctuating quantities can be understood and modelled. When direction computation usually referred as Direct Numerical Simulation (DNS) hit the computational capacity, engineers and scientists got interested in modelling turbulence using statistical measurement techniques.

2.4 Reynolds-Averaged Navier-Stokes equations

In 1895, Osborne Reynolds proposed the decomposition of fluid flow velocity ($\tilde{u}$) and pressure into time-averaged mean component ($\bar{u}_i$) and a fluctuating component (u'_i) [32] with an aim to obtain a set of equations which can describe the averaged properties of a turbulent flow.

$$\tilde{u}_i = U_i + u_i$$
$$U = \lim_{T \to \infty} \frac{1}{T} \int_{t_0}^{t_0+T} \tilde{u}\, dt \tag{2.8}$$

Here, the flow is assumed to have a property that the mean flow field U becomes independent of time t_0 for large time period T which is called a statistically steady turbulent flow. The ergodic theorem states that the mean solution can be obtained by time-averaging a single flow problem. The ensemble averaging filter has the following properties for instantaneous variables f, g:

$$
\begin{aligned}
Linearity(c \in \mathbb{R}) \quad &: \quad \overline{cf} = c\overline{f} \\
Distributive \quad &: \quad \overline{f} + \overline{g} \ and \ \overline{f.g} = \overline{f}.\overline{g}, \\
Projection\, identity \quad &: \quad \overline{\overline{f}} = \overline{f} \\
Average\, of\, fluctuations \quad &: \quad \overline{f'} = 0 \\
Commutative \quad &: \quad \overline{\frac{\partial f}{\partial x}} = \frac{\partial \overline{f}}{\partial x} \ and \ \overline{\int f ds} = \int \overline{f} ds \\
Average\, of\, a\, product \quad &: \quad \overline{fg} = \overline{(\bar{f} + f')(\bar{g} + g')} = \overline{f}\overline{g} + \overline{f'g'}
\end{aligned} \tag{2.9}
$$

By applying the Reynolds decomposition to the mass and momentum equations, we get:

$$\frac{\partial (U+u)_i}{\partial x_i} = 0$$

$$\frac{\partial (U+u)_i}{\partial t} + (U+u)_j \frac{\partial (U+u)_i}{\partial x_j} = -\frac{1}{\rho}\frac{\partial (P+p)}{\partial x_i} + \nu \frac{\partial^2 (U+u)_i}{\partial x_j \partial x_j} + \rho g_i \qquad (2.10)$$

Now, the average of entire equation is taken by drawing a bar over each term while implementing the rules of averaging, we arrive at Reynolds-averaged Navier-Stokes(RANS) equations for an incompressible Newtonian fluid:

$$\frac{\partial U_i}{\partial x_i} = 0$$

$$\frac{\partial U_i}{\partial t} + U_j \frac{\partial U_i}{\partial x_j} = \rho g_i - \frac{1}{\rho}\frac{\partial P}{\partial x_i} + \nu \frac{\partial^2 U_i}{\partial x_j \partial x_j} - \frac{\partial \overline{u_i u_j}}{\partial x_j} \qquad (2.11)$$

After invoking the continuity in convective derivative, the new term $\overline{u_i u_j}$ appears which is termed as Reynolds stress. Although, this term comes from the convection part, the ensemble averaged effect of convection is diffusive and here momentum is being diffused through this additional term [11]. The mean flow equations(2.11) are unclosed due to more unknowns $(P, U_i, \overline{u_i u_j} : 1 + 3 + 3)$ and less equations (4) which is known as the turbulence closure problem. Majority of the field of Turbulence modelling revolves around defining the reynolds stress tensor $(\overline{u_i u_j})$. For a compressible flow, one must also account for density and temperature fluctuations. Favre-averaged Navier-Stokes equations [12, 55] which have a similar structure to the imcompressible form (2.11) are used to solve compressible turbulent flows. For most of the engineering problems, the intricate details of the velocity, pressure fluctuations and fine scales of motion are not necessary. Only the overall effect of all the fluctuations to the mean flow is required to determine quantities like Skin friction, Drag, Heat transfer coefficients etc. So, the majority of turbulence flow computation done by engineers in the industry were, are and will be based on RANS equations for the forseeable future. Therefore, it is necessary to further develop RANS equations for better flow predictions and applicability in wide range of complex engineering applications.

2.5 Turbulence models for RANS

From the Newton's law of viscosity, stress is directly proportional to the strain-rate in laminar flows. This results in a coefficient of proportionality which is the dynamic viscosity coefficient (μ), a property for a fluid. In 1877, Boussinesq proposed the hypothesis of direct proportionality between Reynolds (turbulent) stresses and mean-flow strain-rates. The coefficient of proportionality is the turbulent viscosity or eddy viscosity(μ_T), a property of the flow rather than the fluid.

$$-\overline{u_i u_j} = \nu_T \left(\frac{\partial U_i}{\partial x_j} + \frac{\partial U_j}{\partial x_i} \right) - \frac{2}{3}k\delta_{ij} \qquad (2.12)$$

where $k = (\overline{u_1^2} + \overline{u_2^2} + \overline{u_3^2})/2$ is the turbulent kinetic energy per unit mass and $\nu_T = \mu_T/\rho$ is the kinematic eddy viscosity [51]. All turbulence models which try to define the turbulent viscosity are known as Eddy viscosity models whereas the models which try to directly obtain the Reynolds stress are known as Reynolds Stress Models (RSM). Significant efforts have been made by the CFD research and development community to model the Reynolds stress tensor. These can be categorized based on the number of additional transport equations one needs to solve. Readers are encouraged to visit the NASA's Turbulence resource website [26] for the full list of up-to-date and best performing models for wide range of applications. Few of these turbulence models are predominantly used in the industry.

No. of additional transport equations	Name	References
Zero	Mixing Length	[29]
One	Spalart-Allmaras	[42, 1]
Two	$k - \varepsilon$	[20]
	$k - \omega$	[54]
	SST	[22]
Seven	Wilcox-RSM	[55]
	SSG/LRR-ω	[7]

Table 2.1: List of widely used Turbulence models

2.5.1 Spalart-Allmaras model

The Spalart-Allmaras turbulence model solves one transport equation for kinematic eddy viscosity parameter, $\hat{\nu}$ (here $\hat{\nu}$ was used instead of the original $\tilde{\nu}$ as tilde was used for instantaneous variables only in this chapter). It was originally developed for flows in aerospace applications which involve a wall-bounded flows. The eddy viscosity can be calculated from the kinematic eddy viscosity parameter by $\nu_T = \hat{\nu} f_{v1}$ where f_{v1} is the wall-damping function which becomes unity for high Reynolds numbers.

$$\frac{\partial \hat{\nu}}{\partial t} + U_j \frac{\partial \hat{\nu}}{\partial x_j} = c_{b1}(1 - f_{t2})\hat{S}\hat{\nu} - \left[c_{w1}f_w - \frac{c_{b1}}{\kappa^2}f_{t2}\right]\left(\frac{\hat{\nu}}{d}\right)^2 + \frac{1}{\sigma}\left[\frac{\partial}{\partial x_j}\left((\nu + \hat{\nu})\frac{\partial \hat{\nu}}{\partial x_j}\right) + c_{b2}\frac{\partial \hat{\nu}}{\partial x_i}\frac{\partial \hat{\nu}}{\partial x_i}\right]$$

$$f_{v1} = \frac{\chi^3}{\chi^3 + c_{v1}^3}, \quad \chi = \frac{\hat{\nu}}{\nu}, \quad \hat{S} = \Omega_{ij} + \frac{\hat{\nu}}{\kappa^2 d^2}f_{v2}$$

$$f_{v2} = 1 - \frac{\chi}{1 + \chi f_{v1}}, \quad f_w = g\left[\frac{1 + c_{w3}^6}{g^6 + c_{w3}^6}\right] \quad g = r + c_{w2}(r^6 - r)$$

$$r = min\left[\frac{\hat{\nu}}{\hat{S}\kappa^2 d^2}, 10\right], \quad f_{t2} = c_{t3}exp(-c_{t4}\chi^2), \quad \Omega_{ij} = \frac{1}{2}\left(\frac{\partial U_i}{\partial x_j} - \frac{\partial U_j}{\partial x_i}\right)$$

$$(2.13)$$

Here, ν is the molecular kinematic viscosity, $||\Omega||$ is the magnitude of vorticity, d is the distance from the field point to the nearest wall and the list of constants are: $c_{b1} = 0.1355$, $\sigma = 2/3$, $c_{b2} = 0.622$, $\kappa = 0.41$, $c_{w2} = 0.3$, $c_{w3} = 2$, $c_{v1} = 7.1$, $c_{t3} = 1.2$, $c_{t4} = 0.5$, $and\, c_{w1} = \frac{c_{b1}}{\kappa^2} + \frac{1+c_{b2}}{\sigma}$. The boundary conditions are $\hat{\nu}_{wall} = 0$, $\hat{\nu}_{farfield} = 3\nu_\infty\, to\, 5\nu_\infty$ [26]. Several modifications have been made to this model which include negative-viscosity (SA-neg), rotation, curvature corrections (SA-R95, SA-RC, SA-R23) and also with quadratic constitutive relation (SA-QCR) etc. Some of the prominent modifications to the Spalart-Allmaras model will be discussed in the further chapters.

2.5.2 Menter Shear Stress Transport(SST) model

A widely used 2 equation model based on blending on $k-\varepsilon$ and $k-\omega$ turbulence model. $k-\varepsilon$ model performs well in the free stream but unsatisfactory in the near-wall region inside the boundary layers with adverse pressure gradients. and $k-\omega$ gives good predictions in the boundary layers. In 1994, Menter proposed a blending approach in which $k-\omega$ is used inside the boundary layer and $k-\varepsilon$ is

used in the free stream region.

$$\frac{\partial \rho k}{\partial t} + \frac{\partial (\rho U_j k)}{\partial x_j} = P_k - \beta^* \rho \omega k + \frac{\partial}{\partial x_j}\left[(\mu + \sigma_k \mu_T)\frac{\partial k}{\partial x_j}\right]$$

$$\frac{\partial \rho \omega}{\partial t} + \frac{\partial (\rho U_j \omega)}{\partial x_j} = \frac{\gamma}{\nu_T} P_k - \beta \rho \omega^2 + \frac{\partial}{\partial x_j}\left[(\mu + \sigma_\omega \mu_T)\frac{\partial \omega}{\partial x_j}\right] + 2(1 - F_1)\frac{\rho \sigma_{\omega 2}}{\omega}\frac{\partial k}{\partial x_j}\frac{\partial \omega}{\partial x_j}$$

$$P_k = \tau_{ij}\frac{\partial U_i}{\partial x_j}, \quad \tau_{ij} = \mu_T\left(2S_{ij} - \frac{2}{3}\frac{\partial U_k}{\partial x_k}\delta_{ij}\right) - \frac{2}{3}\rho k \delta_{ij}, \quad S_{ij} = \frac{1}{2}\left(\frac{\partial U_i}{\partial x_j} + \frac{\partial U_j}{\partial x_i}\right)$$

$$\mu_T = \frac{\rho a_1 k}{max(a_1 \omega, \Omega_{ij} F_2)}, \quad \phi = F_1 \phi_1 + (1 - F_1)\phi_2, \quad F_1 = tanh(arg_1^4) \tag{2.14}$$

$$agr_1 = min\left[max\left(\frac{\sqrt{k}}{\beta^* \omega d}, \frac{500\nu}{d^2 \omega}\right), \frac{4\rho \sigma_{\omega 2} k}{CD_{k\omega} d^2}\right], \quad F_2 = tanh(arg_2^2)$$

$$arg_2 = max\left(2\frac{\sqrt{k}}{\beta^* \omega d}, \frac{500\nu}{d^2 \omega}\right)$$

The constants for $k - \omega$ closure are: $\sigma_{k1} = 0.85$, $\sigma_{w1} = 0.65$, $\beta_1 = 0.075$ and $k - \varepsilon$ closure are: $\sigma_{k2} = 1.0$, $\sigma_{w2} = 0.856$, $\beta_2 = 0.0828$ and SST closure constants: $\beta^* = 0.09$, $a_1 = 0.31$. The recommended boundary conditions are for far-field: $\frac{U_\infty}{L} < \omega_{farfield} < \frac{10U_\infty}{L}$ and $\frac{10^{-5}U_\infty^2}{Re_L} < k_{farfield} < \frac{0.1U_\infty^2}{Re_L}$ for wall: $\omega_{wall} = 10\frac{6\nu}{\beta_1(\Delta d_1)^2}$, $k_{wall} = 0$. Several updates have also been proposed to this model such as Vorticity source term (SST-V, SST-Vm), Kato-Launder source term (SST-KL, SST-KLm) and also the Rotation/Curvature correction (SST-RC-Hellsten, SST-RC) to the Production term for its wide applicability in complex engineering systems.

2.5.3   Reynolds Stress model(RSM) - SSG/LRR-ω

Unlike the scalar transport models, Reynolds stress models (also known as Second Moment Closure models) try to obtain the turbulent stresses directly using a transport equation for each component of the tensor. Scalar transport models don't perform well in complex flows with significant strain-rates such as curved boundary layers, swirling flows, rotating flows, flows with significant streamline curvature, flows with huge anisotropy in turbulent stresses and disequilibrium in rapidly changing flow conditions [51, 11]. Reynolds stress tensor $\overline{u_i u_j}$ is a symmetrical tensor with 6 independent components where 3 diagonal components constitute the normal stresses and the 3 off-diagonal components represent the shear stresses. Anisotropic effects result in significant changes to the shear stresses. Models such as $k - \varepsilon, k - \omega$, SST solve k where all the normal stresses are treated as a single term. For example, stable streamline curvature suppresses the component directed towards the center of the curvature. Accurate estimation of the anisotropy of the normal stresses is very essential. Solving a transport equation for each of these independent components can account for the directional effects of the Reynolds stress field [51, 11]. One of the variants of RSM which we concentrate in the present study is SSG/LRR-ω model which is a seven equation model which solves six reynolds stresses and one length scale (ω).

The Speziale-Sarkar-Gatski (SSG) model is a widely recognized nonlinear redistribution model. However, it relies on an ε-equation to determine the length-scale, which may not be optimal for aerodynamic applications where ω-equations have demonstrated advantages. To address this, the SSG-ε model has been combined with the LRR-ω (Wilcox stress-ω) model, particularly near walls. This integration involves blending coefficients from the LRR values at the wall to the SSG values further away, utilizing F1 blending function from Menter's k-ω models. This model must be combined with Menter's baseline (BSL)ω-equation which changes coefficients accordingly from the wall to the far field. Thus the SSG/LRR-ω model consequently transfers the principles of Menter's k-ω models into the framework of Reynolds stress transport equations [7].

Using the notation $\hat{R}_{ij} = \overline{u_i u_j}$, the $SSG/LRR - \omega$ turbulence model is given by:

$$\frac{\partial \overline{\rho}\hat{R}_{ij}}{\partial t} + \frac{\partial(\overline{\rho}U_k\hat{R}_{ij})}{\partial x_k} = \overline{\rho}P_{ij} + \overline{\rho}\Pi_{ij} - \overline{\rho}\varepsilon_{ij} + \overline{\rho}D_{ij} + \overline{\rho}M_{ij}$$

$$\frac{\partial(\overline{\rho}\omega)}{\partial t} + \frac{\partial(\overline{\rho}U_k\omega)}{\partial x_k} = \frac{\alpha_\omega \omega}{k}\frac{\overline{\rho}P_{kk}}{2} - \beta_\omega\overline{\rho}\omega^2 + \frac{\partial}{\partial x_k}\left[\left(\overline{\mu} + \sigma_\omega\frac{\overline{\rho}k}{\omega}\right)\frac{\partial\omega}{\partial x_k}\right] + \sigma_d\frac{\overline{\rho}}{\omega}max\left(\frac{\partial k}{\partial x_j}\frac{\partial\omega}{\partial x_j},0\right)$$

$$\overline{\rho}P_{ij} = -\overline{\rho}\hat{R}_{ij}\frac{\partial U_j}{\partial x_k} - \overline{\rho}\hat{R}_{ij}\frac{\partial U_i}{\partial x_k}, \quad \overline{\rho}\varepsilon_{ij} = \frac{2}{3}\overline{\rho}\varepsilon\delta_{ij}, \quad \varepsilon = C_\mu k\omega$$

(2.15)

The production term $(\overline{\rho}P_{ij})$ is exact and the pressure-strain correlation is modeled via:

$$\overline{\rho}\Pi_{ij} = -\left(C_1\overline{\rho}\varepsilon + \frac{1}{2}C_1^*\overline{\rho}P_{kk}\right)\hat{a}_{ij} + C_2\overline{\rho}\varepsilon\left(\hat{a}_{ik}\hat{a}_{kj} - \frac{1}{3}\hat{a}_{kl}\hat{a}_{kl}\delta_{ij}\right) + \left(C_3 - C_3^*\sqrt{\hat{a}_{kl}\hat{a}_{kl}}\right)\overline{\rho}kS_{ij}^* +$$

$$C_4\overline{\rho}k\left(\hat{a}_{ij}S_{jk} + \hat{a}_{jk}S_{ik} - \frac{2}{3}\hat{a}_{kl}S_{kl}\delta_{ij}\right) + C_5\overline{\rho}k\left(\hat{a}_{ik}\Omega_{jk} + \hat{a}_{jk}\Omega_{ik}\right) \quad (2.16)$$

where the anisotropic tensor is obtained by $\hat{a}_{ij} = \frac{\hat{R}_{ij}}{k} - \frac{2}{3}\delta_{ij}$ and $S_{ij}^* = S_{ij} - \frac{1}{3}S_{kk}\delta_{ij}$ The pressure strain correlation is a blend between the Launder-Reece-Rodi (LRR) model [21] within inner 60% of the boundary layer and the Speziale-Sarkar-Gatski (SSG) model [44] in the outer part of the boundary layer and the freestream. The Diffusion term $(\overline{\rho}D_{ij})$ is modeled by the Generalized Gradient Diffusion Hypothesis (GGDH) from Daly & Harlow [9] which is given by

$$\overline{\rho}D_{ij} = \frac{\partial}{\partial x_k}\left[\left(\overline{\mu}\delta_{kl} + D\frac{\overline{\rho}kR_{kl}}{\varepsilon}\right)\frac{\partial R_{ij}}{\partial x_l}\right] = \frac{\partial}{\partial x_k}\left[\left(\overline{\mu}\delta_{kl} + D\frac{\overline{\rho}kR_{kl}}{C_\mu\omega}\right)\frac{\partial R_{ij}}{\partial x_l}\right] \quad (2.17)$$

In the present work, SSG/LRR-ω has also been tested with Simple Gradient Diffusion Hypothesis(SGDH) [35] for the transport term which is elaborated in Appendix A.3.1.

The flux $\overline{\rho}M_{ij}$ is neglected and all the coefficients are blended similar to the Menters's SST Model:

$$\phi = F_1\phi^{(\omega)} + (1 - F_1)\phi^{(\varepsilon)}, \quad F_1 = tanh(\zeta^4)$$

$$\zeta = min\left[max\left(\frac{\sqrt{k}}{C_\mu\omega d}, \frac{500\mu}{\overline{\rho}\omega d^2}\right)\right], \quad (CD) = \sigma_d^{(\varepsilon)}\frac{\overline{\rho}}{\omega}max\left(\frac{\partial k}{\partial x_k}\frac{\partial\omega}{\partial x_k},0\right) \quad C_\mu = 0.09$$

(2.18)

The near-wall / inner coefficients with superscript (ω) are given by:

$$\alpha_\omega^{(\omega)} = 0.5556, \quad \beta_\omega^{(\omega)} = 0.075, \quad \sigma_\omega^{(\omega)} = 0.5, \quad \sigma_d^{(\omega)} = 0$$

$$C_1^{(\omega)} = 1.8, \quad C_1^{*(\omega)} = 0, \quad C_2^{(\omega)} = 0, \quad C_3^{(\omega)} = 0.8, \quad C_3^{*(\omega)} = 0$$

$$C_4^{(\omega)} = 0.5\left(\frac{18C_2^{(LRR)} + 12}{11}\right), \quad C_5^{(\omega)} = 0.5\left(\frac{-14C_2^{(LRR)} + 20}{11}\right),$$

$$D^{(\omega)} = 0.75C_\mu \quad C_2^{(LRR)} = 0.52$$

(2.19)

The outer coefficients with superscript (ε) are:

$$\alpha_\omega^{(\varepsilon)} = 0.44, \quad \beta_\omega^{(\varepsilon)} = 0.0828, \quad \sigma_\omega^{(\varepsilon)} = 0.856, \quad \sigma_d^{(\varepsilon)} = 1.712$$

$$C_1^{(\varepsilon)} = 1.7, \quad C_1^{*(\varepsilon)} = 0.9, \quad C_2^{(\varepsilon)} = 1.05, \quad C_3^{(\varepsilon)} = 0.8, \quad C_3^{*(\varepsilon)} = 0.65$$

$$C_4^{(\varepsilon)} = 0.625, \quad C_5^{(\varepsilon)} = 0.2, \quad D^{(\varepsilon)} = 0.22C_\mu$$

(2.20)

The boundary conditions for $SSG/LRR - \omega$ model are $R_{ij,farfield} = \frac{2}{3}k_{farfield}\delta_{ij}$ and $\omega_{farfield} = \frac{\overline{\rho}k_{farfield}}{\mu_{T,farfield}}$ where $k_{farfield}$, $\mu_{T,farfield}$ are user defined. Usually, it is linked to the turbulence intensity

(Ti) by $k_{farfield} = (3/2)(Ti)^2 U_{farfield}^2$ At solid walls, $R_{ij,wall} = 0$, $\omega_{wall} = 10\frac{6\nu}{\beta_\omega^{(\omega)}(\Delta d_1)^2}$ where Δd_1 is the distance from the wall to the nearest field solution point. For symmetry boundaries, Reynolds stress components should have Dirchilet conditions of zero depending on the x, y, z symmetry planes as elucidated in [26]. It is very essential that the Reynolds stresses adhere to the realizability conditions as elaborated in Vreman et al. [52] which are 1) For the diagonal elements: $\overline{\rho u_i u_j} \geq 0$ and 2) for the off-diagonal elements $|\overline{\rho u_i u_j}| \leq \sqrt{(\overline{\rho u_i u_i})(\overline{\rho u_j u_j})}$

2.6 DLR TAU solver

In the present work, the Numerical flow solver, TAU was used to perform the CFD simulations. TAU is a software system for the prediction of viscous and inviscid flows for complex geometries from low subsonic to hypersonic region with hybrid unstructured grids. The TAU-Code demonstrates high efficiency on parallel computers and has been optimized for cache processors through specialized edge coloring procedures. Domain decomposition and Message Passing Interface (MPI) make TAU more suitable for simulations of complex geometries and fine meshes. TAU mainly consists of a preprocessing module, compressible and incompressible flow solvers along with adaptation modules. The support for tetrahedral, prismatic, pyramidal and hexahedral elements facilitates the use efficient and modern mesh generators. The adaptation module takes care of local refinement of the hybrid grids and rearrangement of the points in structured sublayers using the flow features. Using multigrids, vectorization and parallelization, TAU ensures efficient computation for large scale steady or unsteady flow problems [34].

2.7 Mesh generation

Fidelity Pointwise was used to generate meshes for the testcases in present study. Fidelity Pointwise is a standalone CFD grid generator which provides a full range of functionalities starting from model preparation of geometry, importing CAD models from wide range of formats, mesh generation using a variety of state-of-art grid generation techniques and the output format compatibility with broad range of flow solvers [6].

2.8 Post Processing

In the present study, Tecplot 360 software was used for post processing of the CFD results. Tecplot 360 is a widely used, powerful post-processing tool for visualizing a wide range of technical data. It offers line plotting, 2D and 3D surface plots in a variety of formats, and 3D volumetric visualization etc [47].

Chapter 3

Effects of mean-streamline curvature

This section describes the main effects of mean-streamline curvature on the turbulence.

3.1 Convex vs Concave curvature

This introduction starts with an intuitive picture of curvature effects by Bradshaw. Flow in a curved path gives rise to a radial pressure gradient depending on the radius of curvature. This is caused by the radially outward centrifugal force which is proportional to the momentum of fluid parcel. The radially-outward centrifugal force is balanced by the inward pressure gradient. Consider a turbulent boundary layer flow over a convex surface. Slow moving particles with less centrifugal force are pushed radially inward due to the dominating pressure gradient force when they try to mix with high momentum fluid. So, flow through a convex curvature hinders exchange of momentum, energy thus exerting a stabilizing influence on the turbulence. And in the region of concave curvature, this effect will be opposite where the radial pressure-gradient enhances momentum exchanges which creates a de-stabilizing influence on the flow [39]. This intuitive picture is described in the seminal work by Bradshaw [5]. Overall for a flow, convex curvature reduces turbulence whereas a concave curvature enhances turbulence.

3.2 Structure of Turbulent Boundary Layers (TBL)

In this section, the changes to the structure of the turbulent boundary layer are briefly discussed.

3.2.1 Structure of convex TBL

For mild streamline curvature $\delta/R \approx 0.01$, the Reynolds shear stresses are slightly reduced but for strong streamline curvature $\delta/R > 0.05$, the Reynolds shear stresses can almost go to zero in the outer part of the boundary layer. The inner-part of TBL, consists of significant Reynolds shear stress and mean-shear and the outer-part of the TBL consists of non-zero mean-shear and negligible shear stress [25].

3.2.2 Structure of concave TBL

When a flow free on non-uniformities in the straight section enters a concave curvature, the mixing across the boundary layer is enhanced by the radial pressure gradient and the modified large eddy structure in the turbulent boundary layer due to curvature. This brings high momentum fluid closer to the wall thus increasing the skin friction. From spectral results, it was determined that the increase in turbulent intensities and Reynolds shear stress in concave TBL is almost entirely due

to increased energy in low-frequency, large-scale fluctuations [3]. Due to the centrifugal mechanism, higher-velocity eddies move closer to the wall while the lower-velocity eddies move away from the wall. This negative correlation is further enhanced within a few boundary layer thicknesses (δ).

This effect gives rise to longitudinal vortices known as "Taylor-Görtler" vortices or simple "Görtler" vortices in literature. As it was Görtler who identified longitudinal vortices in laminar boundary layers of concave walls in laminar flows in Ref. [15]. These vortices increase the turbulent shear stress on the concave walls thus altering velocity profile at different spanwise locations. Additional turbulence means more mixing and more resistance to the flow. So, the fluid moves slightly faster closer to the convex wall due to reduced turbulence.

3.3 Richardson number

Richardson number is a non-dimensional number which expresses the ratio of buoyancy to flow shear, quite prevalent in geophysical fluid dynamics.

$$Ri = \frac{Buoyancy}{Flow\ shear} = \frac{N^2}{\left(\frac{\partial U}{\partial z}\right)^2} \tag{3.1}$$

Here, N is the Brunt–Väisälä frequency, U is the representative flow speed and z is the depth or height (or z in the vertical direction).

3.3.1 Bradshaw's Richardson number

Bradshaw [4] suggested an algebraic analogy between buoyancy and streamline curvature in a turbulent shear flow. Brunt–Väisälä frequency was defined in polar coordinate system using the Azimuthal velocity (U) and radius of curvature (r): $N = \sqrt{\frac{2U}{r^2}\frac{\partial(Ur)}{\partial r}}$. This gives a new version of gradient Richardson number in polar coordinates as given in equation 3.2.

$$Ri = \frac{\frac{2U}{r^2}\frac{\partial(Ur)}{\partial r}}{\left(\frac{\partial U}{\partial r}\right)^2} \tag{3.2}$$

The numerator of equation 3.2 can be rearranged:

$$\frac{2U}{r^2}\frac{\partial(Ur)}{\partial r} \approx \frac{2U}{r^2}\left(U + r\frac{\partial U}{\partial r}\right) \approx \frac{2U}{r}\left(\frac{U}{r} + \frac{\partial U}{\partial r}\right) \tag{3.3}$$

such that the Bradshaw's gradient Richardson number can be written solely in terms of curvature(U/r) and shear ($\partial U/\partial r$).

$$Ri_{Br} = \frac{\frac{2U}{r}\left(\frac{U}{r} + \frac{\partial U}{\partial r}\right)}{\left(\frac{\partial U}{\partial r}\right)^2} \tag{3.4}$$

Here the denominator is always positive and the sign of Ri_{Br} depends on the interplay between curvature and shear in the numerator. When the shear ($\partial U/\partial r$) approaches zero, this function yields excessively high and impractical values, which will be addressed later. Considering a ratio of curvature (U/r) to shear ($\partial U/\partial r$), gives a dimensionless parameter $S = (U/r)/(\partial U/\partial r)$ known as Vorticity ratio [1]. Equation 3.4 can be re-written in terms of the vorticity ratio (S) which results in equation of a parabola [49].

$$Ri_{Br} = 2S(S+1) \tag{3.5}$$

The effect of rotation/curvature is destabilizing when $-1 < S < 0$ and stabilizing otherwise[49]. In other words, negative values of Richardson number denote amplifying turbulence and positive

---

[1]S is the background-to-mean shear vorticity ratio (here referred as vorticity ratio) or inverse Rossby number which was derived by Prandtl and various authors later using classical mixing-length arguments [4, 49]
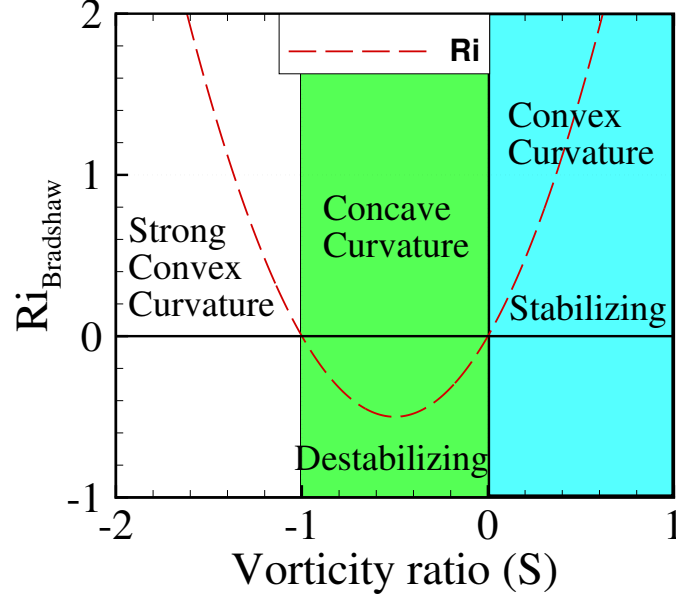
Figure 3.1: Behaviour of Richardson number showing stable/unstable zones

values denote diminishing turbulence. As shown in figure 3.1, turbulence is amplified only for a small set of values (green zone) which denotes flow through a concave curvature. $S \in [0, 1]$ denotes a shear-dominated convex curvature region (blue zone). Although, the flow is dominated by shear, the same sign of curvature and shear aligns the gradients in radial direction thereby stabilizing the flow.

$$\begin{aligned} \left|\frac{U}{r}\right| &> \left|\frac{\partial U}{\partial r}\right| \Rightarrow Convex\,(Curvature\,dominated) \\ \left|\frac{U}{r}\right| &< \left|\frac{\partial U}{\partial r}\right| \Rightarrow \begin{cases} Concave\,(Shear\,dominated,\,opposite\,sign) \\ Convex\,(Curvature\,dominated,\,same\,sign) \end{cases} \end{aligned} \tag{3.6}$$

$S < -1\,and\,S > 1$ occur only in cases with strong streamline-curvature and curvature dominated regions always attenuate turbulence. The behaviour of the Richardson number as a function of vorticity ratio (S) is elaborated later in chapter 5 using a test case.

3.3.2 Hellsten's Richardson number

The definition of Ri_{Br} is limited to representation in the polar coordinate system as it is quite difficult to obtain the radius of curvature at every point in a cartesian domain. This paved the way for a Galiliean-invariant formula for the Richardson number. A generalized definition of the gradient Richardson number for arbitrary three-dimensional flows was introduced by Khodak and Hirsch [17].

$$Ri = -\left(\frac{k}{\epsilon}\right)^2 ||\Omega_{ij}|| \left(||S_{ij}|| - ||\Omega_{ij}||\right) \tag{3.7}$$

Although when applied in conjunction with $k - \omega$ model, this version of Ri (shown in equation 3.7) produced reasonably good results for a two-dimensional fully developed flow rotating channel with moderate rotation, it produced unphysically high values for k in a three-dimensional complex problem [16]. The turbulent time scale (k/ϵ) in equation 3.7 which was used as a scaling factor, was replaced with mean-flow time scale $(1/|S_{ij}| = 1/\sqrt{2S_{ij}S_{ij}})$ by [16]. This resulted in a grid-point

local and Galilean-invariant formulation for the Richardson number as shown in eq. (3.8). A factor of 2 was introduced here for consistency with other definitions of Ri.

$$Ri_{Hellsten} = 2\frac{||\Omega_{ij}||}{||S_{ij}||}\left(\frac{||\Omega_{ij}||}{||S_{ij}||} - 1\right) \tag{3.8}$$

Note that, the formulae can be re-written using the ratio $S = ||\Omega_{ij}||/||S_{ij}|| - 1$ which results in equation of a parabola $Ri = 2S(S + 1)$ as shown in figure 3.1. The behaviour of $\tilde{S}$ was found to be similar to vorticity ratio (S). Ri reaches very high values when $||S_{ij}|| \to 0$, which points out high damping of turbulence.

According to the Boussinesq approximation, turbulent stresses tend to zero at smaller strain-rates which fits well for the behaviour of Ri_{Br} and $Ri_{Hellsten}$ [16]. The Richardson number in equation 3.8 was used to sensitize Menter's $k - \omega$ SST turbulence model for the effects of system rotation and streamline curvature.

As a final comment, the use of the turbulent time scale k/ϵ in eq. (3.7) can be viewed as an attempt to avoid high values of Ri when $||S_{ij}|| \to 0$.

3.3.3   Local Richardson number

Ströer and Knopp (2023) applied the rotation correction sensor $\tilde{r}$ developed by Spalart and Shur[43], in conjunction with prior formulations of the Richardson number [17, 16], to establish a new, grid-point local, and frame-invariant general formulation applicable to three-dimensional flows. A 180° U-turn curved channel test case by Monson et al. [23] was used to derive the new formulation of Richardson number. The details of test case are elaborated in chapter 4 and 5.

The rotation-rate tensor in polar coordinates is given by:

$$\Omega_{ij}^{\text{polar}} = \frac{1}{2}\begin{pmatrix} 0 & -\Omega_z & \Omega_\phi \\ \Omega_z & 0 & -\Omega_r \\ -\Omega_\phi & \Omega_r & 0 \end{pmatrix}$$

$$= \frac{1}{2}\begin{pmatrix} 0 & -\frac{U_\phi}{r} - \frac{\partial U_\phi}{\partial r} + \frac{1}{r}\frac{\partial U_r}{\partial \phi} & \frac{\partial U_r}{\partial z} - \frac{\partial U_z}{\partial r} \\ \frac{U_\phi}{r} + \frac{\partial U_\phi}{\partial r} - \frac{1}{r}\frac{\partial U_r}{\partial \phi} & 0 & -\frac{1}{r}\frac{\partial U_z}{\partial \phi} + \frac{\partial U_\phi}{\partial z} \\ -\frac{\partial U_r}{\partial z} + \frac{\partial U_z}{\partial r} & \frac{1}{r}\frac{\partial U_z}{\partial \phi} - \frac{\partial U_\phi}{\partial z} & 0 \end{pmatrix} \tag{3.9}$$

Here, in polar coordinates, r is the radial direction, ϕ is the azimuthal (or circumferential) direction, z is the axial direction. U_r and U_ϕ are velocities in radial and azimuthal direction respectively.

Assume that a flow through a curved channel can be approximated as 2D i.e., In the centre plane of a curved channel of constant height and large spanwise aspect ratio. All derivatives with respect to z (spanwise direction) can be considered zero. Moreover, it can be assumed that there is no angular acceleration due to constant channel height and U_r is considered to be small. The rotation-rate tensor reduces to:

$$\Omega_{ij} = \frac{1}{2}\begin{pmatrix} 0 & -\Omega_z & 0 \\ \Omega_z & 0 & 0 \\ 0 & 0 & 0 \end{pmatrix}$$

$$= \frac{1}{2}\begin{pmatrix} 0 & -\frac{U_\phi}{r} - \frac{\partial U_\phi}{\partial r} & 0 \\ \frac{U_\phi}{r} + \frac{\partial U_\phi}{\partial r} & 0 & 0 \\ 0 & 0 & 0 \end{pmatrix} \tag{3.10}$$

Therefore, the magnitude of rotation-rate tensor becomes:

$$||\Omega_{ij}|| = \sqrt{2\Omega_{ij}\Omega_{ij}} = \left[2\left(\frac{1}{4}\left(-\frac{\partial U_\phi}{\partial r} - \frac{U_\phi}{r}\right)^2 + \frac{1}{4}\left(\frac{\partial U_\phi}{\partial r} + \frac{U_\phi}{r}\right)^2\right)\right]^{1/2}$$

$$= \left(2\frac{1}{2}\left(\frac{\partial U_\phi}{\partial r} + \frac{U_\phi}{r}\right)^2\right)^{1/2} = \left(\left(\frac{\partial U_\phi}{\partial r} + \frac{U_\phi}{r}\right)^2\right)^{1/2} = \left|\frac{\partial U_\phi}{\partial r} + \frac{U_\phi}{r}\right| \quad (3.11)$$

Similarly, the strain-rate tensor in cylindrical coordinates can also be reduced which is given by:

$$S_{ij} = \frac{1}{2}\begin{pmatrix} \frac{\partial U_r}{\partial r} & \frac{1}{r}\frac{\partial U_r}{\partial \phi} + \frac{\partial U_\phi}{\partial r} - \frac{U_\phi}{r} & \frac{\partial U_r}{\partial z} + \frac{\partial U_z}{\partial r} \\ \frac{1}{r}\frac{\partial U_r}{\partial \phi} + \frac{\partial U_\phi}{\partial r} - \frac{U_\phi}{r} & \frac{1}{r}\frac{\partial U_\phi}{\partial \phi} + \frac{U_r}{r} & \frac{1}{r}\frac{\partial U_z}{\partial \phi} + \frac{\partial U_\phi}{\partial z} \\ \frac{\partial U_r}{\partial z} + \frac{\partial U_z}{\partial r} & \frac{1}{r}\frac{\partial U_z}{\partial \phi} + \frac{\partial U_\phi}{\partial z} & \frac{\partial U_z}{\partial z} \end{pmatrix} \quad (3.12)$$

$$= \frac{1}{2}\begin{pmatrix} 0 & \frac{\partial U_\phi}{\partial r} - \frac{U_\phi}{r} & 0 \\ \frac{\partial U_\phi}{\partial r} - \frac{U_\phi}{r} & 0 & 0 \\ 0 & 0 & 0 \end{pmatrix}$$

Therefore, the magnitude of strain-rate tensor can be written as:

$$||S_{ij}|| = \sqrt{2S_{ij}S_{ij}} = \left[2\left(\frac{1}{4}\left(\frac{\partial U_\phi}{\partial r} - \frac{U_\phi}{r}\right)^2 + \frac{1}{4}\left(\frac{\partial U_\phi}{\partial r} - \frac{U_\phi}{r}\right)^2\right)\right]^{1/2}$$

$$= \left(2\frac{1}{2}\left(\frac{\partial U_\phi}{\partial r} - \frac{U_\phi}{r}\right)^2\right)^{1/2} = \left(\left(\frac{\partial U_\phi}{\partial r} - \frac{U_\phi}{r}\right)^2\right)^{1/2} = \left|\frac{\partial U_\phi}{\partial r} - \frac{U_\phi}{r}\right| \quad (3.13)$$

Considering U for the azimuthal velocity U_ϕ and rewriting the expressions (based on eqs. (3.11), (3.13)) in terms of Galilean-invariant terms as shown in eq. (3.14). Note that the sign +/- is used loosely at this point. Finding the correct sign in an arbitrary flow situation is a crucial task. This will be resolved later by defining a quantity n_Ω which returns the desired +/- sign.

$$\frac{\partial U}{\partial r} + \frac{U}{r} = \Omega_z \approx \pm||\Omega_{ij}||$$
$$\frac{\partial U}{\partial r} - \frac{U}{r} = S_{r\phi} \approx \pm||S_{ij}|| \quad (3.14)$$

The appropriate Galilean-invariant terms can chosen for the absolute values of the quantities (shear + curvature) and (shear - curvature) can be chosen as follows:

$$\left|\frac{\partial U_\phi}{\partial r} + \frac{U_\phi}{r}\right| = \begin{cases} ||\Omega_{ij}|| \text{ if } \frac{\partial U}{\partial r} + \frac{U}{r} > 0 \\ -||\Omega_{ij}|| \text{ if } \frac{\partial U}{\partial r} + \frac{U}{r} < 0 \end{cases}$$
$$\left|\frac{\partial U_\phi}{\partial r} - \frac{U_\phi}{r}\right| = \begin{cases} ||S_{ij}|| \text{ if } \frac{\partial U}{\partial r} - \frac{U}{r} > 0 \\ -||S_{ij}|| \text{ if } \frac{\partial U}{\partial r} - \frac{U}{r} < 0 \end{cases} \quad (3.15)$$

It is important to point out that, again the +/- symbol is used loosely. It is necessary to study all cases of possible sign separately. This is pursued in the following table 3.1. Therefore the original Bradshaw's Richardson number Ri_{Br} can be rewritten in terms of absolute value combinations as

follows:

$$Ri = \frac{\left(\frac{\partial U}{\partial r} + \frac{U}{r}\right)\frac{2U}{r}}{\left(\frac{\partial U}{\partial r}\right)^2}$$

$$= -\frac{\left|\frac{\partial U}{\partial r} + \frac{U}{r}\right|\left(\left|\frac{\partial U}{\partial r} - \frac{U}{r}\right| - \left|\frac{\partial U}{\partial r} + \frac{U}{r}\right|\right)}{\frac{1}{4}\left(\left|\frac{\partial U}{\partial r} - \frac{U}{r}\right| + \left|\frac{\partial U}{\partial r} + \frac{U}{r}\right|\right)^2}$$

$$= -\frac{\pm||\Omega_{ij}||\left(\pm||S_{ij}|| - \pm||\Omega_{ij}||\right)}{\left(\pm\frac{1}{2}||S_{ij}|| + \pm\frac{1}{2}||\Omega_{ij}||\right)^2} \tag{3.16}$$

The final version of Richardson number in 3.16 is given completely grid-point local and Galilean-invariant coordinates. All combinations of '+' and '-' signs can be rearranged into a parameter n_Ω which determines the value of local Richardson number. The parameter $n_\Omega = \pm 1$ depends the signs and relative magnitudes of curvature U/r and shear $\partial U/\partial r$ which is elaborated in table3.1. This is elaborated in further sections of this chapter but shown here for the sake of completeness. This theoretical consideration is investigated by systematic numerical tests in chapter 5 in order to study all the different cases of combinations of magnitude and sign of S separately. Note that the function n_Ω will be described in detail in section 3.4.3. The local Richardson number can be written as:

$$Ri_{local} = -\frac{n_\Omega||\Omega_{ij}||\left(||S_{ij}|| - n_\Omega||\Omega_{ij}||\right)}{\left(\frac{1}{2}||S_{ij}|| + n_\Omega\frac{1}{2}||\Omega_{ij}||\right)^2} \tag{3.17}$$

In the following sections, a proposal for the function n_Ω will be devised. This function is based on the Spalart & Shur's rotation correction parameter $\hat{r}$ from [43] which was the core parameter in SA-RC model and is elaborated in further sections.

Table 3.1: Different possible cases for local Richardson number

Case	Relative magnitude	Vorticity ratio	$\frac{\partial U}{\partial r} - \frac{U}{r}$	$\frac{\partial U}{\partial r} + \frac{U}{r}$	$\frac{\partial U}{\partial r}$	$\frac{U}{r}$	$Ri(|\Omega|,|S|)$	n_Ω
$\frac{U}{r} > 0$	$\left|\frac{\partial U}{\partial r}\right| > \left|\frac{U}{r}\right|$	$S \in (0,1)$	$|S|$	$|\Omega|$	$\frac{1}{2}(|S|+|\Omega|)$	$\frac{1}{2}(-|S|+|\Omega|)$	$\frac{-|\Omega|(|S|-|\Omega|)}{\left(\frac{1}{2}|S|+\frac{1}{2}|\Omega|\right)^2}$	1
$\frac{\partial U}{\partial r} > 0$	$\left|\frac{\partial U}{\partial r}\right| < \left|\frac{U}{r}\right|$	$S > 1$	$-|S|$	$|\Omega|$	$\frac{1}{2}(-|S|+|\Omega|)$	$\frac{1}{2}(|S|+|\Omega|)$	$\frac{|\Omega|(|S|+|\Omega|)}{\left(\frac{1}{2}|S|-\frac{1}{2}|\Omega|\right)^2}$	-1
$\frac{U}{r} < 0$	$\left|\frac{\partial U}{\partial r}\right| > \left|\frac{U}{r}\right|$	$S \in (0,1)$	$-|S|$	$-|\Omega|$	$\frac{1}{2}(-|S|-|\Omega|)$	$\frac{1}{2}(|S|-|\Omega|)$	$\frac{-|\Omega|(|S|-|\Omega|)}{\left(\frac{1}{2}|S|+\frac{1}{2}|\Omega|\right)^2}$	1
$\frac{\partial U}{\partial r} < 0$	$\left|\frac{\partial U}{\partial r}\right| < \left|\frac{U}{r}\right|$	$S > 1$	$|S|$	$-|\Omega|$	$\frac{1}{2}(|S|-|\Omega|)$	$\frac{1}{2}(-|S|-|\Omega|)$	$\frac{|\Omega|(|S|+|\Omega|)}{\left(\frac{1}{2}|S|-\frac{1}{2}|\Omega|\right)^2}$	-1
$\frac{U}{r} < 0$	$\left|\frac{\partial U}{\partial r}\right| > \left|\frac{U}{r}\right|$	$S \in (-1,0)$	$|S|$	$|\Omega|$	$\frac{1}{2}(|S|+|\Omega|)$	$\frac{1}{2}(-|S|+|\Omega|)$	$\frac{-|\Omega|(|S|-|\Omega|)}{\left(\frac{1}{2}|S|+\frac{1}{2}|\Omega|\right)^2}$	1
$\frac{\partial U}{\partial r} > 0$	$\left|\frac{\partial U}{\partial r}\right| < \left|\frac{U}{r}\right|$	$S < -1$	$|S|$	$-|\Omega|$	$\frac{1}{2}(|S|-|\Omega|)$	$\frac{1}{2}(-|S|-|\Omega|)$	$\frac{|\Omega|(|S|+|\Omega|)}{\left(\frac{1}{2}|S|-\frac{1}{2}|\Omega|\right)^2}$	-1
$\frac{U}{r} > 0$	$\left|\frac{\partial U}{\partial r}\right| > \left|\frac{U}{r}\right|$	$S \in (-1,0)$	$-|S|$	$-|\Omega|$	$\frac{1}{2}(-|S|-|\Omega|)$	$\frac{1}{2}(|S|-|\Omega|)$	$\frac{-|\Omega|(|S|-|\Omega|)}{\left(\frac{1}{2}|S|+\frac{1}{2}|\Omega|\right)^2}$	1
$\frac{\partial U}{\partial r} < 0$	$\left|\frac{\partial U}{\partial r}\right| < \left|\frac{U}{r}\right|$	$S < -1$	$-|S|$	$|\Omega|$	$\frac{1}{2}(-|S|+|\Omega|)$	$\frac{1}{2}(|S|+|\Omega|)$	$\frac{|\Omega|(|S|+|\Omega|)}{\left(\frac{1}{2}|S|-\frac{1}{2}|\Omega|\right)^2}$	-1

3.4 Curvature modification of RANS models

Several modifications have been suggested for RANS models in the past few decades mainly for linear eddy viscosity models. Mean-streamline curvature and rotation qualitatively generate a stabilizing or destabilizing effect on a turbulent flow which leads to damping or amplifying turbulence.

3.4.1 Rotation/Curvature correction for SA, SST

A simple intuitive model was proposed by Dacles-Mariani et al. [8] for rotation correction to SA model which reduces the eddy viscosity in the regions where vorticity exceeds strain rate. Flow within a vortex core consists of solid body rotation where turbulence production is low. SA-R [8] concentrated on a pragmatic improvement of eddy-viscosity based RANS models for simulating trailing vortices on wingtips. The production term of SA is modified as shown in eq. (3.18).

$$c_{b1}(1 - f_{t2})\hat{S}\hat{\nu} \rightarrow c_{b1}(1 - f_{t2}) \left[\hat{S} + C_{rot}min(0, S - \Omega) \right] \hat{\nu}$$
$$S = \sqrt{2S_{ij}S_{ij}}, \quad S_{ij} = \frac{1}{2} \left(\frac{\partial u_i}{\partial x_j} + \frac{\partial u_j}{\partial x_i} \right) \tag{3.18}$$

Spalart and Shur [43], [36] derived a Galilean invariant formulation that calculates the angle of misalignment of stress-strain tensors which is based on the work of Knight and Saffman [18]. Spalart-Shur's rotation-curvature correction unifies curvature and rotation effects using a combination of second derivatives of velocity which is given by eq. (3.19).

$$f_{r1} = (1 + c_{r1})\frac{2r^*}{1 + r^*} \left[1 - c_{r3}tan^{-1}(c_{r2}\hat{r}) \right] - c_{r1}$$
$$r^* = \frac{S}{\Omega}$$
$$\hat{r} = \frac{2\Omega_{ik}S_{jk}}{D^4} \left(\frac{DS_{ij}}{Dt} + (\varepsilon_{imn}S_{jn} + \varepsilon_{jmn}S_{in})\Omega_m^{rot} \right)$$
$$S_{ij} = \frac{1}{2} \left(\frac{\partial u_i}{\partial x_j} + \frac{\partial u_j}{\partial x_i} \right), \quad \Omega_{ij} = \frac{1}{2} \left[\left(\frac{\partial u_i}{\partial x_j} - \frac{\partial u_j}{\partial x_i} \right) + 2\varepsilon_{mji}\Omega_m^{rot} \right]$$
$$S^2 = 2S_{ij}S_{ij}, \quad \Omega^2 = 2\Omega_{ij}\Omega_{ij}$$
$$D^2 = \frac{1}{2}(S^2 + \Omega^2), \quad c_{r1} = 1.0, \quad c_{r2} = 12, \quad c_{r3} = 1.0$$
$$\frac{DS_{ij}}{Dt} = \frac{\partial S_{ij}}{\partial t} + u_k \frac{\partial S_{ij}}{\partial x_k} \tag{3.19}$$

The function f_{r1} that is built on the non-dimensional quantities r^* and $\hat{r}$ (elaborated in eq. (3.19)) is used as a coefficient to the production term of SA model such that the production term becomes: $c_{b1}(f_{r1} - f_{t2})\hat{S}\hat{\nu}$. The material derivative of $\frac{DS_{ij}}{Dt}$ is required in time-dependent simulation such as helicopter rotor and usually the time term is omitted in the material derivative [26]. The Ω^{rot} term is used only if the frame of reference is rotating at rate (Ω^{rot}). SA-RC has been one of the most successful and widely applied rotation corrections till date.

Spalart-Shur's rotation-curvature correction framework has been applied to Menter's SST model in Ref. [38] where a limited version of the function f_{r1} has been applied to the production terms of k and ω as show in eq. (3.20).

$$f_{SST-RC} = \max \left[\min(f_{r1}, 1.25), 0.0 \right] \tag{3.20}$$

The production term of k equation is modified as $f_{SST-RC}P_k$ and the production term of ω equation becomes $\frac{\gamma P_k}{\nu_t}f_{SST-RC}$. In eq. (3.20), the lower limit is introduced for numerical stability reasons and the upper limit is to avoid the over-generation of eddy viscosity for destabilizing case

[38]. Moreover, the D^2 in eq. (3.19) is limited by $D^2 = \max(S^2, 0.09\omega^2)$ to avoid zero values in free stream region and the following constants are calibrated to $c_{r1} = 1.0$, $c_{r2} = 2.0$, $c_{r3} = 1.0$ to get the best agreement with the experiments [38].

Hellsten used a new Galilean-invariant Richardson number formulation for sensitisation of SST model in Ref. [16], but it is limited to flows with moderate curvature. This is also investigated in the chapter 5.

3.4.2   Possible candidate terms for curvature modification for RSM

The question arises as to whether a second moment closure model like the SSG/LRR-ω model necessitates curvature modifications. Usually, a second moment closure model is inherently built with means to capture the effect of rotation or streamline curvature (at least concerning several aspects which were found to be important). This is because it doesn't depend on the concept of eddy viscosity and solves individual transport equations for the Reynolds stress tensor. So, the misalignment angle problem of stress-strain tensor doesn't apply to a Reynolds stress model. Therefore, on one hand, the misalignment. Another aspect is that the production term in the transport equation for the Reynolds stresses is exact. In curved shear flow, curvature effects arise in the production term and can be seen to act differently on the different components of the Reynolds stress tensor (see Ref. [11], p.163 and Ref. [10]). This cannot be accounted for if the eddy-viscosity hypothesis is used as the constitutive law for the Reynolds stresses.

In complicated scenarios such as in adverse-pressure gradient turbulent boundary layers, SSG/LRR-ω fails to give reasonable solutions which as investigated by Knopp in Ref. [19]. Therefore it might be prudent to go back to the unclosed transport equation for the Reynolds stresses and to consider all terms for which closure models are used. Closure models are needed for the turbulent transport due to velocity fluctuations (often referred to as triple-correlations and called turbulent transport of Reynolds stresses) and due to pressure-velocity fluctuations (often referred to as pressure transport). Then there is the pressure-strain correlation tensor, responsible for redistribution of the Reynolds stresses among the different components of the tensor. Finally, there is the dissipation tensor. For the latter, two assumptions are made, On the one hand, the SSG/LRR-ω model assumes isotropic dissipation and on the other, the model uses the solution of the transport equation for ω to infer $\epsilon = C_\mu k\omega$.

All these modelling assumptions do not account for curvature effects explicitly. However, there is the notion by Bradshaw that curvature should have an effect on the higher order statistics.

The work by Knopp [19] on turbulent boundary layers in adverse pressure gradient indicated the need that the modelling assumptions for the dissipation, e.g., for the omega equation, could require modification in more complex flow situations other than flow in zero pressure gradient.

In a differential Reynolds stress model like SSG/LRR-ω, the production term is responsible to capture the effect of increasing production in destabilizing curvature. But, in cases where the production is weak, turbulence transport might control the balance of Reynolds stresses [46]. According to Zeman [56], a simple gradient diffusion hypothesis (GDH) is not enough to model such complicated scenarios because the effects of rotation and streamline curvature are neglected in the turbulence transport term.

Production term of SSG/LRR-ω is closed unlike eddy viscosity type RANS models. The Turbulent transport term comprises of a triple correlation which is approximated by gradient diffusion hypothesis. Ströer and Knopp [45] tried to modify the turbulence transport term (due to fluctuating velocity) using the formulation of local Richardson number but no change was observed in the mean velocity for U-duct channel and lower values of turbulent kinetic energy were observed for the simulation of trailing vortex of a delta wing. This is further investigated in the present work.

The turbulence transport due to pressure fluctuations is usually neglected because of minimal contribution and because its model is typically lumped together with the turbulent transport term. The pressure-strain correlation (Redistribution) uses an algebraic model which is complicated and requires more data to model. The dissipation term is modelled as a solution of a transport equation of length scale (ω) in the SSG/LRR-ω. In the present work, the transport term is investigated further using test cases of different types and magnitudes of curvature.

3.4.3   Direction information in local Richardson number

A frame invariant quantity was obtained in eq. (3.16) which replicates the classical Richardson number in Galilean-invariant fashion. But, the direction information which decides the $\pm$ sign is lost due to the absolute magnitudes of vorticity and strain-rate tensor. This $\pm$ sign is of prime importance as it decides if the curvature is convex or concave. For a boundary layer, this is obvious from curvature of the wall which species the direction of radial vector and fluid flow orientation. But, for a free shear flow, to obtain the sign one needs to compare the magnitudes and signs of U/r and $\partial U/\partial r$ which is not Galilean invariant. Moreover, the actual mean shear has two contributions: the shear of the corresponding flow in the absence of curvature/rotation and the extra rate of strain U/r caused by curvature/rotation, as the radial pressure gradient $\partial p/\partial r$, which forces the fluid motion to follow a curved path, is balanced by $\rho U^2/r$.

The rotation/curvature correction from Spalart and Shur [43] presents this direction information in a fully grid-point local and Galilean-invariant fashion. According to Ref. [43], the stress-strain misalignment is in the direction of vorticity. So, the sign of $(D\alpha/Dt)\mathrm{sgn}(\Omega_z)$ is represented by the non-dimensional quantity $\hat{r}$ hereafter known as r_b following the convention in TAU solver. This equivalence is show in eq. (3.21) from [43] and [46].

$$\mathrm{sgn}\left[\frac{D\alpha}{Dt}\mathrm{sgn}(\Omega_z)\right] = \mathrm{sgn}\left[\frac{U}{r}\mathrm{sgn}(\Omega_z)\right] = sgn(r_b) \tag{3.21}$$

Small positive values of r_b suppress turbulence and small negative values of r_b enhance turbulence activity [43]. Moreover, a second step is required to obtain the direction information of local Richardson number, because the $\pm$ sign is defined by $S_{r\phi}$ and Ω_z (see eq. (3.14)). Using different combinations of U/r and $\partial U/\partial r$ from the table of different possible cases, a rotation function can be obtained which is given by eq. (3.22) in Ref. [46].

$$f_{rot} = \mathrm{sgn}\left[2\Omega_z\frac{U}{r}\right]\frac{||S_{ij}||}{||\Omega_{ij}||} = \mathrm{sgn}(r_b)\frac{||S_{ij}||}{||\Omega_{ij}||} \tag{3.22}$$

The direction sensor for the local Richardson number can be obtained by using a tanh function as shown in eq. (3.23) where the sign changes from 1 to -1 when f_{rot} becomes greater than 1. [46].

$$n_\Omega = \tanh(1000 - 1000f_{rot}) \tag{3.23}$$

Note that function n_Omega will be studied and illustrated for the numerical tests presented in chapter 5. Using the direction information provided by eq. (3.23) using Spalart-Shur rotation/correction framework(eq. (3.19)), the grid-point local and Galilean invariant formulation based on the table 3.1, can be written as :

$$Ri_{local} = -\frac{n_\Omega||\Omega_{ij}||\left(||S_{ij}|| - n_\Omega||\Omega_{ij}||\right)}{\left(\frac{1}{2}||S_{ij}|| + n_\Omega\frac{1}{2}||\Omega_{ij}||\right)^2} \tag{3.24}$$

The local Richardson number in eq. (3.24) which replicates the classical Bradshaw's Richardson number in eq. (3.4) can be used to senstise RANS models for mean streamline curvature and rotation and also as a potential guiding parameter in Data-driven turbulence modelling techniques such as Field Inversion/Machine Learning [37].

3.4.4   Necessity of a transfer function

As the Bradshaw's Richardson number (and local Richardson number) follows the parabola shown in fig. 3.1, it can be observed that Richardson number is bounded in the destabilizing (concave) zone i.e. $S \in (0,1)$ with a minimum value of Ri = -0.5. In the convex and strong convex zones where absolute value of the vorticity ratio (S) is greater than 1, Richardson number behaves as an increasing curve. This suggests the scope for Richardson number to obtain abnormally high values outside of concave region. Moreover, the Bradshaw's Richardson number is built with radial gradient
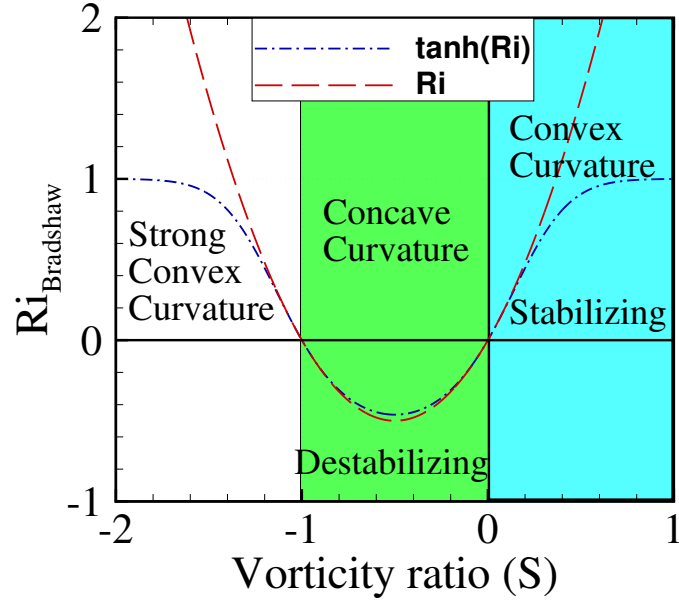
Figure 3.2: Behaviour of Richardson number in different zones with a tanh function

of velocity in denominator (see eq. (3.4)) which points out the possibility of a discontinuity (due to a singularity) when $\partial U/\partial r \to 0$.

A transfer function is necessary to practically use the Richardson number in a robust manner for any type of complex flow problem. Instead of directly using Ri, tanh (Ri) is used in the present work to clip high values of Ri. Moreover, such a transfer function would prevent extremely high values of Ri arising due to vanishing dU/dy which arises discontinuity in Ri. The stabilizing effect from convex to strong convex cases is only marginally higher. tanh (Ri) provides a maximum value of Ri = 1 in convex regions thus making it practically robust for sensitisation of RANS models. A deeper investigation on the variation of Richardson number for different magnitudes of curvature in convex and concave boundary layers in investigated in the chapter 5.

Chapter 4

Validation cases: Development of computational setup

4.1 Description of validation cases

Few experimental test cases are available in literature for curved boundary layers. Table 2 in the review paper by Patel and Saroupoulous gives an overview about notable experiments in this regard. For the selection of suitable cases, following requirements were made. First, the Reynolds number should be sufficiently high $Re_\theta > 3000$ to ensure a sufficiently thick overlap region between inner and outer boundary layer. Recall that the SSG/LRR-ω model does not attempt to resolve the near-wall region (which was pursued e.g. in the low-Re RSM by Jakirlic and Hanjalic). Therefore the SSG/LRR-ω model is expected to yield good predictions only in the overlap region and in the outer region. Secondly, the experiment needs to be fully documented regarding the geometry and the boundary conditions. Thirdly, the flow conditions in the test-section of the experiment should allow for a 2D computational setup. A small spanwise extent would make such a 2D setup questionable. In the case of concave curvature, 3D Görtler vortices can arise, a topic which is discussed in section 3.2.2. Another criterion was the availability of measurement data for the mean velocity and for the Reynolds stresses. Other criteria were a sufficient streamwise length for flow development in the curved section (hence no rapid curvature impulse) and to cover different values of curvature (in terms of δ/R).

Few experiments from the literature with different curvature ratios for both Concave and Convex curvatures were chosen to simulate and validate using SA-RC, SST-RC and multiple RSM re-distribution models which are as follows:

4.1.1 Monson et al. (1990)

Experimental setup

This testcase consists of an turbulent subsonic internal flow in a U-shaped duct. The experiment was conducted at NASA Ames High Reynolds Number Channel I (HRC I), an air blowdown wind tunnel using unheated dry air at ambient temperature with a 180° Turn Around Duct (TAD). The spanwise-width of duct was 10 times that of duct height which makes the aspect ratio, AR = 10. For the duct height H = 3.8 cm, the duct was extended to around 22 H upstream for the development of small Turbulent boundary layer and around 13 H downstream the curvature for recovery. The inner radius of the bend is equal to the half-height of spanwise-wide duct which makes the curvature ratio, $\delta/R \approx 0.5$ at convex bend and $\delta/R \approx 0.16$ at the concave bend. Due to the large aspect ratio (AR = 10:1) and the placement of suction slots spaced H apart upstream of the bend to remove the side-wall boundary layers, the flow is approximated as two dimensional [24]. Experiments were performed at two Reynolds numbers, $Re_H = 10^5$, 10^6 with a reference velocity $U_{\text{ref}} = 32\,\text{m/s}$ and reference Mach number $M_{\text{ref}} = 0.1$. Mean velocity and Reynolds shear stress were measured using

two-component Laser-Doppler Velocimetry at different streamwise locations. In the curved region, measurements are available for the mean velocity and Reynolds shear stress only at 90° position which are used for validation.
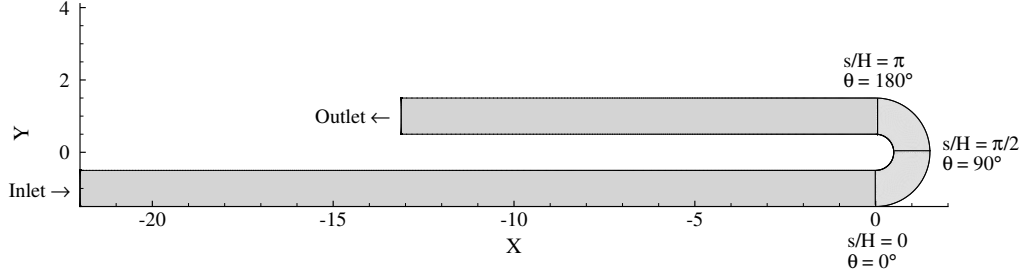
Figure 4.1: Geometry of the CFD domain of two dimensional U-duct [23] and mesh with 1070×200 grid points.

Computational setup

The two dimensional geometry and the mesh was constructed in Pointwise with duct height H = 1 m as shown in the fig. 4.1. The configuration of high Reynolds number, Re = 10^6 was chosen for the current study. From the plots of skin-friction coefficient in Ref. [23], $C_f = 0.012$ was chosen approximately from the 90° position on concave wall. Based on the details of $U_{\text{ref}} = 32$ m/s, Re = 10^6, H = 1 m, the wall normal spacing of first grid point away from the wall was calculated for a y^+ = 0.2 as shown in eq. (4.1).

$$
\begin{aligned}
u_\tau &= \sqrt{\frac{\tau_w}{\rho}} = \sqrt{\frac{1}{2} C_f U_\infty^2} \\
Re &= \frac{U_\infty H}{\nu} \Rightarrow \nu = \frac{U_\infty H}{Re} \\
\Delta y_1 &= \frac{y^+ \nu}{u_\tau} \\
\Delta y_1 &= \frac{y^+ \sqrt{2} H}{Re \sqrt{C_f}} = \frac{0.2 \times \sqrt{2} \times 1}{10^6 \times \sqrt{0.012}} \approx 2.5 \times 10^{-6} \, \text{m}
\end{aligned}
\tag{4.1}
$$

'Reservoir-pressure-inflow' and 'Reservoir-pressure-outflow' boundary conditions are used for inlet and outlet in DLR-TAU and viscous-wall boundary condition was used for both inner and outer walls. CFD simulations were performed in DLR-TAU solver with low-Mach number settings. The reference parameters used in DLR-TAU are shown below in SI units.

```
References ----------------------------------------------------: -
        Reynolds number: 1000000
        Sutherland reference viscosity: 4.5e-5
        Reference pressure: 120738.87
        Reynolds length: 1.0
        Reference Mach number: 0.1
```

CFD simulations using the turbulence models SA-RC, SST-RC and SSG/LRR-ω were performed for the geometry validation. The geometry of Monson is fairly simple especially in the curved region. Experimental data for the mean velocity measurements were quite cluttered in Ref. [23]. So the mean velocity profile from the same experiment given in their preceding paper [24] were also taken
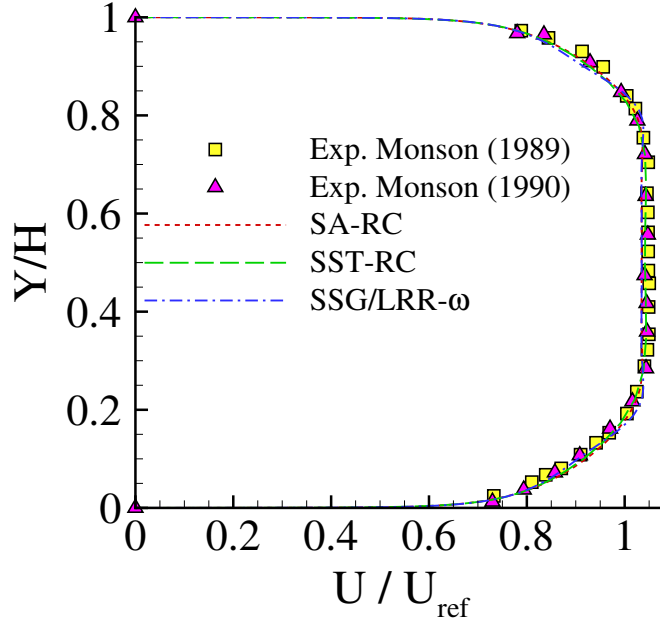
Figure 4.2: Inlet longitudinal velocity upstream of curvature in U-duct at s = -4H

for comparison as shown in fig. 4.2. The velocity measurements were normalised using U_{ref} as given in [23]. The boundary layer thickness on top wall and bottom wall are slightly different in the experiment which is known to happen sometimes in wind tunnels due to the turning vanes on the corner before inlet. To facilitate this, the transition point was defined slightly downstream i.e. at s = -19H for top wall and s = -22H for bottom wall (inlet position). Mean velocity profiles were evaluated at streamwise position s = -4H as shown in fig. 4.2. The velocity profiles of RANS models show a good agreement with that of experimental measurements.

4.1.2   Gillis & Johnston (1983)

Experimental setup

This experiment consists of a duct with flat surface followed by a 90° bend with constant radius of curvature and a flat recovery region. Aspect ratio of the duct is 11:1 which makes it nomially a two dimensional flow. After the nozzle, a development region of 259 cm with a duct height of 15.2 cm is provided upstream of the curvature. The downstream recovery region after the end of curvature is 97.2 cm long. The radius of curvature was constant at 45 cm for the inner wall thus making the curvature ratio $\delta/R \approx 0.1$. This can be considered as a high convex curvature test case. In the experiment, the static pressure on the convex wall was maintained constant by adjusting the outer wall and bulging the duct. Hence, the drop in static pressure at the inner wall is compensated by the increasing pressure due to the diverging duct. The outer wall is fitted with a porous suction (see figure 4.3) at the start of curvature region to remove the boundary layer separation and the formation of separation bubble at the outer wall. The changes to coefficient of pressure (Cp) were below 0.05 which makes it a convex curved almost zero pressure gradient (ZPG) test case [14, 13]. Due to the streamwise curvature ZPG, the effects of convex curvature on the turbulence can be well understood i.e. the effects of curvature and pressure can be separated. In the experiment, mean velocity measurements were taken using 2 techniques: 1) accurate measurement with wall-static pressure and pitot tubes traversed across the boundary layer in wall-normal direction; 2) Measurement with a DISA 55M01 constant-temperature anemometer, a TSI 1076 linearizer and a DISA 55P01 horizontal wire probe. Due to the limitations of hot wires, the pitot tube data is more accurate especially in the curved region [13]. Measurements of Reynolds stress tensor were made

(a) Schematic of the experimental facility

(b) Suction box located on the concave wall, near the start of curvature
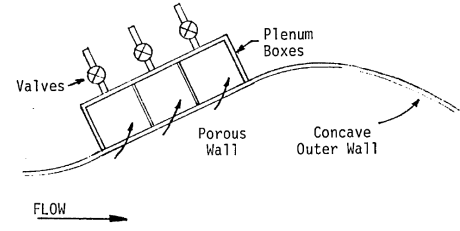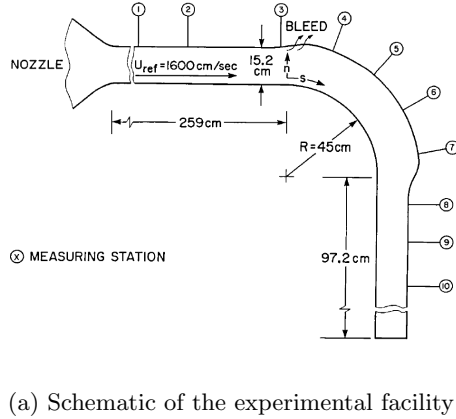
Figure 4.3: Experimental setup for the first experiment of Gillis-Johnston from Ref. [13]

using two DISA 55M01 bridges, two TSI linearizers and DISA 55P51 x-wire probe as elaborated in ref. [13].

Computational setup

Due to ZPG on inner wall, the potential flow velocity on the inner wall was constant, $U_{pw} \approx 16\,m/s$ which can also be taken as the free stream velocity in the straight section. From the experimental data of [13], at station 1 (s = -71.75 cm), momentum thickness, $\theta = 0.0037$ m, free stream velocity, $U_\infty = 16$ m/s and momentum thickness Reynolds number $Re_\theta = 3802 = U_\infty \theta / \nu$ which gives the kinematic viscosity $\nu = 1.557 \times 10^{-5}\,m^2/s$. Similarly, at station 2 (s = -41.27 cm), momentum thickness, $\theta = 0.00439$ m, free stream velocity, $U_\infty = 16$ m/s and momentum thickness Reynolds number $Re_\theta = 4517 = U_\infty \theta / \nu$ which gives the kinematic viscosity $\nu = 1.554 \times 10^{-5}\,m^2/s$. Thus, the kinematic viscosity was determined to be $\nu = 1.555 \times 10^{-5}\,m^2/s$ and based on the duct height, D = 15.24 cm, the Reynolds number is calculated to be $Re = U_\infty D / \nu = 1.568 \times 10^5$. The reference values set in DLR-TAU solver are shown below which are in SI units.

```
References --------------------------------------------------: -
            Reynolds number: 1.562e+5
            Reynolds length: 0.152
            Reference velocity: 16
            Reference temperature: 298
```

This testcase is slightly more complicated as details of the geometry weren't readily available in the publications. Using the static-pressure distributions provided, an approximate 2D geometry was constructed using Pointwise meshing software with a development length of 2.59 m and duct height of 0.1524 m. A slight tapper was provided to the upperwall such that a zero pressure gradient is established on the lower wall in the straight section. To reduce the pressure drop on the inner wall, a small section of the outer wall at beginning of the curvature was assigned with an inviscid euler wall boundary condition whereas the rest of walls were assigned with a regular viscous wall boundary condition. The inviscid wall region mimics the porous suction wall in the experiment as shown in fig. 4.4. 'Reservoir-pressure-inflow' and 'Reservoir-pressure-outflow' boundary conditions are used for inlet and outlet in DLR-TAU. A total of 200×748 grid points were taken in wall normal and streamwise direction respectively with a minimum wall-normal spacing of 5×10^{-6} m that corresponds to $y^+ \approx 0.2$. The positions of all measuring stations on the inner wall are described in fig. 4.3a. The SA-RC, SST-RC and SSG/LRR-ω were mainly used to develop the geometry.

On the convex wall/inner wall, the streamwise positions s < 0 correspond to the flat development region, $s \in (0, 70.68)$ cm is the curved region and s > 70.68 cm is the flat recovery region downstream
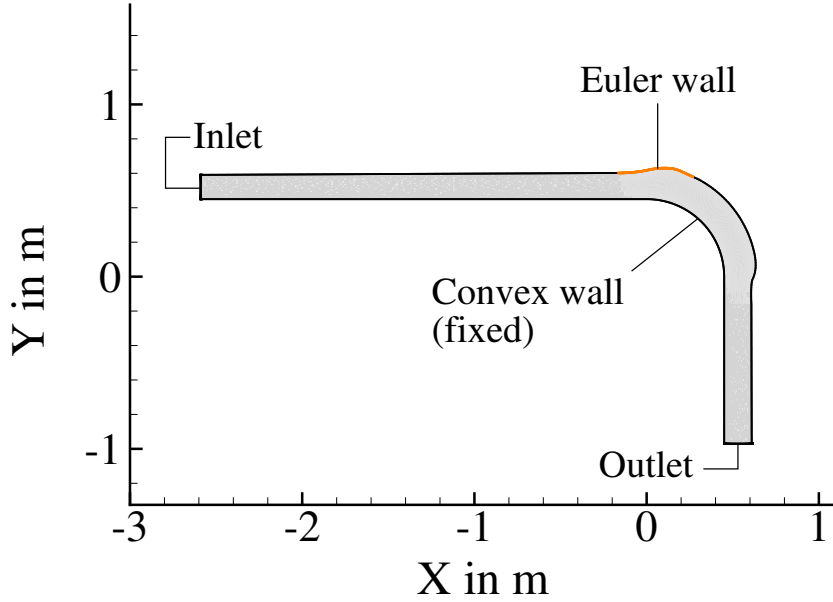
Figure 4.4: Geometry of the CFD domain of two dimensional Gillis-Johnston experiment [13] with inviscid euler wall shown in orange line and viscous wall everywhere else

of the curvature. The duct was bulged in curved region by adjusting grid points of outer wall such that static pressure changes are well below 5% on the convex wall. This was achieved using an iterative gradient-based optimisation as elaborated in the Appendix (A.1). The resultant static pressure distribution obtained is in good agreement with the experimental measurements as shown in fig. 4.5. Coefficient of pressure is calculated relative to the position s = 0 using eq. 4.2.

$$C_p = \frac{p - p_{s=0}}{\frac{1}{2}\rho U_{\text{ref}}^2} \tag{4.2}$$

The parameters in DLR-TAU solver were determined such that the simulation matches mean velocity, boundary layer thickness (δ), skin friction coefficient (C_f), displacement thickness (δ^*) and momentum thickness (θ) of the experiment as shown in figure 4.6. Line profiles of C_f, δ^*, and θ show a constant pattern of different between the models. RSM model gives slightly higher values of the above parameters. For the boundary layer thickness shown in fig. 4.6c, the values of SST and SSG/LRR-ω are closer to each other while SA model produces slightly higher results. Present setup is a compromise to match C_f, δ^*, θ, δ_{99}, and the profiles for mean velocity and Reynolds stresses.
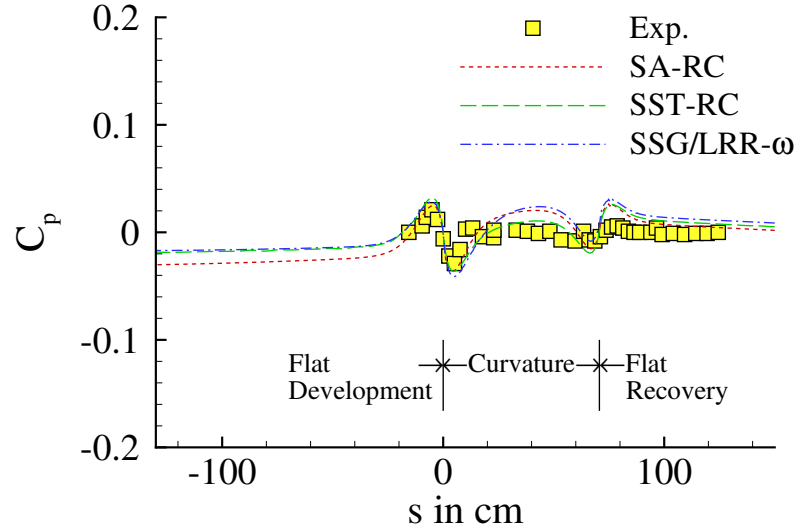
Figure 4.5: Static pressure distribution on the convex wall

(a) Skin friction coefficient using different turbulence models

(b) Displacement thickness (δ^*, solid lines) and Momentum thickness (θ, dashed, dash-dot lines)

(c) Boundary layer thickness calculated using different methods
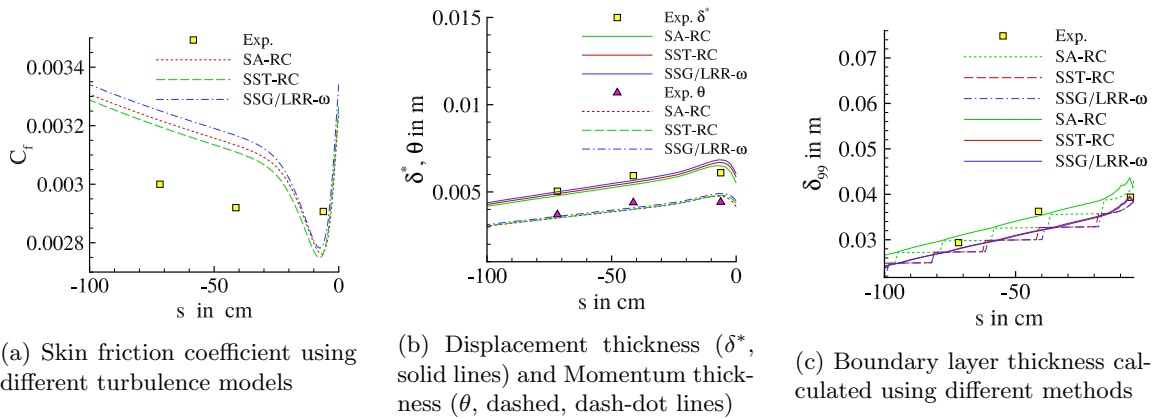
Figure 4.6: Validation of surface parameters in straight section of the duct for Gillis-Johnston case

Mean velocity and Reynolds shear stress were mainly used to validate the CFD simulation results in the development region. In station 1 at streamwise distance of s = -71.75 cm, profiles were extracted using wall-normal lines in DLR-TAU profiling tools. Turbulence models SA-RC, SST-RC, SSG/LRR-ω were used in validation of the development region. Although, the rotation-corrections of SA, SST models are only activated in the curved region, it is mentioned here for the sake of completeness.
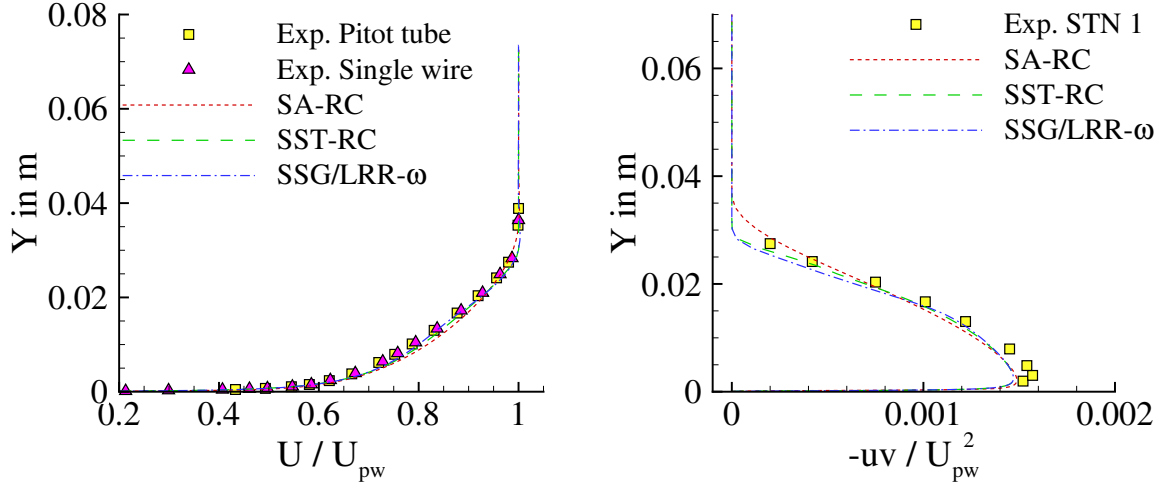
(a) Mean velocity normalised with potential flow velocity at wall (U_{pw}) for station 1 with both

(b) Reynolds shear stress normalised with U_{pw} for station 1

Figure 4.7: Normalised Profiles of mean velocity and Reynolds shear stress for station 1 at streamwise distance s = -71.75 cm

The profiles of mean-velocity for stations 1 and 2 show a very good agreement with the experimental results. The thickness of boundary layer, peak values, profiles of Reynolds shear stress are well captured by the turbulence models for this geometry. Results of SSG/LRR-ω and SST are slightly closer to each other. This can be observed in the Reynolds shear stress in figs. 4.7b, 4.8b. However, all models predict good results with respect to experimental data in the straight region of the duct.
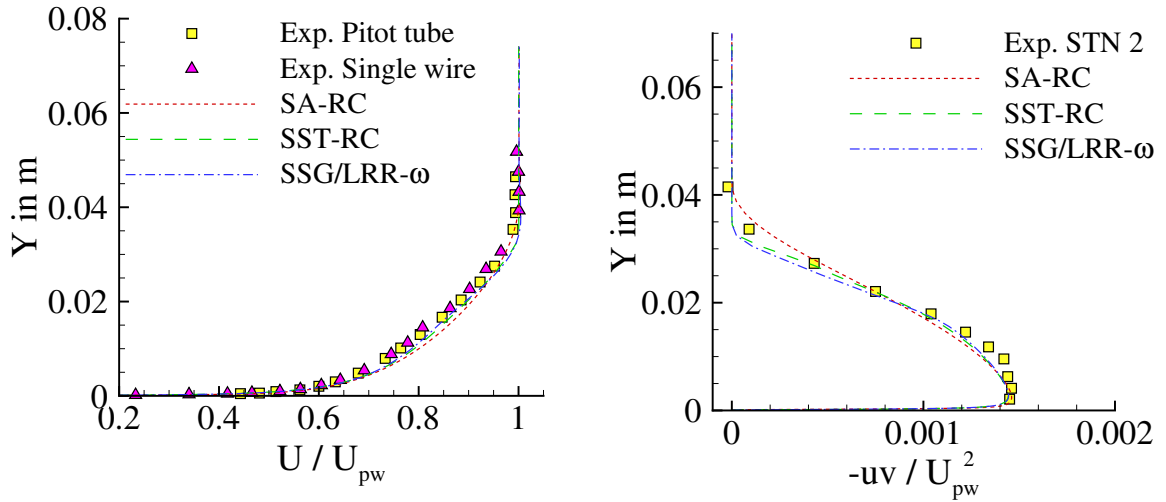
(a) Mean velocity normalised with potential flow velocity at wall (U_{pw}) for station 2 with both pitot tube and Single wire measurements

(b) Reynolds shear stress normalised with U_{pw} for station 2

Figure 4.8: Normalised Profiles of mean velocity and Reynolds shear stress for station 2 at streamwise distance s = -41.27 cm

4.1.3   So & Mellor (1973)

Experimental setup

In this experiment, a curved-wall tunnel was constructed with duct height of 6 inches (15.24 cm) and spanwise width of 4 ft (122 cm) which gives an aspect ratio of 8:1. Upstream of the test section, a 6 layer honeycomb structure is used followed by a 6:1 ratio contraction chamber. Then the flow enters the rectangular test section. A 4 ft(122 cm) long flat section for the development of the turbulent boundary layer followed by a curved region with varying radius of curvature and a 90° bend with exit diffuser, fan and motor housing for suction as shown in fig. 4.9. The wall of curved test section was adjusted based on the following configurations: 1) Convex ZPG, 2) Convex APG and 3) Concave ZPG. The setup was run at Reynolds number, Re = 4.37 $\times 10^5 \text{ft}^{-1}$ based on reference entrance test velocity which is approximately equal to 1.4337 $\times 10^6$ for reference length of 1 m. In the configurations of convex ZPG and APG, the inner wall was fixed and the outer wall was adjusted to vary the static pressure distribution on the inner wall whereas the outer wall was fixed and inner wall was adjusted for the concave test configuration. Using yaw measurements closer to the center line of spanwise width, it was shown that the extent of secondary flows was minimal thus making the two-dimensional assumption valid [40].

At the beginning of curvature, static-pressure increases drastically on the concave wall up to 23% of reference dynamic head and thereafter remains constant throughout the curvature region. The inner wall was adjusted to maintain the pressure constant on the Concave wall. Radius of curvature was continuously increased which offers a smooth transition from straight section to the curved region. This gave a curvature ratio, $\delta/R \approx 0.08$ for the convex and 0.1-0.2 for concave configurations depending on the spanwise location due to the presence of longitudinal vortices on the concave walls. Turbulence measurements were taken using hot-wire technique and is elaborated in Ref. [39]. There is one special design criterion for the case by So and Mellor worth mentioning. The radius of curvature is not constant. Instead, R is continuously changing to keep δ/R approximately constant. The values for R are given at a discrete number of streamwise positions i.e. geometry is built using different sectors of constant radii (see Figure 4.10a).
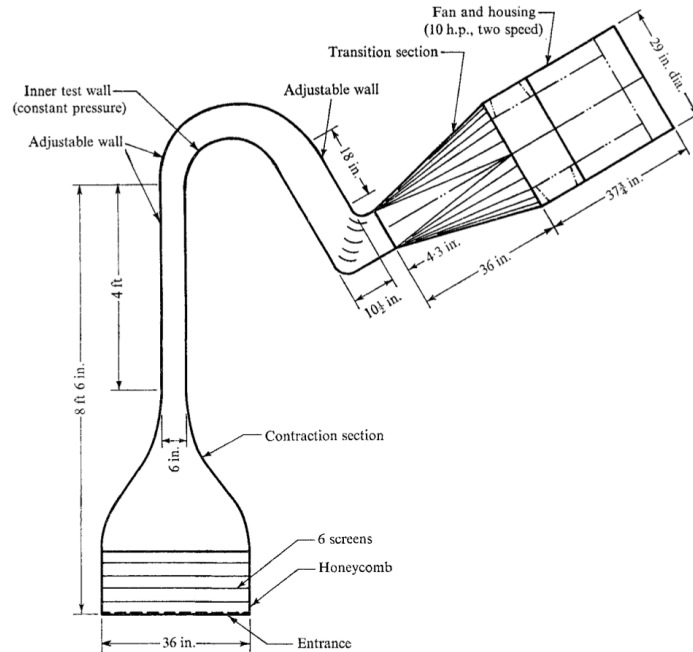
Figure 4.9: Layout of experimental setup of So and Mellor Convex configuration from Ref. [40] with spanwise width of 4 ft.
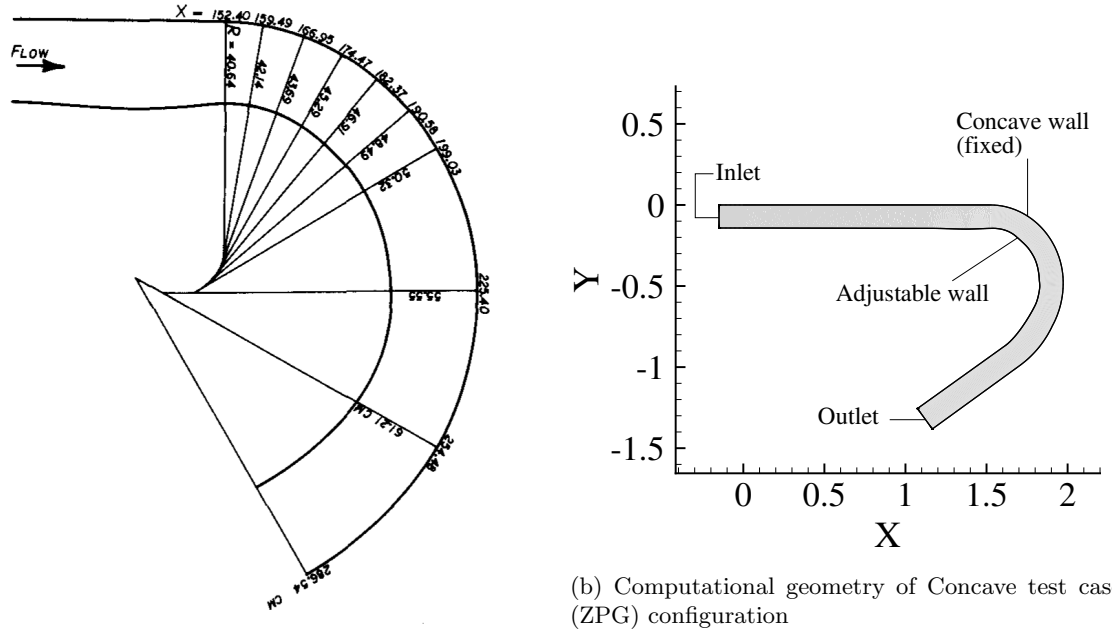
(a) Experimental geometry of Concave test section (ZPG) with measurements in cm from Ref. [41]

(b) Computational geometry of Concave test case (ZPG) configuration

Figure 4.10: Comparison of Experimental setup and Computational setup for So-Mellor Concave test case

Computational setup

From the experimental data of Ref. [41], at station 1 (s = 0.61 m), the mean streamwise velocity is approximately 21.5 m/s with a Reynolds number, Re = 1.437 $\times 10^6$ per 1 m reference length. Kinematic viscosity was calculated from this using, $\nu = U_\infty 1\,m/Re = \frac{21.6 \times 1}{1.437 \times 10^6} \approx 1.5 \times 10^5\,\mathrm{m^2}/s$. For the present geometry, with a duct height of H = 0.1524 m, Reynolds number was calculated as $Re = \frac{21.5 \times 0.1524}{1.5 \times 10^{-5}} \approx 2.2 \times 10^5$. The highest C_f was observed on the concave curvature case at stations 4 and 5, $C_f = 0.0054$ from Ref. [41]. Using the formula for wall-normal spacing from eq. 4.1, with $y^+ = 0.4$, H = 0.1524 m, $Re = 2.2\,E + 5$ and $C_f = 0.0054$, first grid point spacing was calculated to be $\Delta y_1 \approx 5 \times 10^{-6}$ m. 'Reservoir-pressure-inflow' and 'Reservoir-pressure-outflow' boundary conditions are used for inlet and outlet in DLR-TAU and viscous-wall boundary condition was used for both inner and outer walls. The following reference parameter settings were used in DLR-TAU solver for Concave configuration of So-Mellor's experiment.

```
References ------------------------------------------------------: -
        Reynolds number: 2.25e+5
        Sutherland reference viscosity: 1.91e-5
        Reynolds length: 0.1524
        Reference velocity: 22.0
        Reference temperature: 293.15
```

An approximate 2D geometry with a straight section of 1.674 m, followed by the curved section of 150° bend and a 0.45 m flat recovery region was developed using Pointwise meshing software. The fixed wall of the curved region was developed by adding sector of gradually increasing radii as shown fig. 4.10a. The curved for adjustable wall was developed using a gradient-based optimisation technique where design suggestions were taken for an iterative-step development of the geometries for each configuration as elaborated in Appendix (A1). The coefficient of pressure was considered
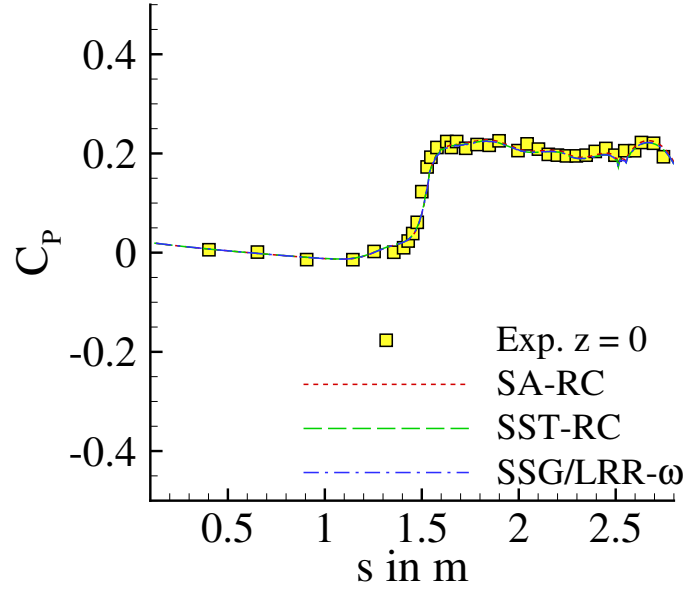
Figure 4.11: Comparison of Static pressure distribution of RANS models and So-Mellor experiment (at spanwise position z = 0, i.e. centreline) where curvature starts from s = 1.5 m

mainly from 3 RANS models to finalize the geometry. A grid of 535×100 points was used in longitudinal and wall-normal direction respectively. A comparison of geometries of the experiment and computational domain are shown in fig. 4.10.

The curved region starts at streamwise position, s = 1.5 m where the static pressure raises by almost 23% and thereafter remains constant. Experimental data from spanwise location z = 0 m, which denotes the centre line of the duct in spanwise direction. Minor differences have been observed in experimental data of static-pressure distributions on the concave wall at different spanwise locations elaborated in Ref. [41]. SA-RC, SST-RC and SSG/LRR-ω models produce pressure profiles which agree well with the experimental measurements as shown in fig. 4.11 which justifies the geometry of curved region for this testcase.

(a) Skin friction coefficient using different turbulence models

(b) Displacement thickness (δ^*, dashed, dash-dot lines) and Momentum thickness (θ, solid lines)

(c) Boundary layer thickness calculated using different methods
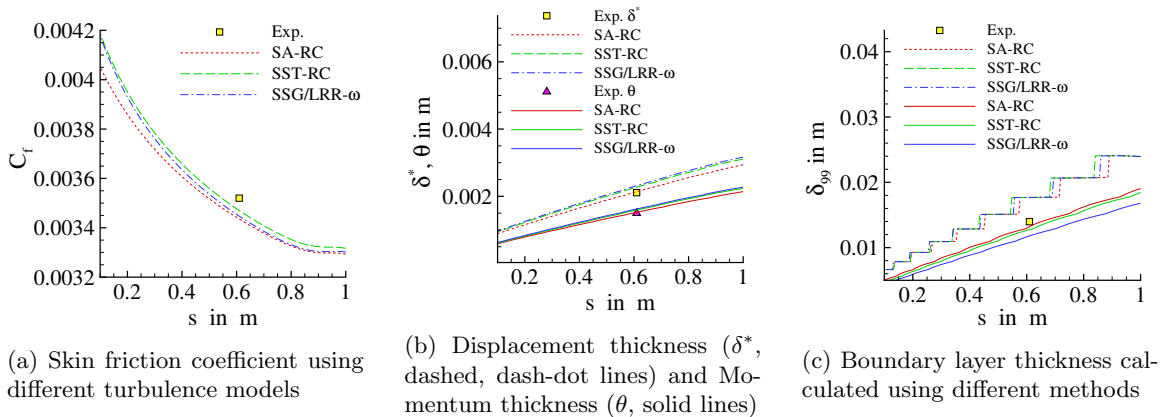
Figure 4.12: Validation of surface parameters in straight section (at station 1, s = 0.61 m or 24 inches) of the duct for So-Mellor test case

In the straight section, the surface quantities were only available at one station (s = 0.61 m) in the experimental data which was used to validate the current geometry and inlet development

length. Profiles of skin-friction coefficient, displacement and momentum thickness and boundary layer thickness show a good agreement with the experimental data as shown in fig. 4.12.
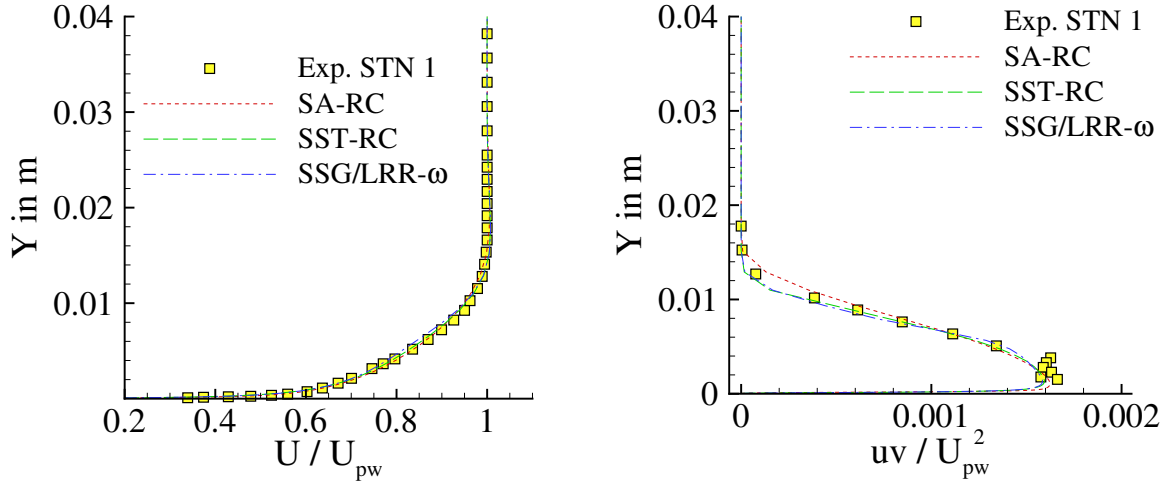
(a) Mean velocity normalised with potential flow velocity at wall (U_{pw}) for station 1

(b) Reynolds shear stress normalised with U_{pw} for station 1

Figure 4.13: Normalised Profiles of mean velocity and Reynolds shear stress for station 1 at streamwise distance s = 0.61 m (24 inches)

The normalised profiles of mean velocity from RANS models SA-RC, SST-RC and SSG/LRR-ω in fig. 4.13a show good agreement with the experiment measurements. The development length was varied and increased by 15 cm compared to the experimental setup to achieve a good match for thickness of boundary layer, the overall profile of mean velocity with respect to the experiment. Hence, the length of the flat wall inlet section was 1.674 m in the modified computational set-up. Normalised profiles of Reynolds shear stress in fig. 4.13b show good agreement with the experimental data with respect to the diffusion of Reynolds shear stress and also the peak values closer to the wall.

Chapter 5

Sensitivity study of Richardson Number
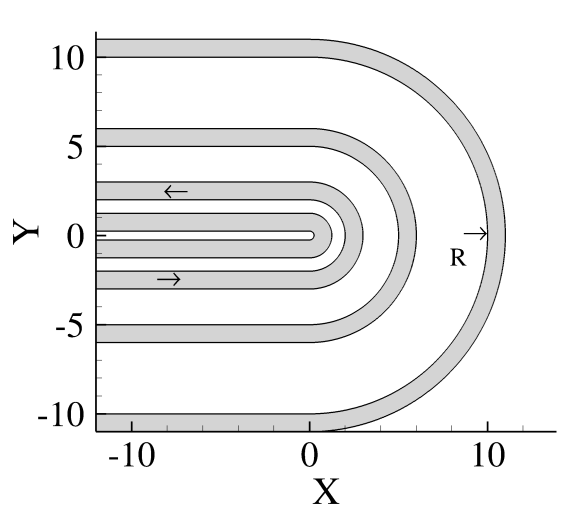
Figure 5.1: Geometries of different test cases of U-duct with varying radii of inner bend $R = D/2$, $4D$, $10D$ and $20D$

5.1 Test cases with varying curvature in a U-turn

The U-duct test from [23] which was elaborated in the chapter 4 is considered to study the effects of Richardson number with varying magnitude of curvature. The ratio of boundary layer thickness (δ) to radius of curvature (R) is considered to perform a validation study to compare the Richardson number by Bradshaw (see eq. (3.4)) and the local definition of the Richardson number by Ströer (see eq. (3.24)). Five test cases of U-duct were developed with the inner radius of the bend (R) as a function of the half-height (D) of the duct. Here, the boundary layer thickness at the end of the development region of the duct (i.e. s = -4H) was observed to be 25% of the whole duct height. So, $\delta \approx D/2$ and approximate curvature magnitudes δ/R were calculated for each test case and shown in the table 5.1.

Keeping the duct height constant, the inner radius of the bend (R) was parameterized as a function of the half-height of the duct (D). CFD domains of R = D/2 (strong curvature), R = D, R = 4D, R = 10D, R = 20D (weak curvature) were developed and simulated in DLR-TAU using

R/D	δ/R	Curvature
1/2	1	very strong
1	0.5	very strong
4	0.125	strong
10	0.05	moderate
20	0.025	mild

Table 5.1: Test cases of different U-ducts with varying curvature
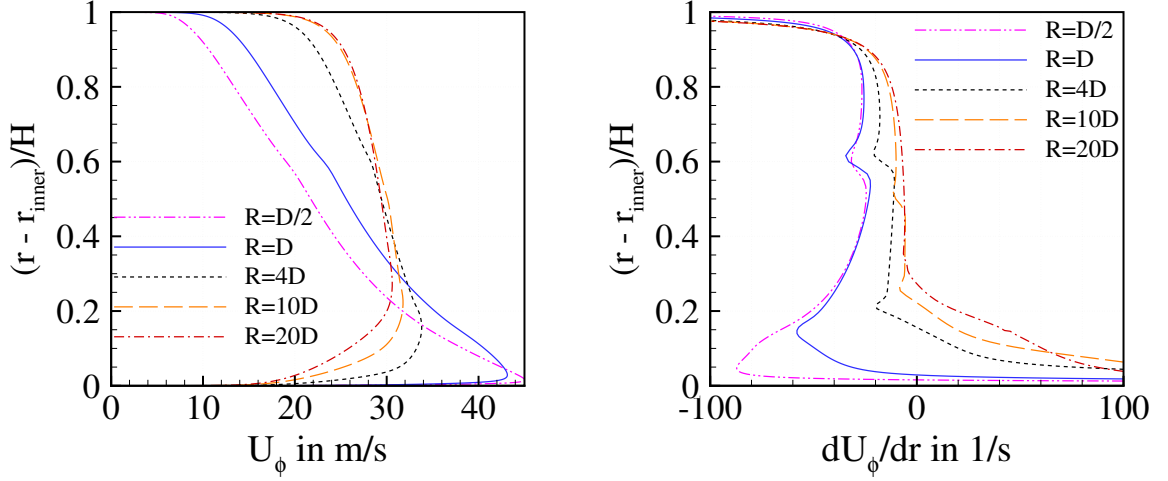
(a) Azimuthal velocities (U_ϕ) of different test cases of U-duct with varying radii of inner bend $R = D/2$, D, $4D$, $10D$ and $20D$

(b) Velocity gradient (dU_ϕ/dr) of different test cases of U-duct with varying radii of inner bend $R = D/2$, D, $4D$, $10D$ and $20D$

Figure 5.2: Profiles at 90° bend with normalized radial height in y-axis where 0 denotes inner wall and 1 denotes outerwall

SA-Neg turbulence model with 'SA-RC' rotation correction for the same test case parameters of Monson [23]. The profiles at the 90° bend are plotted to understand how the values of Richardson number vary with different magnitudes of curvature.

Comparison of mean azimuthal velocity in fig. 5.2a shows the bending of mean velocity in the inviscid region in the center of duct relative to the magnitude of curvature. From the profiles of velocity shear in fig. 5.2b, the shear rapidly turns negative away from the inner wall with increments of curvature. The relative magnitudes of curvature (U/r) to shear (dU/dr) determine the effect of curvature on turbulence as specified in eq. 3.6. Fig. 5.2 indicates that the potential flow velocity outside the boundary layers is not constant in curved flows. The mean velocity gradient dU_ϕ/dr has two sources: 1) The viscous effects of the walls and 2) The presence of curvature. The so-called potential flow velocity is given

$$U_p = (1 + Ky)U_{pw} \tag{5.1}$$

Here, K $= 1/R_c$ for convex wall and K $= -1/R_c$ for concave wall where R_c is the radius of curvature [27]. The computation of potential flow velocity at wall (U_{pw}) is elaborated in Appendix A.2. Curvature causes a radial pressure gradient $dP/dr = \rho U^2/r$ (see Bradshaw's monograph [5] p.5). Hence the inviscid flow outside the viscous-effected boundary layers is not constant, but varying.
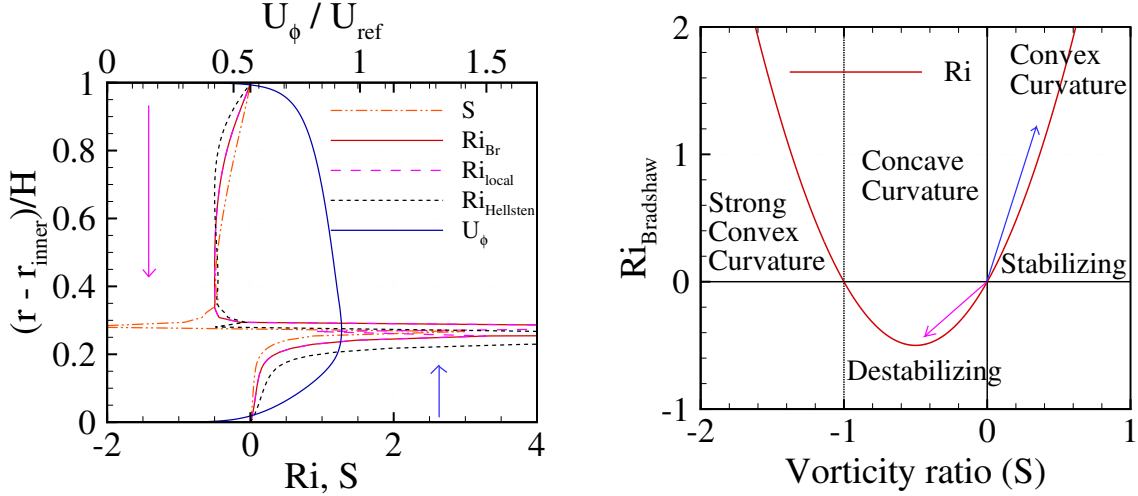
(a) Comparison of different formulations of Richardson numbers for mild curvature test case R = 20D

(b) Mapping the zones of flow at 90° bend with parabola of Richardson number

Figure 5.3: Profiles for R = 20D case at 90° bend with normalized radial height in y-axis where 0 denotes inner wall and 1 denotes outer wall

5.2 Analysis of Richardson numbers in mild curvature case, R = 20D

First consider the case of mild curvature (R=20D) in fig. 5.3a, moving away from the inner wall (following blue arrow), velocity increases and further decreases. In Bradshaw's Ri, the sign and magnitude of S determine the effects of curvature as described in fig. 5.3b. Starting at the inner wall, S is positive, in agreement with what is expected on a mildly convex-curved surface. However, the shear dU/dr becomes zero at the point where S changes sign and S becomes very high. This needs special treatment later. Starting from the outer wall, S is negative, in agreement with expected values for mild concave curvature. Inside the boundary layer of the outer wall, S is larger than -0.5, but S = -0.5 is reached in the core flow.

The point where velocity begins decreasing in radially outward direction is important as the shear turns to zero or a negligibly small value. $S = (U/r)/(dU/dr)$ and as $dU/dr \to 0$, the vorticity ratio (S) gives very high values leading to a discontinuity exactly at the point where shear turns negative. The same behaviour is observed in the Richardson number profiles which indicates the necessity of a transfer function. A mapping can be made from the zones of the 90° bend to the parabola of Richardson number. The region closer to the inner wall follows the path of convex curvature (blue arrow) and the region closer to the outer wall follows the destabilizing zone of the parabola depicting a concave region. Ri_{Br} reaches the least possible negative value i.e. -0.5 in the concave region.

Here the reference curve is Ri_{Br} and other versions of Ri are assessed by reference to Ri_{Br}. All Richardson numbers demonstrate the concave region very well within the lower limits of the parabola. Ri_{local} perfectly aligns with Ri_{Br} in the concave region. For comparison, $Ri_{Hellsten}$ slightly deviated. On the positive side, $Ri_{Hellsten}$ identifies the direction and magnitude correctly in the concave region. In the convex region, Ri_{local} perfectly aligns with Ri_{Br} and $Ri_{Hellsten}$ has slight deviations as it produces marginally higher values of curvature. Overall predictions of all Richardson number is in good agreement regarding both the sign of Ri and the magnitude of Ri for the case of mild curvature.

It is worthwhile to consider the expected sign of Ri in more detail. From a theoretical standpoint, rotation rate (Ω_z) from eq. 3.10 should denote the convex or concave curvature zone as given by the signum function in eq. 5.2. But, it also depends on the ratio of $(U/r)/(\partial U/\partial r)$ in scenarios of moderate curvature. And this formulation is not galilean-invariant due to the radius of curvature r

which is difficult to obtain in cartesian coordinate system.
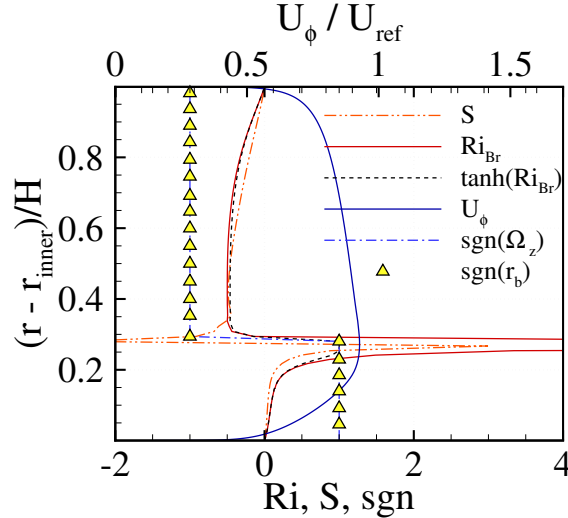
Figure 5.4: Comparing the effect of tanh function and performance of sgn(r_b) at the bend

$$\text{sgn}(\Omega_z) = \text{sgn}\left(\frac{U}{r} + \frac{\partial U}{\partial r}\right) \tag{5.2}$$

Now, we consider another indicator function for curvature; namely r_b from the Spalart-Shur rotation/curvature correction framework (see $\hat{r}$ in eq. (3.19)) given in eq. (3.21) which is a galilean-invariant framework. Fig. 5.4 demonstrates the performance of rotation-correction function for the mild-curvature. Both convex and concave zones are accurately identified.

Finally, let us comment more on the need for a transfer function. The effect of the transfer function tanh can be observed at the point where there exists a discontinuity in Richardson number. The extremely high values of Ri are clipped to give practically useful values of Ri which can be further used to modify turbulence models. Tanh(Ri_{Br}) and Ri_{Br} are in good agreement in both concave and convex regions as the transfer function produces negligible deviations with respect to the input values (Ri_{Br}).

5.3 Analysis of Richardson numbers in strong curvature case, R = D/2

For the case of U-duct with very strong curvature, where the inner radius of the bend is half of the duct half-height i.e. R = D/2, the strong effect of curvature is evident in the drastic bending on the mean velocity profile (U_ϕ) due to strong radial pressure-gradient.

Similar to the previous case, first consider the vorticity ratio (S) and the resulting prediction of curvature effects. Starting at the inner wall, S rapidly grows and reaches a maximum value close to the wall (see fig. 5.6a). Then it changes sign as the velocity starts to decrease further in wall normal direction. This sign change is much closer to the wall compared the mild curvature case of R = 20D. Above this maximum value, the values of S are smaller than -1, indicating the region of strong convex curvature. Such region was not present in the mild curvature case. Starting from the outer wall, negative values $-1 < S < 0$ are observed, in agreement with the value expected for concave wall (see purple arrow in fig. 5.5).

Moving away from the outer wall, the vorticity ratio (S) continuously decreases (follow purple arrow in fig. 5.5 surpassing the negative Ri values of parabola reaching the zone of strong-convex curvature where the Ri is positive. The values of Ri_{Br} describe a smooth transition from the concave
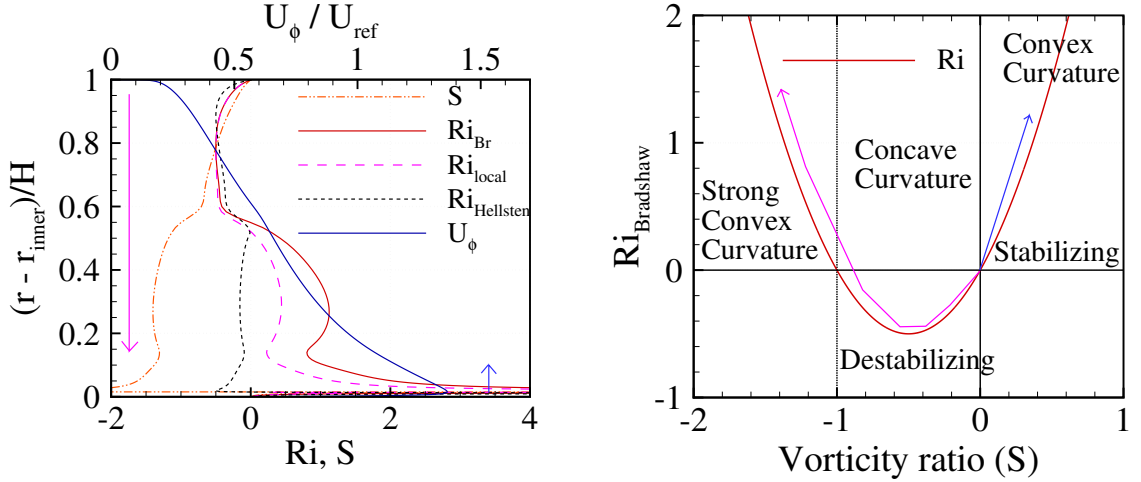
(a) Comparison of different formulations of Richardson numbers for mild curvature test case R = D/2

(b) Mapping the zones of flow at 90° bend with parabola of Richardson number

Figure 5.5: Profiles for R = D/2 case at 90° bend with normalized radial height in y-axis where 0 denotes inner wall and 1 denotes outer wall

curvature zone ($S \in (0, 1)$) to the zone of strong-convex curvature at S = -1 which is not same for the transition from concave curvature to a convex curvature at S = 0.

The region S = 0 is always involves a discontinuity which is damped by the transfer function 'Tanh'. All 3 Richardson numbers capture the physics accurately in the concave region where Ri_{local} perfectly aligns with Ri_{Br} and $Ri_{Hellsten}$ slightly deviates but lies within the lower limits of the parabola.
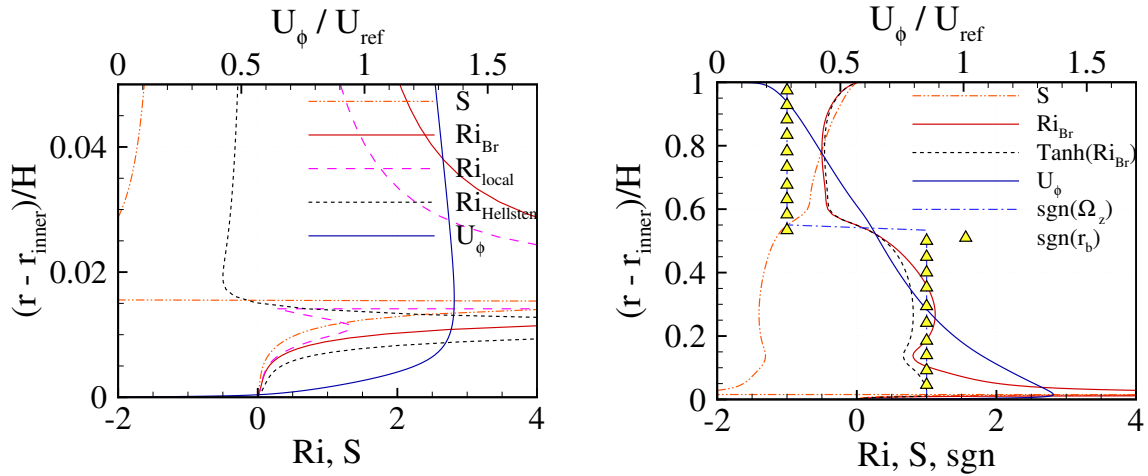
(a) Zoomed view of for mild curvature test case R = D/2 closer to the inner wall

(b) Comparing the effect of tanh function and performance of $sgn(r_b)$ at the bend

Figure 5.6: Zoomed Profiles for R = D/2 case at 90° bend and effects of signum, tanh functions

In convex region closer to the inner wall, the discontinuity of Richardson numbers due to the change in sign of velocity shear lies very close to the inner wall which is evident from the changing sign of vorticity ratio, S (orange dash-dot-dot line in fig. 5.5a) approximately at $(r - r_{inner})/H < 0.05$. A regular convex region where $Ri > 0$, $S > 0$ exists closer to the inner wall similar to the case of mild-curvature as shown in the zoomed fig. 5.6a where all 3 Richardson number give positive

values of Richardson number in agreement with the parabola. Moreover, the Ri_{local} identifies both strong-convex curvature ($S < -1$, $Ri > 0$) and regular convex ($S > 0$, $Ri > 0$) very well and is in good agreement with Ri_{Br}. Furthermore, in fig. 5.6b, both the direction sensors $\text{sgn}(\Omega_z)$ and $\text{sgn}(r_b)$ are also in good agreement for the high curvature test case which ensures robust application to complex wake flows.

In fig. 5.6, S becomes negative closer to the inner wall thus moving from convex to strong-convex region in the parabola. It is at this point Ri_{Hellsten} turns positive. So, Ri_{Hellsten} misinterprets the strong-convex zone ($S < -1$) as a concave region which is one of the drawbacks of this formula in strong curvature cases. Even though Ri_{Hellsten} remains a galilean-invariant formulation that exhibits robustness across various coordinate systems, its applicability is limited to test cases with mild curvature.

Finally, in fig. 5.6b, the action of tanh transfer function is demonstrated in the strong-convex region ($S < -1$). $\tanh(Ri_{\text{local}})$ although not shown, follows the same path because $Ri_{local} \approx Ri_{Br}$. So, even in the high-curvature test case, the tanh function helps to avoid abnormally large values obtained near the $S \rightarrow 0$ region which makes it usable for devising modifications to turbulence models.

## 5.4 Analysis of Richardson numbers in moderate curvature case, R = 10D
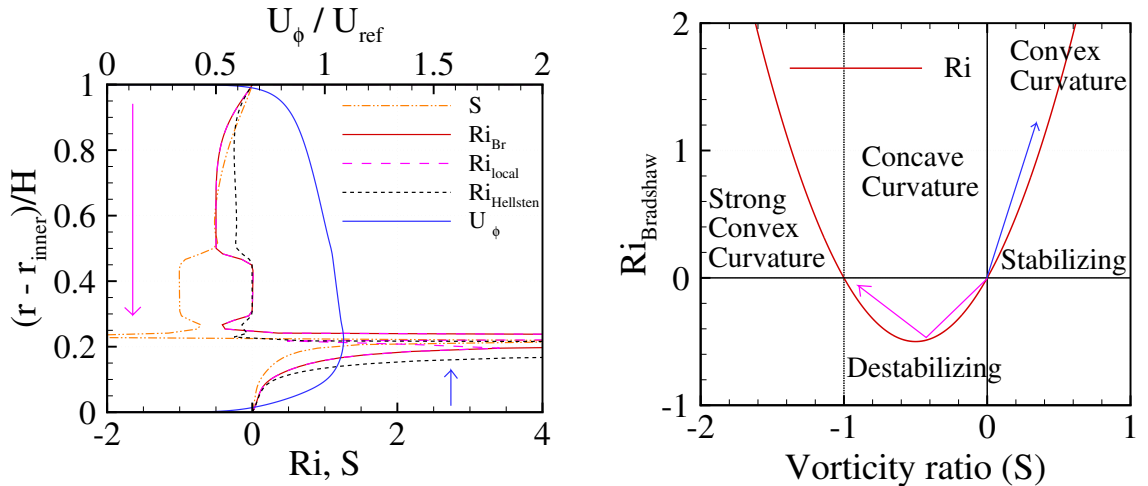
(a) Comparison of different formulations of Richardson numbers for mild curvature test case R = 10D

(b) Mapping the zones of flow at 90° bend with parabola of Richardson number

Figure 5.7: Profiles for R = 10D case at 90° bend with normalized radial height in y-axis where 0 denotes the inner wall and 1 denotes the outer wall

The case of moderate curvature is most difficult and the effect of the sign of curvature type becomes most subtle. For a case of U-duct with inner radius of the bend ten times of the duct half-height (D), i.e. R = 10D, it can be considered as a moderate curvature case. Starting from the inner wall, S grows and reaches a maximum value and then switches in sign once the velocity starts decreasing in the wall normal direction (see blue arrow in fig. 5.7). This position near the inner wall where S switches in sign for the case of R = 10D is higher than that of R = D/2 and lower than the case R = 20D which shows that this position is dependent on the magnitude of curvature.

Starting from the outer wall, S reduces following the behaviour of the concave wall with negative values of Ri. But, moving away from the outer wall, S does not venture into strong-convex region ($S < -1$) but stays at S = -1 which produces $Ri \rightarrow 0$. This suggests that for the case of moderate

curvature (R = 10D), convex and concave effects are equally stronger away from the walls of the duct.

All 3 Richardson numbers identify the concave region near the outer wall as shown in fig. 5.7a. Ri_{local} and Ri_{Br} align very well in both concave and convex regions. Although, Ri_{Hellsten} identifies the correct direction, it underpredicts the magnitude of Richardson number in the concave region as shown in fig. 5.7a.
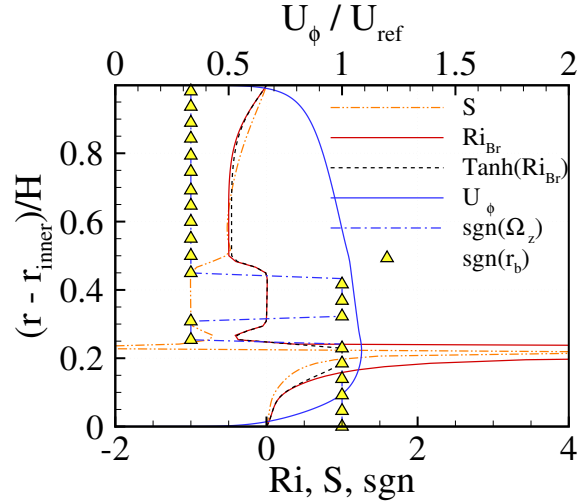
Figure 5.8: Comparing the effect of tanh function and performance of sgn(r_b) at the bend

In fig. 5.8, both the direction sensors sgn(Ω) and sgn(r_b) are in good agreement for the moderate curvature case. In cases of very strong or mild curvatures, two distinct zones of convex or concave were observed by the Richardson number and also the rotation-correction function (r_b) of Spalart-Shur [43]. But, in moderate curvature cases, a mixture of convex and concave regions are identified near the inner wall i.e. the inner 50% of duct height comprises of alternating zones of positive and negative Richardson number and r_b. Similar behaviour was also observed for the cases of $R = 4D$ and $R = 2D$. Further work needs to be done in this direction to clearly understand the action of turbulence in moderate curvature cases which can be achieved either by performing experiments or scale-resolving simulations.

Finally, in fig. 5.8, closer to the inner wall when velocity starts reducing, Ri reaches abnormally high values as $S \to 0$. Here, the effect of tanh transfer function mitigates the discontinuity in Ri thus providing usable values for modifying turbulence models.

Chapter 6

Validation of SSG/LRR-ω for wall-bounded flows with significant curvature

This section is dedicated to the validation of the RANS models SA, SST, RSM etc for the test cases described in section 4.1.

6.1 Comparison of SSG/LRR-ω with rotation correction of SA and SST

The performance of SSG/LRR-ω was compared to SA and SST models with and without rotation-correction using the validation cases for both convex and concave curvatures.

6.1.1 Testcase: Monson et al. (1990)

For the test case by Monson, experimental results are available only at the position of 90° bend in the curved region from Ref. [23]. The profiles of longitudinal mean-velocity and Reynolds shear stress at this position are shown in fig. 6.1 where the positions on the Y-axis, $(r - r_{\text{inner}})/H = 0$ and 1 refer to the inner wall and the outer wall of the bend respectively (see fig. 4.1). For the inviscid region in the center of duct, there a good agreement between the RANS solutions and experimental measurements a shown in fig. 6.1a. In Monson's test case, both convex and concave wall possess strong streamwise pressure-gradients.

First consider the concave wall. Near the concave wall ($(r - r_{\text{inner}})/H \to 1$ in fig. 6.1a), none of the RANS models show a good agreement with the experimental results inside the boundary layer. SA-RC shows a significant improvement over SA model and gives predictions closer to the experimental data than the other RANS models near the concave wall. Comparing the mean-velocity (in fig. 6.1a) near concave wall with respective Reynolds shear stress shown in fig. 6.1b, it can be clearly observed that RC modification to SA model increases turbulence production in the concave region where de-stabilizing flow occurs which brings the velocity profile closer to the experimental data.

Similar effect is also seen in SST-RC modification where turbulent stress is increased in the concave region. As a result, mean-velocity profile of SST-RC is marginally closer to the experimental data compared to regular SST in fig. 6.1a. Unlike SA-RC, rotation-correction modification cannot increase the turbulent stress too much by increasing the production term in the transport equation for turbulent kinetic energy. Higher and lower limits for the modification of turbulence production term have been introduced in SST-RC model. The lower limit was due to numerical stability issues and the higher limit was to avoid over-generation of eddy viscosity in flows with destabilizing

(a) Longitudinal velocity in U-duct at $\theta = 90°$
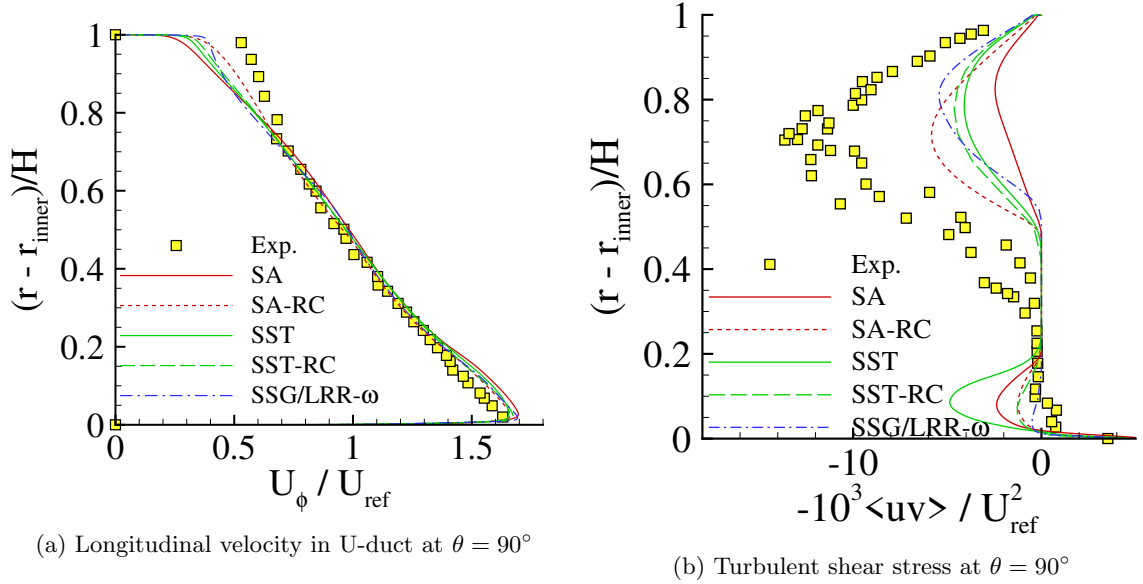
(b) Turbulent shear stress at $\theta = 90°$

Figure 6.1: Mean velocity and Reynolds shear stress of U-duct for different RANS models

curvature [38]. Less increment of turbulent shear stress in fig. 6.1b from SST to SST-RC compared to increment from SA to SA-RC is attributed to the action of limiters in production term. In Ref. [38], authors have used Monson's testcase for validation of SST-RC but have not shown the turbulent shear stress profiles of the U-duct at 90° bend which is elaborated here in detail.

Comparing the experimental profiles of mean-velocity and turbulent shear stress in fig. 6.1b, it can be inferred that the increase of turbulent stresses extends to the potential flow region for the concave wall. Likewise, the reduction of turbulent stresses is observed in the convex region even though a velocity-gradient exists away from the convex wall. This is due to the pressure gradient in radial direction which damps and augments turbulent cross stream fluctuations at convex and concave regions respectively [39].

In the concave region, SSG/LRR-ω profiles lie between SST-RC and SA-RC in fig. 6.1b and produce higher $\overline{uv}$ closer to the outer wall which are not present in eddy viscosity based RANS model simulated in the present study. This results in higher velocity closer to the wall as shown in fig. 6.1b. Moreover, the peak of $\overline{uv}$ in fig. 6.1b in the concave region which occurs at $(r - r_{inner})/H \approx 0.7$ is only best represented by SA-RC among all RANS models in the present study which proves the robustness of Spalart-Shur's rotation correction in curved turbulent boundary layers with strong streamwise pressure-gradient. Additionally, SA-RC and SST-RC show higher diffusion of turbulent shear stress in concave boundary layer in fig. 6.1b compared to SSG/LRR-ω. Note that the test case by Monson was used for the evaluation of the SA-RC modification [36]. Hence, strictly speaking, the Monson case is not a validation study for SA-RC.

In the convex region (closer to the inner wall, $(r - r_{inner})/H \to 0$ in fig. 6.1b), SST and SA overpredict turbulent shear stress. Due to the stabilizing flow effect, the outer-part of boundary layer has negligible shear stress. The effect of rotation-correction modification reduces the turbulence production closer to the convex wall thus producing smaller Reynolds shear stress and a better agreement with the experiment as shown in fig. 6.1b. SSG/LRR-ω produces smaller $\overline{uv}$ in the convex region and is marginally closer to the experiment data when compared to SA-RC and SST-RC as shown in fig. 6.1b. SA-RC and SST-RC produce very close profiles of $\overline{uv}$ due to the same Spalart-Shur's rotation correction [43].

It is worthwhile to add another comment. Reynolds shear stress values ($\overline{uv}$) were calculated from the Boussinesq hypothesis for SA and SST models i.e. using mean-strain rates whereas it can be directly obtained from the result of transport equation in RSM. It was observed that when Reynolds shear stress was calculated using Boussinesq hypothesis for RSM, it predicted higher values compared

to the solution of Reynolds stress tensor especially at the convex wall. This is another indication of the impact of the Boussinesq hypothesis. Moreover, the $\overline{uv}$ data from the experiment shown in fig. 6.1b is shows a significant spreading/scatter in the concave region and qualitatively difficult to compare RANS models. This could be attributed to the presence of Taylor-Görtler vortices on the concave wall. More test cases were simulated to understand the effects of pressure-gradients, streamline-curvature separately and validate the performance of SSG/LRR-ω in different conditions.

6.1.2 Testcase: Gillis & Johnston (1983)

For the convex curvature test case of Gillis & Johnston, 3 stations in curved region i.e. stations 4, 6 and 7 at streamwise positions s = +16.2 cm, +50.8 cm and +64.13 cm respectively are taken into consideration. Mean velocity and Reynolds shear stress profiles normalised to respective local potential flow velocity at wall (U_{pw}) are shown in figs. 6.2 and 6.3 respectively. U_{pw} was calculated using the grid points in the inviscid region and a least-squares fit as elaborated in appendix A.2.
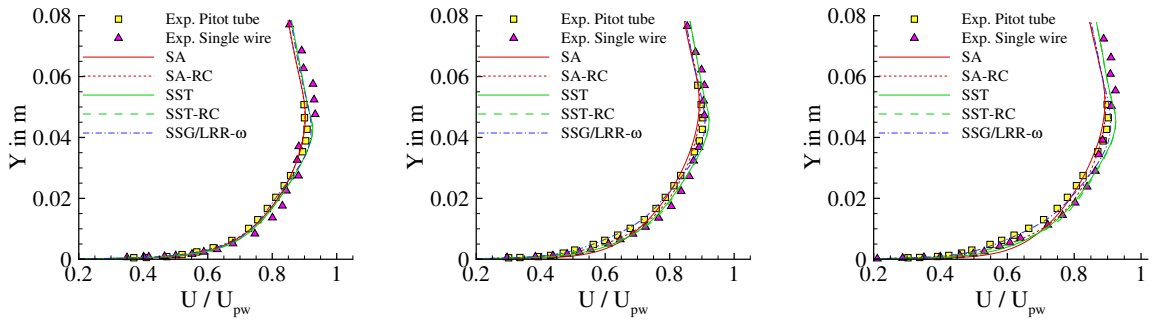
(a) Normalised mean velocity for station 4 (s = + 16.2 cm)

(b) Normalised mean velocity for station 6 (s = + 50.8 cm)

(c) Normalised mean velocity for station 7 (s = + 64.13 cm)

Figure 6.2: Normalised mean velocity profiles at stations in curved region for Gillis & Johnston's test case to demonstrate the effect of rotation correction on RANS models

In fig. 6.2, the mean velocity profiles show a very good agreement with the experiment measurements in the inviscid region away from the wall. The effect of rotation correction for SA, SST models slightly modifies the mean velocity profile especially in inner-half of the boundary layer by modifying the Reynolds shear stress. RC modifies the turbulence production term directly for SA and SST models. In fig. 6.2, minor differences between different RANS models can be observed in the inner-part of boundary layer at stations 6 and 7.
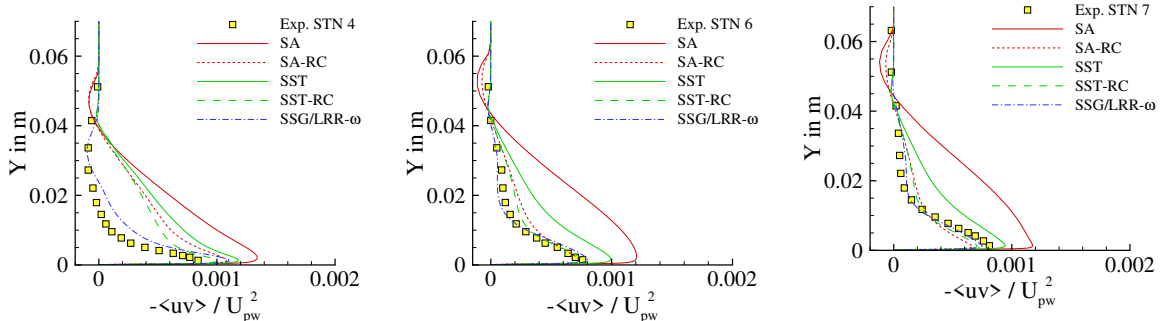
(a) Normalised Reynolds shear stress for station 4 (s = +16.2 cm)

(b) Normalised Reynolds shear stress for station 6 (s = +50.8 cm)

(c) Normalised Reynolds shear stress for station 7 (s = +64.13 cm)

Figure 6.3: Normalised Reynolds shear stress profiles at stations in curved region for Gillis & Johnston's test case to demonstrate the effect of rotation correction on RANS models

The Reynolds shear stress was calculated using Boussinesq hypothesis for SA, SST models. Normalisation was done using the local U_{pw} for each station. For the convex curve, without rotation correction, SST shows better agreement with experiment than SA. SST-RC shows better agreement with experimental data than SA-RC. RSM shows better agreement with the experimental data than both SA-RC and SST-RC. For SA and SST, the rotation correction reduces the peak values of $\overline{uv}$ closer to the wall and this effects slowly subsides away from the wall. SA and SA-RC predict negative values of $\overline{uv}$ at the edge of boundary layer and such behaviour was not observed with SST and RSM. In fig. 6.3a, the RSM shows better agreement with the experimental data than SA, SST models with rotation corrections. The response to Reynolds shear stress on the onset of curvature can be clearly observed. RSM responds more rapidly to wall-curvature for this test case whereas SA-RC and SST-RC come close to the experimental measurements in stations 6 and 7 as shown in fig. 6.3. In station 7 (fig. 6.3c), RC for SA, SST gives smaller values than the experiment where RSM shows better predictions of Reynolds shear stress.

6.1.3 Testcase: So & Mellor (1973)

The next test case considered is the curved duct by So & Mellor. It is important to highlight that Taylor-Görtler vortices can arise for flow over concave surfaces. For the configuration of Concave - ZPG, measurements of mean velocity and Reynolds shear stress are available at 2 streamwise locations i.e. s = 1.78 m and s = 2.44 m and two spanwise locations at each streamwise point. Measurements stations 2 and 3 are located at spanwise locations z = 1.7 cm and z = 3.4 cm to measure the quantities at a crest and a trough of Taylor-Görtler vortices. Similarly, at s = 2.44 m, stations 4 and 5 are located at z = 2.6 cm and z = 5.3 cm in the experimental setup [41].
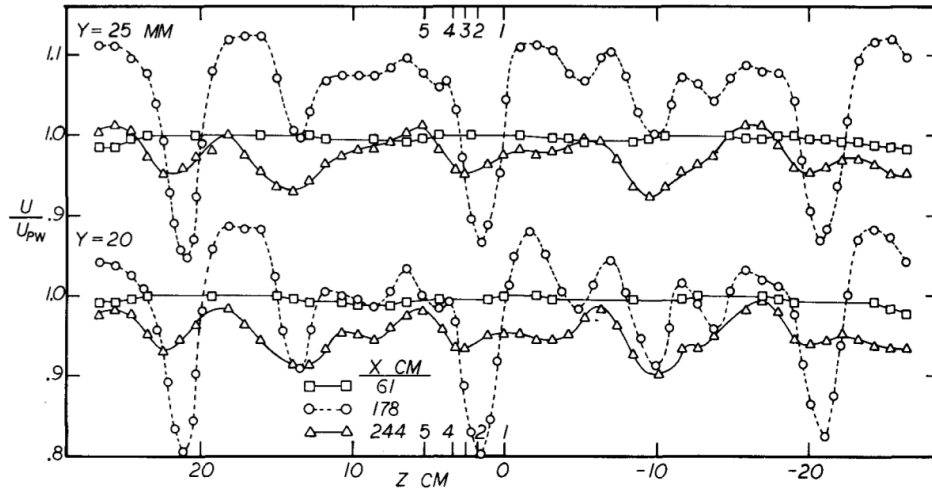
Figure 6.4: Mean transverse velocity distribution at constant wall-normal height (Y = 0.02m and 0.025 m) at different streamwise locations, s = 0.61 (squares), 1.78 (circles) and 2.44 (triangles) m (obtained from Ref. [41])

As the simulation domain is two dimensional, the streamwise locations are compared to different spanwise locations of the experiment to understand the predictions of each turbulence model. When viewed in streamwise direction i.e. a spanwise slice shows that the mean-velocity is not constant at all spanwise locations for a wall-normal height (see fig. 6.4). Due to the formation of longitudinal vortices, crests and troughs form in the spanwise profiles of mean-velocity. As shown in fig. 6.4, at streamwise position x = 61 cm, the mean velocity is same at all spanwise locations (shown by squares-sold-lines) at different wall-normal distances. But, in the curved region, the longitudinal vortices distort the mean-velocity profiles to generate a spanwise wave like structures. The first question to be answered is what is predicted by RANS models in a 2D simulation.
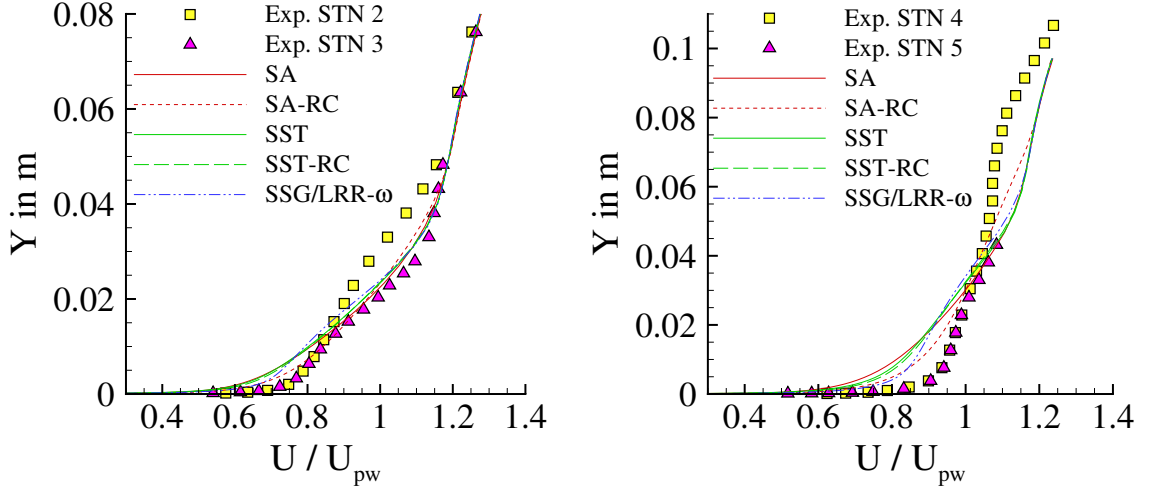
(a) Longitudinal mean velocity on concave wall at streamwise position, s = 1.78 m (stations 2,3 in exp.)

(b) Longitudinal mean velocity on concave wall at streamwise position, s = 2.44 m (stations 4, 5 in exp.)

Figure 6.5: Mean velocity profiles on So & Mellor's concave wall in curved region

In fig. 6.5a, the mean velocity profiles match with the experiment data in the inviscid region. The behaviour of mean velocity (from experiments) is different in both crest and trough of the longitudinal pairwise vortices. The mean-velocity experimental profiles very close to the wall align for stations 2-3 and stations 4-5 as shown in fig. 6.5. This exact profile closer to the wall was not captured by any of the RANS models in the present simulation. SA-RC and SSG/LRR-ω show profiles which are close to experiment values compared to SST-RC, SST and SA models. This can be attributed to the robust rotation-correction of SA-RC and second moment closure advantage of SSG/LRR-ω. As we proceed in the streamwise direction, the effect of longitudinal vortices become more intense. Experimental stations 3 and 5 denote troughs of the vortices whereas stations 2 and 4 denote the crests of the vortices. At s = 2.44 m, the boundary layer thickness increases drastically as shown in fig. 6.5b. SST-RC shows only a marginal improvement over SST due to limitation of turbulence production in the model. However, SA-RC shows a strong improvement over SA for the profiles of mean-velocity as shown in fig. 6.5.

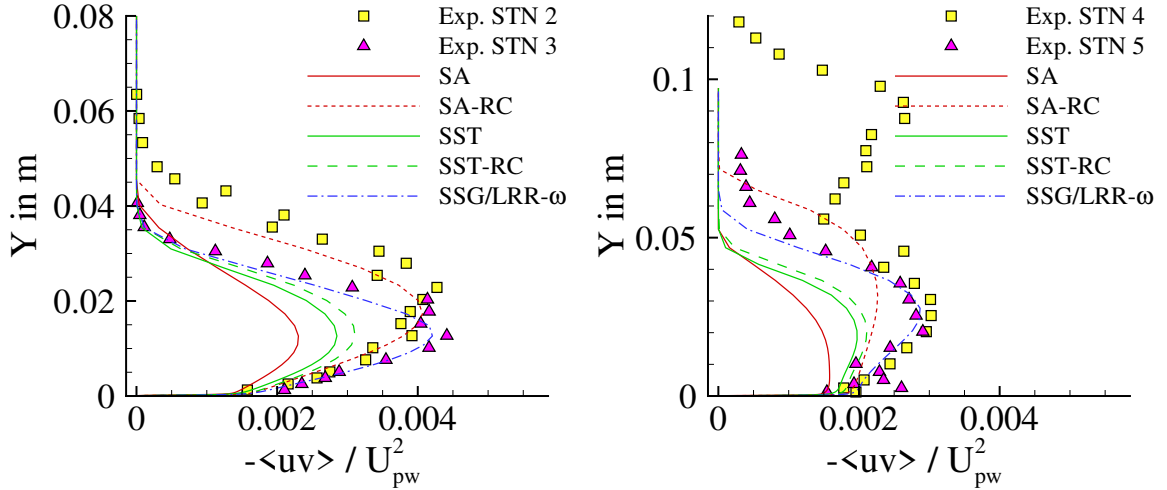Reynolds shear stress profiles for both streamwise locations are shown in fig. 6.6. SA-RC captures the shear stress of the crest of the vortex (station 2) whereas SSG/LRR-ω produces the $\overline{uv}$ profile of the trough (station 3) of the vortex as shown in fig. 6.6a. Similar behaviour is also observed for streamwise position, s = 2.44 m in fig. 6.6b.

There is good agreement for the $\overline{uv}$ of SSG/LRR-ω with the experiments in inner part of the boundary layer. The turbulent diffusion of SA-RC is higher than SSG/LRR-ω in the outer part of boundary layer as can be seen in fig. 6.6. Regarding the effects of rotation-corrections, SA-RC produces a tremendous change when compared to SA in estimating the Reynolds shear stress in both increasing the magnitude of turbulence and turbulent diffusion on a concave wall. SST-RC increases $\overline{uv}$ on the concave but only to a marginal extent due to the limiters of rotation-correction in SST-RC.

Moreover, it is a challenging task for RANS to model centrifugal instabilities that lead to longitudinal vortices. This was not investigated in detail as to whether or not RANS is able to capture Görtler vortices. It would require a 3D simulation of the same concave wall. Preliminary trials were conducted to observe such spanwise effects using a 3D spanwise-coarse version of the present So & Mellor concave test case. But, no change was observed in the mean-velocity in spanwise direction. A detailed investigation needs to be performed with finer grids to confirm the ability of RANS models to predict centrifugal instabilities. Nevertheless, SA-RC and SSG/LRR-ω perform reasonably good for such complex systems. Although, SSG/LRR-ω captures the structure of turbulent bound-

(a) Reynolds shear stress on concave wall at stream-wise position, s = 1.78 m(stations 2,3 in exp.)

(b) Reynolds shear stress on concave wall at stream-wise position, s = 2.44 m(stations 4, 5 in exp.)

Figure 6.6: Reynolds shear stress profiles on So & Mellor's concave wall in curved region

ary layer reasonably well compared to eddy-viscosity based RANS models, there is some room for improvement in terms of turbulent diffusion.
'

6.2 Study of details of second moment closure modeling: Convex curvature

In this section, the details of the second moment closure model are changed in order to study the sensitivity of the model predictions. The following modelling details are studied:

- The turbulent diffusion model (SGDH vs GGDH)

- The redistribution model (SSG blended with LRR, LRR and SSG)

Differential Reynolds stress model (SSG/LRR-ω) uses LRR model in the inner $\approx 60\%$ of boundary layer and SSG in the outer part of the boundary layer with ω as a blending function. To understand the effect of re-distribution model in boundary layers with streamline curvature, SSG, LRR and SSG/LRR-ω models are compared for different testcases of convex and concave curvatures. In fig. 6.7 and 6.8, the mean-velocity and Reynolds shear stress profiles for the stations 6 and 7 of curved region in Gillis & Johnston's experiment are shown. The Generalized Gradient Diffusion Hypothesis (GGDH) was used to model the turbulent transport term for three redistribution models SSG, LRR and SSG/LRR-ω unless specified otherwise.

6.2.1 Mean flow and Reynolds stresses

Effect of redistribution model

In the inner part of the boundary layer, the profiles of three redistribution models are very close and agree well with the experiments but in the outer-part of boundary layer, where the stabilizing effect of strong convex curvature is dominant, SSG/LRR-ω performs well in both predicting the magnitude of $\overline{uv}$ and diffusion of $\overline{uv}$ (see fig. 6.8). SSG produces less diffusion of $\overline{uv}$ which can be observed by the profiles in outer-part of the boundary layer as shown in fig. 6.8. LRR produces slightly higher diffusion of turbulent shear stress than SSG model but SSG/LRR-ω shows a better agreement with
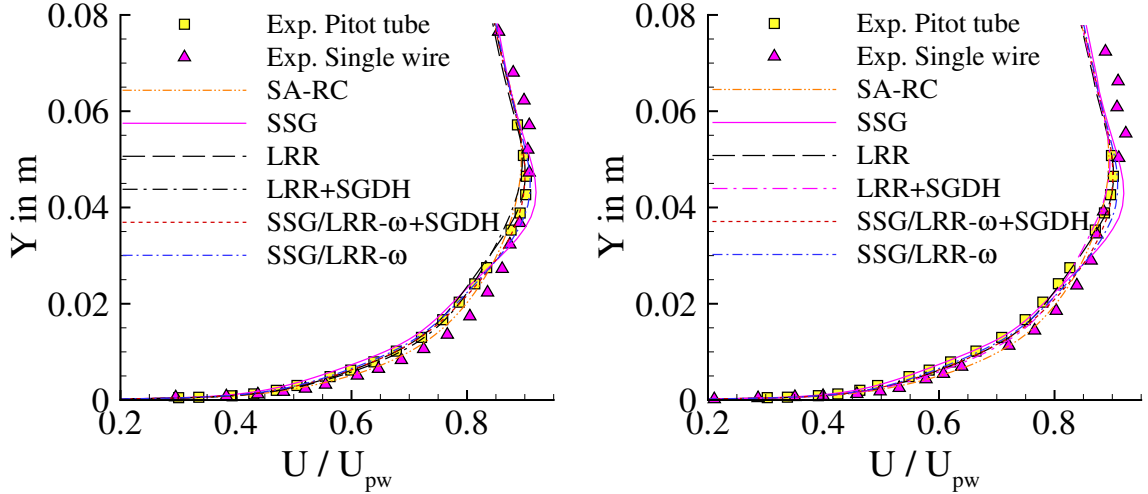
(a) Normalised mean-velocity for station 6 (s = + 50.8 cm)

(b) Normalised mean-velocity for station 7 (s = + 64.13 cm)

Figure 6.7: Normalised mean-velocity profiles at stations in curved region for Gillis & Johnston's test case to demonstrate the effect of redistribution models for convex curvature with ZPG

the Reynolds shear stress profiles of the experiment. SSG/LRR-ω captures the right magnitude of $\overline{uv}$ to estimate accurate structure of turbulence in convex curvature and a good estimate of turbulent diffusion which is evident from the profiles in the outer-part of the boundary layer(see fig. 6.8). The mean-velocity profiles shown in fig. 6.7 also suggest that SSG/LRR-ω provides a better agreement with the experimental data compared to standalone SSG or LLR redistribution models.

To conclude, the blended redistribution model of SSG/LRR gives the best agreement with the experimental data among the different redistribution models tested.

Effect of diffusion model in Transport term

LRR and SSG/LRR-ω were simulated with SGDH for the Turbulent transport term for the same test case to understand the effect of diffusion model in transporting turbulence shear stress. SGDH in turbulent transport for both LRR and SSG/LRR-ω models leads to higher diffusion of turbulent shear stress in the boundary layer (see fig. 6.8). This suggests that the Generalised Gradient Diffusion Hypothesis (GGDH) gives better agreement with the experimental data than Simple Gradient Diffusion Hypothesis (SGDH) for modelling turbulent transport in convex curved turbulent boundary layers.

There is some theoretical support for this observation. It is the $\overline{vv}$ component which governs the wall normal turbulent transport in the GGDH model. The component $\overline{vv}$ is highly affected by curvature, as described in Durbin [11] p. 164. Hence the additional physics of the GGDH using the $\overline{vv}$ component can be expected to yield better prediction of the turbulent transport. This will be described in detail when the Zeman modification for the turbulent transport is reviewed, see Appendix A.3.1.

(a) Normalised Reynolds shear stress for station 6 (s = +50.8 cm)

(b) Normalised Reynolds shear stress for station 7 (s = +64.13 cm)

Figure 6.8: Normalised Reynolds shear stress profiles at stations in curved region for Gillis & Johnston's test case to demonstrate the effect of redistribution models for convex curvature with ZPG
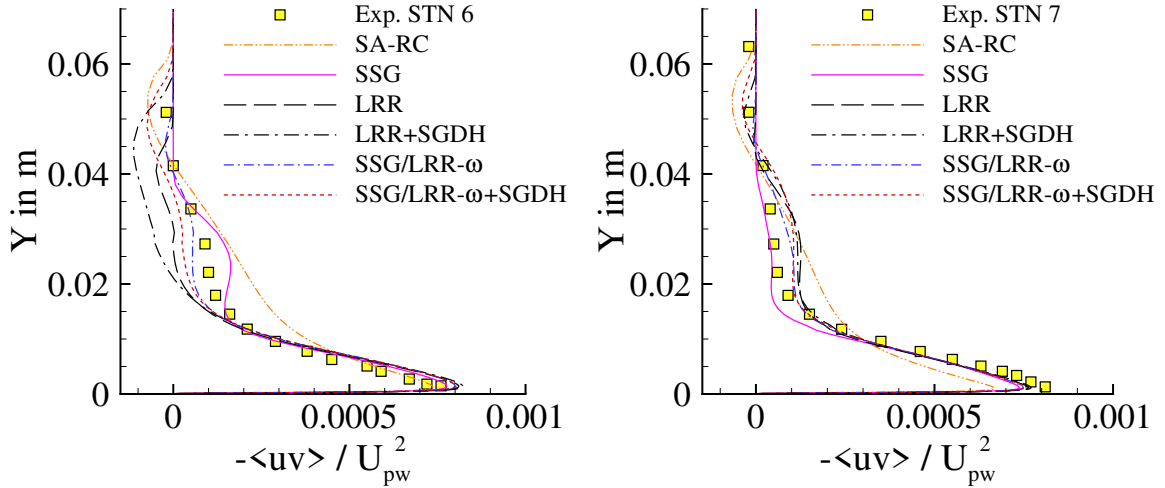
6.2.2 Streamwise Evolution of Reynolds stress anisotropy in convex curved Boundary Layers
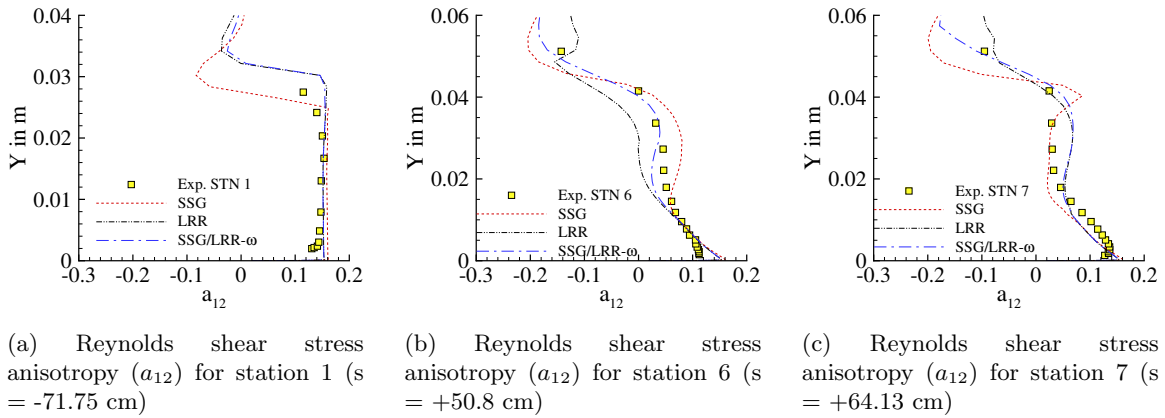
(a) Reynolds shear stress anisotropy (a_{12}) for station 1 (s = -71.75 cm)

(b) Reynolds shear stress anisotropy (a_{12}) for station 6 (s = +50.8 cm)

(c) Reynolds shear stress anisotropy (a_{12}) for station 7 (s = +64.13 cm)

Figure 6.9: Streamwise evolution of Reynolds shear stress anisotropy using different redistribution models for Gillis & Johnston's test case

To understand how different redistribution models predict turbulent shear stress distribution in curved turbulent boundary layers, anisotropy of Reynolds shear stress (a_{12}) was calculated using eq. 6.1 and it's streamwise evolution was shown at different stations in fig. 6.9.

$$a_{ij} = \frac{\overline{u_i u_j}}{q^2} - \frac{\delta_{ij}}{3}, \ a_{ss} = 0$$
$$a_{12} = \frac{\overline{uv}}{\overline{uu} + \overline{vv} + \overline{ww}}$$

(6.1)

The y-axis is shown in dimensional units to directly compare the evolution of anisotropy inside the boundary layer with the experiment. From the experiment, in the straight section of the duct, it

can understood that anisotropy of turbulent shear stress is almost constant at $a_{12} = 0.15$ throughout the boundary layer and turns to zero in the free-stream where turbulence is isotropic (see fig. 6.9a. In fig. 6.9a, all three redistribution models perform well where LRR and SSG/LRR-ω have closer profiles which agree well with the experiment both in terms of magnitude of a_{12} and thickness of boundary layer (height where a_{12} goes to zero).

In curved region, shown in fig. 6.9b and 6.9c, anisotropic parameter, a_{12} varies from ≈0.15 (at the wall) to ≈-0.1 (outer-part of boundary layer) for convex curvature without streamwise pressure-gradient where the largest changes have been observed in the outer-part of boundary layer. This suggests that stabilizing curvature reduces production of turbulence energy and the overall Reynolds stress anisotropy mainly in the middle and outer-parts of the boundary layer. This structure of turbulent shear stress in a curved boundary layer is better captured by SSG/LRR-ω than individual SSG and LRR redistribution models as shown in fig. 6.9b. LRR profile in fig. 6.9b shows that the pressure-strain correlation of LRR suppresses turbulence production more than SSG and SSG/LRR-ω.

6.3 Study of details of second moment closure modeling: Concave curvature

This section describes the findings for the concave curvature case and gives a brief discussion of concave curvature effects.

6.3.1 Mean flow and Reynolds stresses
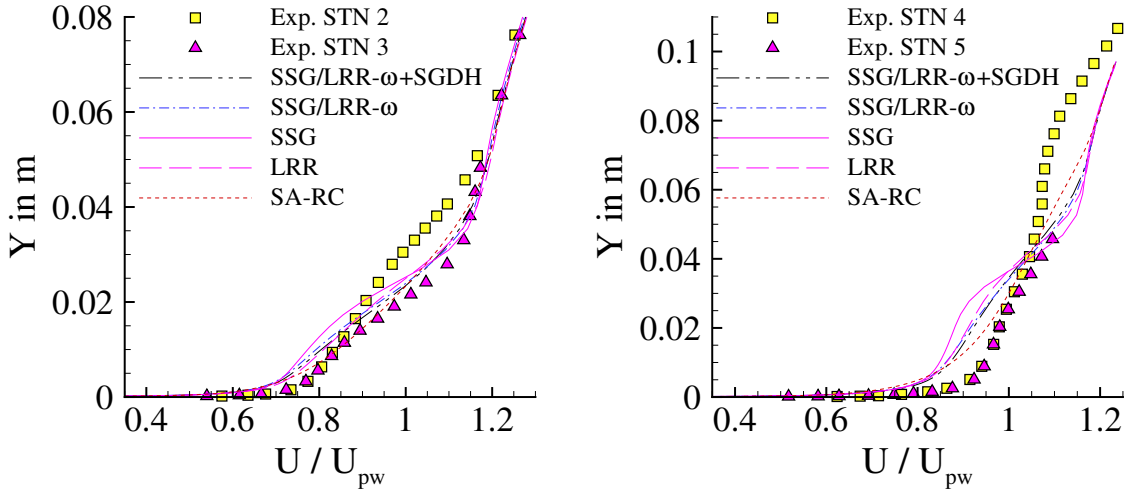
(a) Longitudinal mean velocity on concave wall at streamwise position, s = 1.78 m (stations 2,3 in exp.)

(b) Longitudinal mean velocity on concave wall at streamwise position, s = 2.44 m (stations 4, 5 in exp.)

Figure 6.10: Mean velocity profiles of different redistribution models for So & Mellor's concave wall testcase in curved region

In figs. 6.10 and 6.11, the mean-velocity and Reynolds shear stress profiles are shown for the stations in curved region of So & Mellor concave experiment. The three redistribution models SSG, LRR and SSG/LRR-ω use Generalized Gradient Diffusion Hypothesis (GGDH) to model the turbulent transport term unless specified otherwise. These models with same diffusion model in Turbulent transport term are compared for concave curvature without streamwise pressure-gradient.

Effect of redistribution model

$\overline{uv}$ profiles in fig. 6.11 show that SSG produces higher magnitudes of turbulent shear stress in the middle part of the boundary layer at both streamwise locations which can be directly attributed to the smaller diffusion in the outer-part of boundary layer. So, the same amount of turbulent shear stress is spread across smaller region. LRR model produces $\overline{uv}$ that agrees well with experiment but still has less diffusion in the outer-part of the boundary layer for So & Mellor's test case. In fig. 6.12b, the $\overline{uv}$ profiles on the concave wall of Monson's test case show similar behaviour where SSG produces higher mangitude of Reynolds shear stress spread across smaller height which shows less turbulent diffusion. LRR leads to lower $\overline{uv}$ than SSG with marginally higher diffusion than SSG. So, the level of $\overline{uv}$ of LRR model is smaller compared to other redistribution models. Compared to SSG and LRR, the SSG/LRR-ω leads to the right magnitude of Reynolds shear stress which gives a better agreement with the experiment in inner and outer parts of the boundary layer for the same diffusion models of turbulence transport in both test cases. Velocity profiles in figs. 6.10 and 6.12a suggest that SSG/LRR-ω has better agreement with the experiment compared to standalone SSG and LRR models.
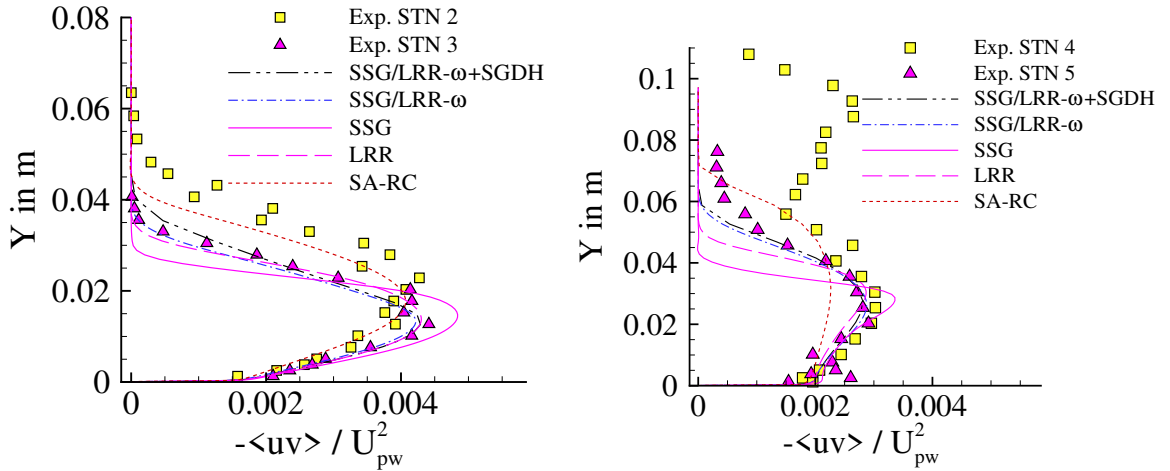
(a) Reynolds shear stress on concave wall at streamwise position, s = 1.78 m (stations 2,3 in exp.)

(b) Reynolds shear stress on concave wall at streamwise position, s = 2.44 m (stations 4, 5 in exp.)

Figure 6.11: Reynolds shear stress profiles of different redistribution models for So & Mellor's concave wall testcase in curved region

Effect of diffusion model in Transport term

Moreover, the diffusion model of turbulent transport term in Reynolds stress transport equation was modified to the Simple Gradient Diffusion Hypothesis (SGDH), to compare GGDH with SGDH. SSG/LRR-ω with SGDH leads to more diffusion in the concave boundary layer than SGDH. For position, s = 1.78m in fig. 6.10a, SGDH leads to slightly higher diffusion than GGDH but SSG/LRR-ω (with GGDH) has better match with the experimental data. This suggests that SGDH in turbulence transport term could be inducing more diffusion than required. For the streamwise position, s = 2.44 m in fig. 6.11b, it is difficult to conclude as none of the Reynolds stress models capture the diffusion of turbulent shear stress of the experimental data. More diffusion of turbulence transport term is necessary to accurately estimate turbulent shear stress for this streamwise position due to the effect of longitudinal vortices. In fig. 6.12b showing the concave region of Monson's testcase, similar behaviour is observed where SGDH gives marginally higher diffusion in the concave region and more diffusion of Reynolds shear stress is necessary for this position in U-duct.
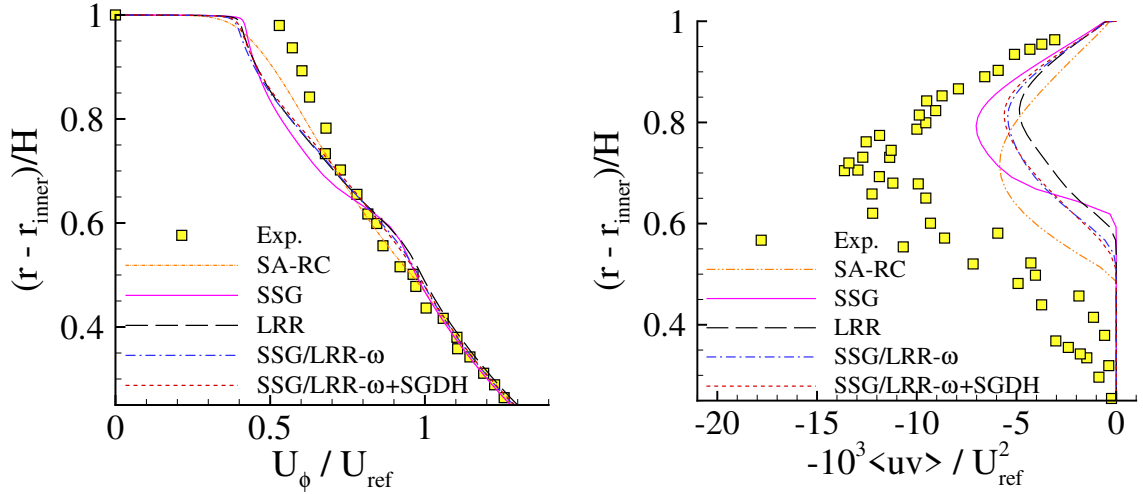
(a) Comparison of mean-velocity of different RSMs in U-duct at $\theta = 90°$

(b) Comparison of Reynolds shear stress of different RSMs in U-duct at $\theta = 90°$

Figure 6.12: Mean velocity and Reynolds shear stress of U-duct flow by Monson for different Reynolds stress re-distribution models and diffusion models for turbulent transport zoomed towards the concave region (outer wall)

6.3.2 Streamwise Evolution of Reynolds stress anisotropy in concave curved Boundary Layers
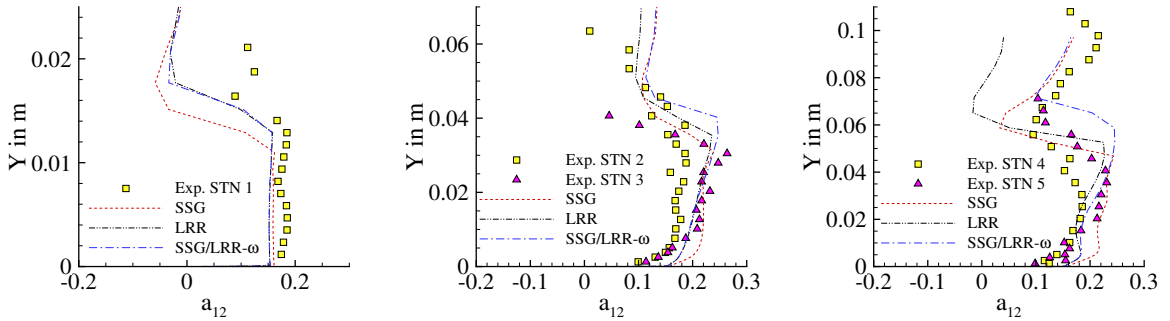
(a) Reynolds shear stress anisotropy (a_{12}) for station 1 (s = 0.61 m)

(b) Reynolds shear stress anisotropy (a_{12}) for station 2 and 3 (s = 1.78 m)

(c) Reynolds shear stress anisotropy (a_{12}) for station 4 and 5 (s = 2.44 m)

Figure 6.13: Streamwise evolution of Reynolds shear stress anisotropy using different redistribution models for So & Mellor concave test case

In fig. 6.13, anisotropy of turbulent shear stress is shown for different stations in straight and curved regions. From the experimental data of fig. 6.13, it can be inferred that a_{12} is constant in the wall-normal direction throughout the entire boundary layer approximately at 0.15-0.18 and becomes zero at the edge of boundary layer where the assumption of isotropic turbulence is valid. Similar to the Gillis & Johnston's experiment, the solution of different redistribution models produces almost constant anisotropy in the entire boundary layer $a_{12} \approx 0.15$ as shown in fig. 6.13a. But, in the curved region, due to the effect of concave wall, the anisotropic parameter stays positive and increases up to $a_{12} \approx 0.2$ and higher. This can be attributed to the destabilizing effect of concave curvature where turbulence production is increased to the centrifugal forces thus producing higher Reynolds

stress anisotropy as shown in figs. 6.13b and 6.13c. The increase of the magnitude of $\overline{uv}$ in concave curvature due to increased $\overline{vv}$ as described in Ref. [11] p. 164.

   The SSG model leads to more turbulence in the inner-part of boundary layer as shown in both curved region stations in fig. 6.13 compared to other redistribution models. In the outer-part of the boundary layer, even though SSG and SSG/LRR-ω have the same redistribution model, there exists marginal difference in variation of Reynolds stress anisotropy.

   From the experimental data of station 4 in fig. 6.13c, the structure of Reynolds stress anisotropy clearly represents the crest of a Taylor-Görtler vortex. In the centre region of a vortex, turbulent shear stress reduces due to strong stabilizing effect which is evident in fig. 6.11b(see Exp. STN 4 at Y = 0.06 m). Although the turbulent shear stress was almost zero above Y = 0.07 m in fig. 6.11b for all redistribution models, the Reynolds stress anisotropy suggests otherwise in fig. 6.13c. a_{12} of LRR model on the other hand turns to zero in the outer part of the boundary layer thus returning to isotropy while proceeding in wall-normal direction. But, SSG and SSG/LRR-ω increase in anisotropy and then decrease in the outer-part of the boundary layer and later again starts increasing (see fig. 6.13c). This behaviour of anisotropy of SSG and SSG/LRR-ω is closer to the experimental value of a_{12} although the actual values of $\overline{uv}$ are relatively very small. A deeper investigation needs to be done about the relative magnitudes of $\overline{uv}$ compared to turbulent kinetic energy in a 3D simulation which might reveal more information in this regard.

6.4   Implications for the modification of the SSG/LRR-ω for flows with significant streamline curvature

According to Zeman [56], a standard gradient diffusion hypothesis is not enough to accurately model the turbulent transport because it neglects the effects of mean-streamline curvature and rotation.

Implications for the convex wall

For the case of convex curvature without streamwise pressure-gradient (Gillis & Johnston's test case), the SSG/LRR-ω performs well compared to other redistribution models in estimating the turbulence structure and turbulence diffusion in the boundary layer. Moreover, for modelling the turbulence transport term, the Generalised Gradient Diffusion Hypothesis (GGDH) which uses the averaged wall-normal fluctuating component $\overline{vv}$ gives a much better agreement with the experiment compared to the Simple Gradient Diffusion Hypothesis (SGDH) which uses the Turbulent kinetic energy. For the case of convex curvature with streamwise adverse pressure-gradient (Monson's test case), more data is required at different streamwise positions in the curved region to understand the behaviour of pressure-strain correlation and turbulence transport models.

Implications for the concave wall

A large increase in turbulence was observed for the test cases of Monson and So & Mellor on the concave walls. The destabilizing nature of a concave curvature increases the production and diffusion of turbulence. There is a necessity for accurate experimental data at different spanwise and streamwise locations for validation; due to the formation of Taylor-Görtler vortices. For the case of So & Mellor, distinctive longitudinal vortices were observed at two spanwise locations. The amplitude of the Reynolds shear stress and the region occupied for the Reynolds shear stress is different at different spanwise locations.

   In So & Mellor's case, SSG/LRR-ω is found to be in good agreement with the turbulence structure that occurs in the crest of longitudinal vortex but not in the trough (which has stronger turbulence) region. The Reynolds shear stress anisotropy hints the structure of a longitudinal vortex for SSG and SSG/LRR-ω models in the outer-part of the boundary layer where the magnitude of $\overline{uv}$ is negligible. Anisotropic parameter, a_{12} could be useful in further modelling these effects in SSG/LRR-ω model. These effects of concave curvature are enhanced further with increasing magnitude of curvature

(δ/R). For Monson's case, a large increase of peak turbulent shear stress spread across larger wall-normal region is observed. Both turbulence production and diffusion needs to be increased for SSG/LRR-ω.

Chapter 7

Prospects for Curvature modifications to SSG/LRR-ω model

Based on the insights from section 6.4, few attempts were made to devise modifications to different terms in SSG/LRR-ω model which are elaborated in this section.

7.1 Modification of turbulent transport of Reynolds stresses

According to Zeman [56], in flow conditions where the production of Reynolds shear stress is weak, the turbulent transport term may control the balance and local level of Reynolds shear stress [45]. A closer look at the third moment terms is necessary [56].
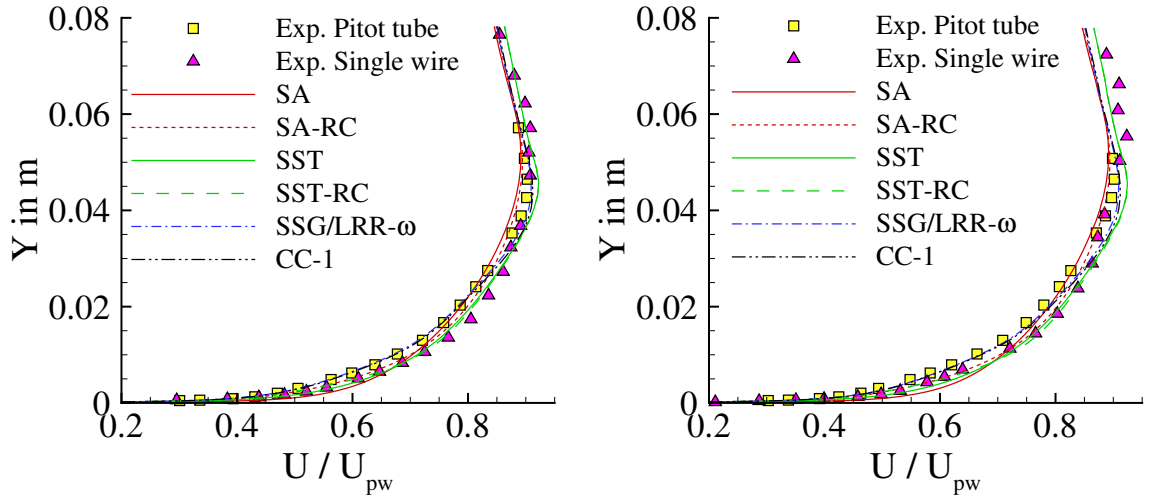
(a) Normalised mean-velocity for station 6 (s = + 50.8 cm)

(b) Normalised mean-velocity for station 7 (s = + 64.13 cm)

Figure 7.1: Normalised mean-velocity profiles at stations in curved region for Gillis & Johnston's test case to demonstrate the effect of curvature correction (CC-1) to SSG/LRR-ω for convex curvature with ZPG

The effect of rotation correction for SA, SST models slightly modifies the mean velocity profile especially in inner-half of the boundary layer by modifying the Reynolds shear stress. RC modifies

the turbulence production term directly for SA and SST models whereas for SSG/LRR-ω, curvature modifications were made to the transport term denoted as CC-1 as shown in figs. 7.1 and 7.2. For the case of convex curvature with ZPG, minor changes have been observed in the outer-part of boundary layer for Reynolds shear stress as shown in fig. 7.2. This resulted in a minute change for the mean-velocity profile shown in fig. 7.1.
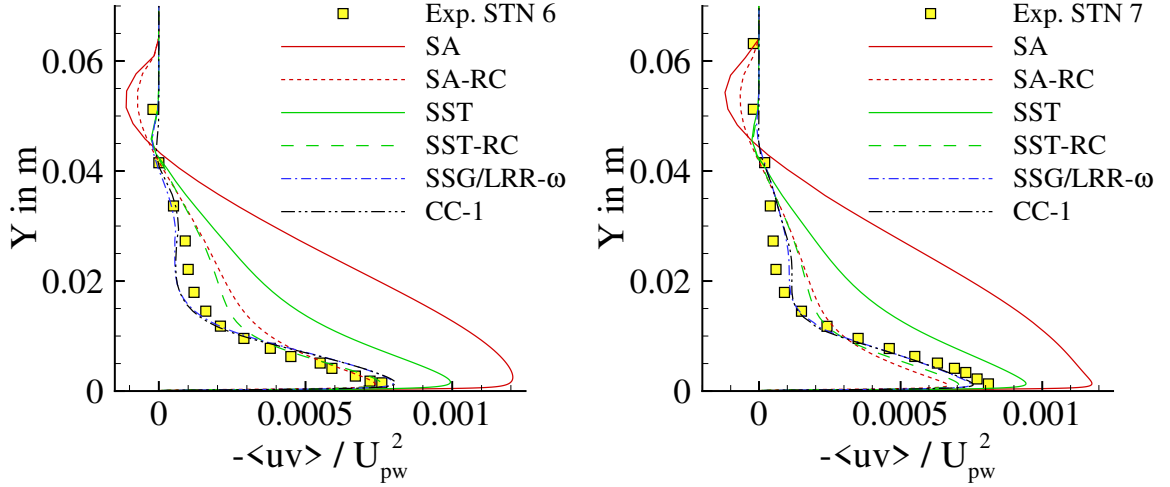
(a) Normalised Reynolds shear stress for station 6 (s = +50.8 cm)

(b) Normalised Reynolds shear stress for station 7 (s = +64.13 cm)

Figure 7.2: Normalised Reynolds shear stress profiles at stations in curved region for Gillis & Johnston's test case to demonstrate the effect of curvature correction (CC-1) to SSG/LRR-ω for convex curvature with ZPG
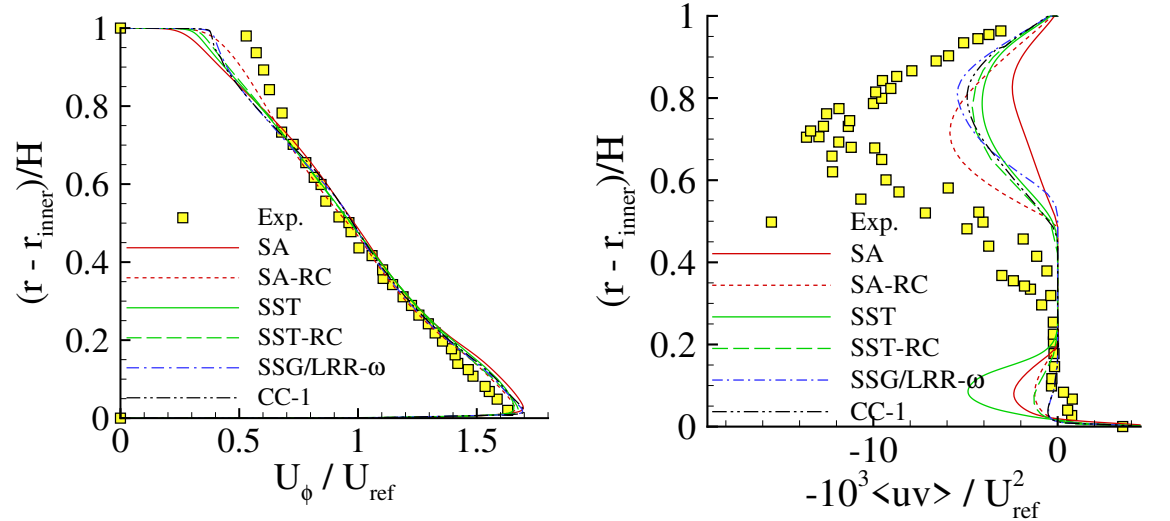
(a) Comparison of mean-velocity of different RSMs in U-duct at $\theta = 90°$

(b) Comparison of Reynolds shear stress of different RSMs in U-duct at $\theta = 90°$

Figure 7.3: Mean velocity and Reynolds shear stress of U-duct showing the effect of rotation-correction for different RANS models

For concave curvature, the modification of CC-1 was tested for the case of Monson's U-duct and the result of turbulent shear stress and mean-velocity at the 90° bend is shown in figs. 7.3b and 7.3a.

CC-1 increases diffusion in the concave boundary layer shown in fig. 7.3b. This is accompanied by reduction in the peak $\overline{uv}$ as the same amount of turbulence is being diffused into larger region by the action of turbulence transport term in the Reynolds stress model. The changes of CC-1 to the mean-velocity are only marginal on both concave and convex walls for the Monson's case shown in fig. 7.3a.

7.2 Trials to modify the length scale (ω) equation

Inspired from the rotation-corrections of SA-RC and SST-RC, trials were made to modify the production of turbulence shear stress. As the production term in Reynolds stress models is exact, the dissipation term of SSG/LRR-ω can be influenced by directly modifying the production term of length scale (ω) equation thus changing the turbulence production indirectly. Increasing the dissipation will suppress the turbulence production to balance the transport equation.

(a) Mean velocity profiles in U-duct at $\theta = 90°$ (b) Reynolds shear stress profiles in U-duct at $\theta = 90°$
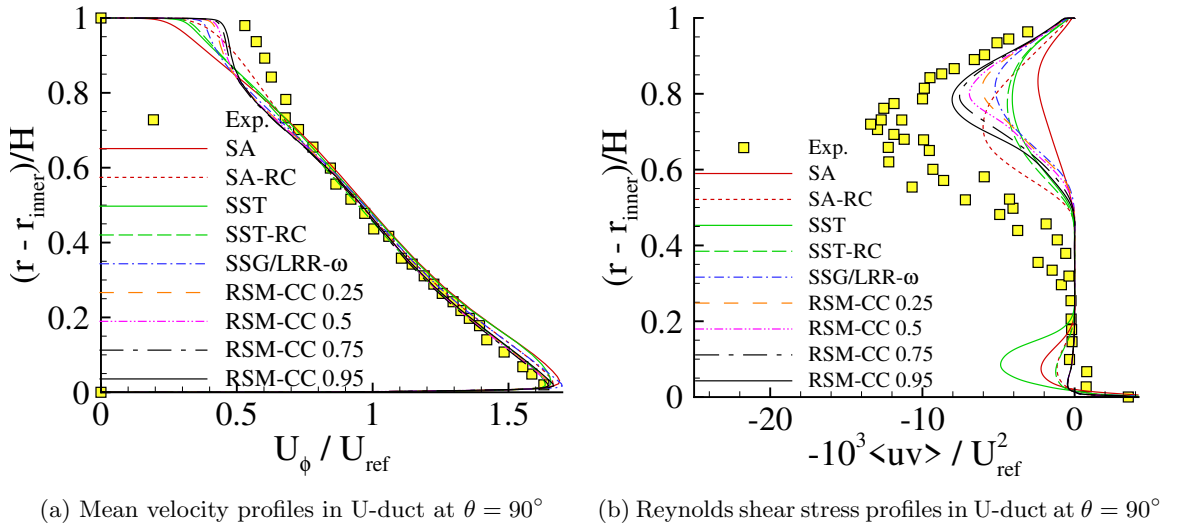
Figure 7.4: Mean velocity and Reynolds shear stress of U-duct showing the effect of trials to modify P_ω (Production term of ω equation)

Concave region of the U-duct was identified using the local Richardson number discussed in chapter 3. Trials were made to increase reduce the length scale but multiplying the production term of ω equation by a coefficient $= (1 - f_r)$ where the value f_r was modified with different values: 0.25, 0.5, 0.75, 0.95 thus giving the coefficient to the production of ω equation as: 0.75, 0.5, 0.25, 0.05 respectively. A constant coefficient was multiplied to the production of ω in the entire concave and convex regions as shown in eq. 7.1. By reducing the factor, production of ω equation i.e. P_ω is reduced. This reduces the magnitude of length scale ω there by reducing the dissipation of Reynolds stress, ε. As a result, the production of Reynolds stress should increase due to the reduction of dissipation. Results of these trials are shown in fig. 7.4 where RSM-CC-f_r shows different values. As a comparison, rotation corrections to other RANS models is shown in fig. 7.4.

$$P_\omega \rightarrow \begin{cases} (1 - f_r)P_\omega & \text{if } Ri_{local} < 0.0 \\ (1 + f_r)P_\omega & \text{if } Ri_{local} > 0.0 \end{cases} \tag{7.1}$$

In fig. 7.4b, the turbulent shear stress is increased in the concave region due the influence of length-scale production. But, the peak of $\overline{uv}$ still doesn't align with that of experiment like SA-RC does. This is because of multiplication of a constant coefficient to the entire boundary layer on concave wall. But, this aspect can be fixed by inducing more diffusion of turbulence in the boundary layer. However, the increase of Reynolds shear stress in the concave region shows a better agreement with the experimental values. The profiles of mean-velocity approach the experimental values with

increase in the f_r value of CC-f_r (see fig. 7.4b). By parameterizing this effect using a blending function, desired Reynolds shear stress can be achieved on the concave region. A coefficient which is a function of wall-distance or the local Richardson number directly would be a topic of interest for further research. A combined modification with both length-scale production and turbulence transport would be highly influential in modifying Reynolds shear stress on concave walls.

Chapter 8

Conclusion

8.1 Summary

A deeper investigation was conducted to understand and quantify the effects of streamline curvature in curved turbulent boundary layers. Bradshaw's work of gradient Richardson number which identifies the nature and magnitude of curvature was studied in detail to understand the zones of convex and concave curvatures for turbulence subjected to mean-streamline curvature.

This was used to further develop a Galilean-invariant version of Richardson number. Inspired from Hellsten's Richardson number, a grid-point local Richardson number Ri_{local} augmented by the direction information from the Spalart-Shur's rotation/curvature correction framework was derived. Different possible cases of Ri_{local} based on the nature of sign and relative magnitudes of curvature (U/r) and shear $(\partial U/\partial r)$ were elaborated to finalize the Galilean-invariant formulation for Ri_{local}. The behaviour of each Richardson number formulation was investigated by conducting a sensitivity study on the Monson's U-duct test case.

Suitable test cases from literature namely Monson (1990), Gillis & Johnston (1981) and So & Mellor (1972) were chosen and CFD setup was developed and validated from the experimental data. Using these validation test cases, the effects of rotation/curvature corrections to SA, SST model was understood and SSG/LRR-ω was validated for test cases with and without streamwise pressure-gradient. Different redistribution models for the pressure-strain correlation of RSM and different diffusion models for the turbulent transport term of RSM were compared for both convex and concave curvature test cases using the profiles of mean-velocity, Reynolds shear stress and anisotropy.

Prospects for curvature sensitsation of SSG/LRR-ω were explored. Turbulent transport term in SSG/LRR-ω was modified using the Galilean-invariant formulation of Richardson number Ri_{local} and the result of this modification was studied for the validation cases. Trials to modify the production of length scale ω equation (P_ω) were elaborated. Its effect on the dissipation of Reynolds stress thus changes to the turbulence production were examined. Insights into further modification of SSG/LRR-ω for complex flows were provided.

8.2 Conclusion

In the present work, the main objective was to further develop the Galilean-invariant formulation of Richardson number, to assess the predictive accuracy of the SSG/LRR-ω model with respect to wind tunnel experiments and to devise modifications to SSG/LRR-ω using the local Richardson number. The take-home messages from this work are as follows.

8.2.1 Study of Richardson number

- Support for the failure of $Ri_{Hellsten}$ for strong curvature was provided from the sensitivity study of Richardson numbers in chapter 5.

- The capability of Ri_{local} by Ströer & Knopp [46] for various curvature magnitudes was demonstrated.

- Ri_{local} is recommended for use as a flow feature in Machine Learning for improvement of turbulence models.

8.2.2 Situation and set-up of validation cases

The following conclusions can be drawn from the development of the validation test cases in the present work.

- Overall situation of various test cases:

  - Most of the suitable experiments for studying streamline curvature were performed before 1990s. There is a lack of recent experiments. For the case of turbulent boundary layers in APG, there are very few experiments until 1990 but has grown in the community since 2010.
  - Lack of DNS and LES data even for moderate Re flow conditions should be noted.

- Importance to consider different sources of uncertainties when comparing experiment data and simulation data:

  - Inflow conditions such as position of inlet boundary as the boundary layer thickness is larger than zero at the beginning of the test-section. As a remedy, the development length was modified in the CFD setup to match the experimental data of boundary-layer thickness, skin-friction coefficient etc at reference position upstream of the curvature region.
  - Definition of the geometry: For convex case, outer wall was adjusted to match the static-pressure distribution on the inner wall and vice versa for concave wall.
  - Uncertainty about effects of the spanwise side wall of the wind tunnel, in contrast to a 2D setup of the flow in the centre plane of the wind tunnel.

- Measurement errors:

  - In Gillis & Johnston's test case, different means of experimental techniques were used to measure the mean-velocity profiles in curved region. The pitot-tube measurements seem to be more accurate than the single-wire measurements.
  - For flow over concave walls, there is clear need to measure the mean velocity and Reynolds stresses at different spanwise positions (with a spacing accounting for the size of the Görtler vortices) and to carefully document the data at the different spanwise positions. For Monson's test case, the Reynolds shear stress profiles were only available at the 90° position. Moreover, significant influence of measurement accuracy on convex and concave walls is evident from the scatter of the Reynolds shear stress measurements (see fig. 6.1b). Although, this test case has a simple geometry for CFD setup, it is not suitable as a validation. This shortcoming in the experimental data by Monson seems to be in contrast with the observation that this case was widely used to validate several rotation/curvature corrections to RANS models such as SA-RC [36], SST-RC [38] (see Durbin's review paper [10]).

- Design of computational setup:

  - The geometries of the curved section of the test cases like Gillis & Johnston and So & Mellor are not readily available in the respective literature.
  - Geometries for CFD setup were developed from scratch using simple design tools based on iterative shape optimisation which are elaborated in the Appendix A.1.

- – In the experiment of Gillis & Johnston, the pressure drop at the onset of curvature i.e. streamwise static pressure-gradient dp/dx between the flat region and curved region was kept as low as possible by employing a special treatment of the opposite wall.

- – The attempts to expand the duct in the curved region to reduce static pressure changes are encountered with flow separation. Euler wall boundary condition could be used in CFD setup (see fig. 4.4) to avoid flow separation. The occurrence of flow separation brings problems for the method to determine the geometry. The form of separation region depends on the RANS model used, leading to different final geometries for different turbulence models. This issue can be reduced significantly if an Euler wall is used. One can either use the Euler wall boundary condition for some part of the curved outer wall or the entire outer wall depending on the conditions of the experiment.

- Part 1: Cases with convex curvature

  - – The test case by Gillis & Johnston is a suitable validation case, but requires development of the computational setup. A suitable computational setup was developed using shape-optimisation and validation using RANS models.

- Part 2: Cases with concave curvature

  - – So & Mellor's concave setup is a suitable validation case, but requires one to develop the geometry. This was successfully achieved.

  - – The situation in the wind tunnel is 3D with spanwise variation due to Görtler vortices. Measurements were only available at 2 stations in the curved region. But, the experimental data was very clear without any scatter.

  - – If the 2D RANS is compared to the minimum and maximum values of the Reynolds shear stress, it can observed that the dual peak structure of turbulent shear stress that occurs in a Görtler vortex is not captured by RANS models in the present work. Whether RANS models can simulate Görtler vortices is an open question that requires a 3D investigation.

8.2.3 Validation of RANS models in curved regions

- Part 1: Eddy viscosity models

  - – For the test case of Gillis & Johnston, SA-RC and SST-RC give similar results.

  - – For the concave wall in So & Mellor's test case, SA-RC has more pronounced effect on the increase of Reynolds shear stress than SST-RC. One reason is the limiters of RC modifications in SST-RC which is not used in SA-RC

- Part 2: Reynolds stress models

  - – Model ingredients of SSG/LRR-ω (modelling of turbulent transport term using Generalized Gradient Diffusion Hypothesis (GGDH), modelling redistribution using the blending of Launder-Reece-Rodi (LRR) and Speziale-Sarkar-Gatski (SSG) gave the best agreement with the experiment data compared to Simple Gradient Diffusion Hypothesis (SGDH) for transport and LRR, SSG for redistribution.

- Convex curvature

  - – For the case of Gillis & Johnston, SSG/LRR-ω gives better agreement with the experimental data than Eddy-viscosity models with rotation/curvature corrections in profiles of mean-velocity, Reynolds shear stress and Reynolds stress anisotropy (a_{12}).

- Concave curvature

  - – SSG/LRR-ω gives good agreement with Reynolds shear stress when compared to the experimental data from the trough region of a Görtler vortex where the effect of these longitudinal vortices is minimal.

– As a result of Görtler vortices, a double peak structure is formed in the Reynolds shear stress (see fig. 6.5b). This double peak structure representing a longitudinal vortex was not captured by any of Reynolds stress models or Eddy-viscosity based RANS models.

- The test case by Monson is not suitable for validation of RANS turbulence models due to a large measurement uncertainty, as seen in the scatter of Reynolds shear stress profiles.

- At the concave wall of the Monson's experiment, a large diffusion of Reynolds shear stress was observed but no structure suggesting the existence of longitudinal vortices (as observed for So & Mellor's experiment) was present.

8.3 Future scope

There are still several open questions in the present work which leaves scope for future researchers which are as follows:

- A direction sensor for Richardson number based on wall-normal gradients of total pressure is being developed. So, one can avoid the calculation of second derivatives of velocity for the Spalart-Shur's [43] rotation/curvature correction.

- New data generation using wind tunnel experiments for validation of RANS:

  – New data generated with state-of-art experimental measurement is required for curved turbulent boundary layer test cases with and without streamwise pressure-gradient i.e both APG and ZPG cases.

  – Measurements should be made at multiple locations upstream, at the onset of curvature, curved region at several (equally distant) spanwise locations to clearly observe and understand the effect of longitudinal vortices on concave walls.

  – It is better to have an aspect ratio of higher than 10 to avoid the effect of secondary flows in the test section.

  – Experiments with moderate to high Reynolds number are necessary to devise modifications to RANS models to equip them for accurate simulations of aircrafts.

- New data generation using scale-resolving simulations:

  – Scale-resolving simulations such as Direct Numerical Simulations (DNS) and Large Eddy Simulation (LES) are very expensive for high Re flow conditions.

  – There is a lack of DNS, LES validation data for flows with streamline curvature with and without streamwise pressure-gradient.

  – DNS of flow conditions with at least moderate Re(or high Re if possible) should be generated for high curvature and moderate curvature cases for both convex and concave walls. These are very essential in understanding the turbulence inside a vortex and modelling trailing vortices arising from aircraft wingtips.

- Three dimensional simulations of RANS models need to be performed to answer the question whether or not RANS models can capture Görtler vortices.

- In the So & Mellor's experiment, there are also convex constant-pressure and varying-pressure configurations which could be simulated for a deeper insight into pressure-strain correlation of Reynolds stress models.

Appendix A

Appendix

A.1 Gradient-based offline shape optimisation

In the present work, for the test cases of Gillis-Johnston and So-Mellor it was necessary to achieve a specific pressure-gradient on a fixed wall by increasing/decreasing the duct height. The locations of grid points representing the adjustable wall were moved in every design iteration. To reduce the C_P on the fixed wall, the duct height was reduced and vice versa. In each design iteration, it is difficult to manually estimate the amount to change required at a location based on the it's agreement with the pressure-distribution in experimental data. An offline calculation was performed by using the last two design iterations to modify shape for the next iteration.

$$\Delta D = \frac{\Delta D}{\Delta C_P}(C_P - C_P^{exp})$$
$$D^{n+1} - D^n = \frac{D^n - D^{n-1}}{C_P^n - C_P^{n-1}}(C_P^{exp} - C_P^n) \tag{A.1}$$
$$D^{n+1} = D^n + \frac{D^n - D^{n-1}}{C_P^n - C_P^{n-1}}(C_P^{exp} - C_P^n)$$

Here, 'D' be the height of the duct and superscript 'n' refers to the iteration. n, and n-1 represent the previous 2 iterations and n+1 represents the next iteration for which target curve is to be generated. The formula given in eq. A.1 is local to each grid point and can be used to apply changes to the x and y coordinates of a grid point separately as elaborated in eq. A.2.

$$x^{n+1} = x^n + \frac{x^n - x^{n-1}}{C_P^n - C_P^{n-1}}(C_P^n - C_P^{exp})$$
$$y^{n+1} = y^n + \frac{y^n - y^{n-1}}{C_P^n - C_P^{n-1}}(C_P^n - C_P^{exp}) \tag{A.2}$$

In a two-dimensional simulation, both coordinates can be altered after every iteration based on it's agreement with the target C_P curves from the experiment. The change at each grid point can be distributed at neighboring grid points increase the smoothness of the curves i.e. to avoid any discontinuities. In the present work eq. A.2 was used to obtain design suggestion for the next iteration. The x, y obtained from SA-RC, SST-RC and SSG/LRR-ω model were averaged to decide the curve for next iteration. So, the optimisation was done mainly using these 3 RANS models. The curve obtained from eq. A.2 was later imported into the Ponitwise mesh generation software to edit the mesh for the present test case. Example of a result of this technique is shown in fig. A.1 where the fixed wall onto which a certain desired C_P is obtained by modifying the adjustable wall. The pressure distribution at 2 previous iterations n and n-1 is required to calculate the n+1 curve using the simple gradient-based optimisation technique.
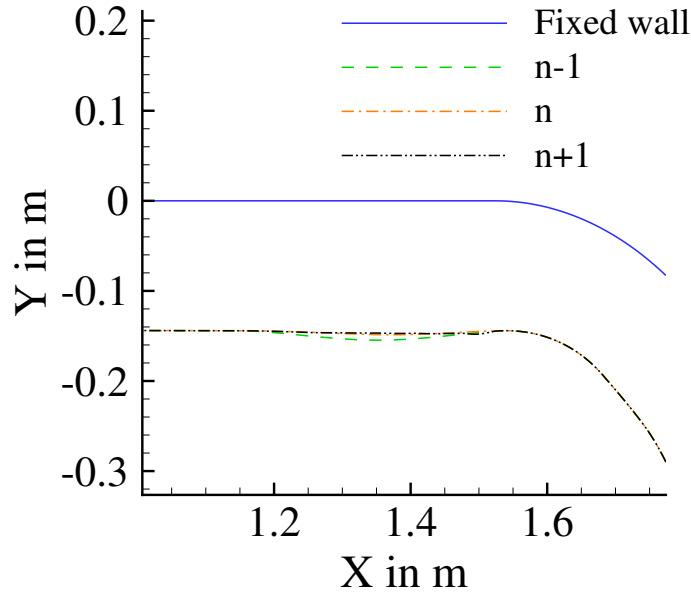
Figure A.1: An example showing fixed wall and the curve suggestion for the adjustable wall using gradient-based technique

A.2 Calculation of Potential flow velocity at wall for scaling

A proper scaling technique is required to compare different models with experiment in curved boundary layers. One can use the reference velocity to normalize the mean-velocity and turbulent shear stress. Outside of the boundary layer, inviscid region exists where the potential flow approximation is valid. In this region the effect of wall shear is negligible as a result the mean velocity is constant in wall-normal direction in the central region of the duct. Usually the boundary layer thickness is also calculated using the free-stream velocity i.e. constant in the potential flow region. Boundary layer thickness is decided when the mean-velocity reaches 99% of the potential flow velocity.

In straight section of a duct, the mean-velocity in the centre of duct or the free-stream velocity is constant in wall-normal direction in the potential flow region. When a line is drawn using these the points in the potential flow region, this line is perpendicular to the wall. But, in flows with mean-streamline curvature, this particular line is bend at a certain angle depending on the magnitude of the curvature. In fig. 5.2a, this can be observed for U-ducts with different radius of curvature.

A well-known scaling technique in curved boundary layers in literature is to use the potential flow velocity at wall. Irrespective of straight and curved regions, this technique can be used by drawing a line from the potential flow region on to the wall as shown in fig. A.2. In fig. A.2, mean-velocity is shown at station 6 (in curved region) obtained using SSG/LRR-ω model for the Gillis-Johnston's test case. The velocity at grid points above Y = 0.055 m was considered to perform a least-squares fit using the 'numpy.linalg.lstsq' function from the Linear Algebra library of Python-Numpy. The line obtained from the least-squares fit is extended on to the wall thus obtained the potential flow velocity at wall.

Another way to obtain the potential flow velocity at from Ref. [39] is by using an inviscid approximation given by the eq. A.3.

$$P_{total,\infty} = P_{static,\,wall} + \frac{1}{2}\rho U_{pw}^2 \tag{A.3}$$

For a duct, the total pressure (or stagnation pressure) remains constant throughout the entire duct particularly in the potential flow region. This constant total pressure along with the static pressure on the wall can be used to obtain the potential flow velocity at wall as shown in eq. A.3.

This technique is based on the inviscid approximation stemming from the Bernoulli's equation in fluid mechanics. Although, this is a simple technique, the method of least-squares fit is more robust and realistic to viscous flow. So, the least-squares fit of points in the potential flow region was used for both computational and experimental data in the present work.
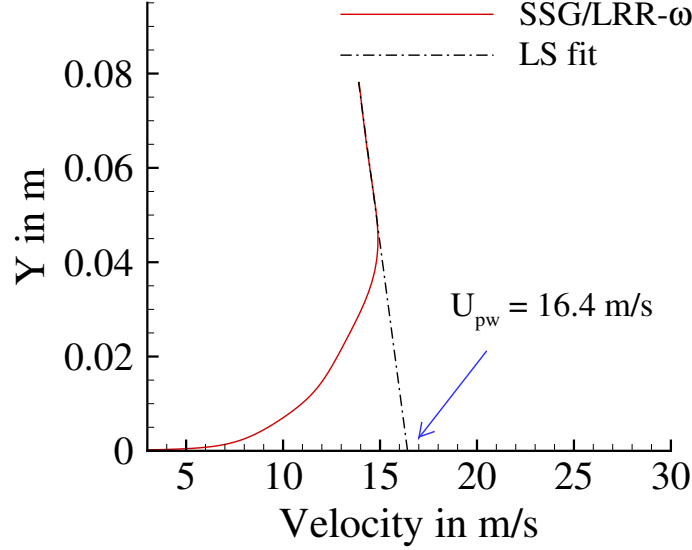

Figure A.2: Mean-velocity profile of Gillis-Johnston's test case at station 6(in curved region) calculated by SSG/LRR-ω model and U_{pw} calculation using the least-squares fit.

A.3 Modification of higher order correlations and their modelling

A.3.1 Turbulent diffusion of momentum

Usually, the Reynolds stress diffusive fluxes are assumed to be proportional to the gradient of respective Reynolds stress component. Two well-known models for gradient diffusion are SGDH and GGDH which are elaborated as follows.

Simple Gradient Diffusion Hypothesis (SGDH)

In SGDH, the diffusive coefficient is a scalar where the turbulent contribution is proportional to an equivalent eddy viscosity as shown in eq. A.4 [35].

$$D_{ij} = \frac{\partial}{\partial x_k} \left[\left(\nu + \frac{D}{C_\mu} \frac{k^2}{\epsilon} \right) \frac{\partial R_{ij}}{\partial x_k} \right] \tag{A.4}$$

Generalized Gradient Diffusion Hypothesis (GGDH)

In GGDH, the diffusion coefficient is a tensor where the turbulent contribution is proportional to the Reynolds stress tensor as shown in eq. A.5 [9].

$$D_{ij} = \frac{\partial}{\partial x_k} \left[\left(\nu \delta_{kl} + D \frac{k R_{kl}}{\epsilon} \right) \frac{\partial R_{ij}}{\partial x_l} \right] = \frac{\partial}{\partial x_k} \left[\left(\nu \delta_{kl} + D \frac{R_{kl}}{C_\mu \omega} \right) \frac{\partial R_{ij}}{\partial x_l} \right] \tag{A.5}$$

Consider the boundary layer approximation with largest gradients in the wall-normal direction. Assume that x_1 is in the wall-parallel direction and x_2 is in the wall-normal direction. (Loosely

speaking, x_2 is the radial direction and x_1 is the circumferential direction.) Then setting $k = l = 2$ yields

$$
\begin{aligned}
D_{ij} &= \frac{\partial}{\partial x_2} \left[\left(\nu \delta_{22} + D \frac{k R_{22}}{\epsilon} \right) \frac{\partial R_{ij}}{\partial x_2} \right] \\
&= \frac{\partial}{\partial x_2} \left[\left(\nu + D \frac{k \overline{v'^2}}{\epsilon} \right) \frac{\partial R_{ij}}{\partial x_2} \right] \\
&= \frac{\partial}{\partial x_2} \left[\left(\nu + D(k/\epsilon) \overline{v'^2} \right) \frac{\partial R_{ij}}{\partial x_2} \right] \\
&= \frac{\partial}{\partial x_2} \left[\left(\nu + D \tau \overline{v'^2} \right) \frac{\partial R_{ij}}{\partial x_2} \right]
\end{aligned}
\tag{A.6}
$$

with the turbulent time scale $\tau = k/\epsilon$.

Turbulent transport model by Zeman

Zeman starts with writing the unclosed second-order moment equation in cylindrical coordinates. Zeman studies the third moments T_{ijk} in the Reynolds stress equation. Zeman argues that in votex flow the turbulence production mechanism is weak, and that the turbulent transport becomes important. Moreover, he points out that third moment terms T_{ijk}/r, that are not in flux-divergence form, appear in the second-order moment equations. He writes that they can be important in the vortex core.

Zeman arrives at the following relation for the turbulent viscosity for the radial transport (in the r-direction) by considering linearized equations for fluctuating Lagrangian velocities

$$
\nu_{t,r} = \frac{c_1 \tau \overline{v'^2}}{1 + (c_2 \tau)^2 (K_z^2)'/2r^3}
\tag{A.7}
$$

Equation (A.7) can be seen as a modification of (A.6). Note that Zeman defines $\tau = q^2/\epsilon = 2k/\epsilon$, as $q^2 = 2k$. The prime ($'$) denotes the derivative in radial direction and $K_z = Ur = \Gamma/(2\pi)$ is the mean angular momentum in the z-direction, and c_1 and c_2 are adjustable constants that describe the relation between an effective time scale T_L associated with Lagrangian correlations arising in the derivation of (A.7) and the turbulence time scale $\tau = q^2/\epsilon$.

Then a gradient Richardson number is used as a streamline curvature parameter

$$
Ri_c = \frac{(K_z^2)'/r^3}{U'^2} = \frac{(K_z^2)'/r^3}{\left(\frac{\partial U}{\partial r} \right)^2}
\tag{A.8}
$$

It is worth to hold on for the moment and to compare this definition of Ri_c with the previous definitions

$$
\begin{aligned}
Ri_c &= \frac{(K_z^2)'/r^3}{U'^2} = \frac{\frac{\partial (U^2 r^2)}{\partial r} \frac{1}{r^3}}{\left(\frac{\partial U}{\partial r} \right)^2} = \frac{\left[2rU^2 + 2r^2 U \frac{\partial U}{\partial r} \right] \frac{1}{r^3}}{\left(\frac{\partial U}{\partial r} \right)^2} \\
&= \frac{2 \frac{U^2}{r^2} + 2 \frac{U}{r} \frac{\partial U}{\partial r}}{\left(\frac{\partial U}{\partial r} \right)^2} = 2 \left[\frac{\left(\frac{U}{r} \right)^2 + \frac{U}{r} \frac{\partial U}{\partial r}}{\left(\frac{\partial U}{\partial r} \right)^2} \right] \\
&= 2 \left[\frac{\left(\frac{U}{r} \right)^2}{\left(\frac{\partial U}{\partial r} \right)^2} + \frac{\frac{U}{r}}{\frac{\partial U}{\partial r}} \right] = 2[S^2 + S] = 2S(1+S), \quad S = \frac{\frac{U}{r}}{\frac{\partial U}{\partial r}}
\end{aligned}
\tag{A.9}
$$

Then we can proceed and study the formula for $\nu_{t,r}$ further. Substitution of (A.10) after rearranging as

$$
Ri_c \left(\frac{\partial U}{\partial r} \right)^2 = (K_z^2)'/r^3
\tag{A.10}
$$

into (A.7) yields

$$\nu_{t,r} = \frac{c_1 \tau \overline{v'^2}}{1 + (c_2 \tau)^2 \frac{1}{2} Ri_c \left(\frac{\partial U}{\partial r}\right)^2} \tag{A.11}$$

Note that Launder proposed the idea that the mean-flow time scale $[\partial U/\partial r]^{-1}$ can be replaced by the turbulent time scale $\tau = k/\epsilon$ in the nominator of the definition of Ri_c, as described in equation (25) in Hellsten. Using $\tau = k/\epsilon$ (without factor 2 due to the use of q^2 instead of k) yields

$$\nu_{t,r} = \frac{c_1 \tau \overline{v'^2}}{1 + (c_2 \tau)^2 \frac{1}{2} Ri_c \left(\frac{\partial U}{\partial r}\right)^2} = \frac{c_1 \tau \overline{v'^2}}{1 + c_2^2 \left(\frac{k}{\epsilon}\right)^2 \left(\frac{\partial U}{\partial r}\right)^2 \frac{1}{2} Ri_c} \tag{A.12}$$

In the last equation, the mean-flow time scale and the turbulent time scale might be canceled out and then only Ri_c arises in the denominator.

$$\nu_{t,r} = \frac{c_1 \tau \overline{v'^2}}{1 + c_2^2 \frac{1}{2} Ri_c} \tag{A.13}$$

Using $\tau = k/\epsilon$ in the nominator gives

$$\nu_{t,r} = \frac{c_1 \frac{k}{\epsilon} \overline{v'^2}}{1 + c_2^2 \frac{Ri_c}{2}}, \qquad \text{with} \quad Ri_c = 2S(1 + S) \tag{A.14}$$

Modification of the turbulent transport model by Zeman

The effect of curvature is scaling linearly with Ri_c. One might think that such linear relation is appropriate only for small values of Ri_c. For small Ri_c, the effects are described by

$$f = c_3^2 \frac{Ri_c}{2} \tag{A.15}$$

which needs modification for large values of Ri_c. For this purpose a modified transfer function $f(Ri_c)$ needs to be designed. Consider two extreme cases. For strong concave curvature, the parabola $Ri_c = 2S(1 + S)$ takes a minimum value of $Ri_c = -1/2$ at $S = -1/2$. For concave curvature, an increase of the turbulent transport is observed (see Arolla & Durbin [2]). For the present modelling, an increase corresponding to $1 + f(Ri_c) = 1 + c_{Dcc} = 0.33$ is assumed. For convex curvature, a reduction of the turbulent transport by a factor of 3 is assumed, corresponding to $1 + f(Ri_c) = 1 + c_{Dcv} = 3$. The third condition is $1 + f(0) = 1$.

$$\nu_{t,r} = \frac{c_1 \frac{k}{\epsilon} \overline{v'^2}}{1 + f(Ri_c)}, \qquad \text{with} \quad Ri_c = 2S(1 + S) \tag{A.16}$$

Bibliography

[1] Steven R Allmaras and Forrester T Johnson. Modifications and clarifications for the implementation of the spalart-allmaras turbulence model. In *Seventh international conference on computational fluid dynamics (ICCFD7)*, volume 1902. Big Island, HI, 2012.

[2] Sunil K Arolla and Paul A Durbin. Modeling rotation and curvature effects within scalar eddy viscosity model framework. *International Journal of Heat and Fluid Flow*, 39:78–89, 2013.

[3] Robert S Barlow and James P Johnston. Structure of a turbulent boundary layer on a concave surface. *Journal of Fluid Mechanics*, 191:137–176, 1988.

[4] P Bradshaw. The analogy between streamline curvature and buoyancy in turbulent shear flow. *Journal of Fluid Mechanics*, 36(1):177–191, 1969.

[5] Peter Bradshaw and AD Young. Effects of streamline curvature on turbulent flow. Agard Paris, 1973.

[6] Cadence : Fidelity pointwise cfd mesh generation software. `https://www.cadence.com/en_US/home/tools/system-analysis/computational-fluid-dynamics/pointwise.html`, 2024. Accessed: January 31, 2024.

[7] René-Daniel Cécora, Rolf Radespiel, Bernhard Eisfeld, and Axel Probst. Differential reynolds-stress modeling for aeronautics. *AIAA Journal*, 53(3):739–755, 2015.

[8] Jennifer Dacles-Mariani, Gregory G Zilliac, Jim S Chow, and Peter Bradshaw. Numerical/experimental study of a wingtip vortex in the near field. *AIAA journal*, 33(9):1561–1568, 1995.

[9] Bart J Daly and Francis H Harlow. Transport equations in turbulence. *The physics of fluids*, 13(11):2634–2649, 1970.

[10] Paul Durbin. Review: Adapting Scalar Turbulence Closure Models for Rotation and Curvature. *Journal of Fluids Engineering*, 133(6):061205, 06 2011.

[11] Paul A Durbin and BA Pettersson Reif. *Statistical theory and modeling for turbulent flows*. John Wiley & Sons, 2011.

[12] Alexandre Favre. Equations des gaz turbulents compressibles. *J. de Mecanique*, 4(3), 1965.

[13] JC Gillis, JP Johnson, RJ Moffat, and WM Kays. Experimental data and model for the turbulent boundary layer on a convex, curved surface. Technical report, NASA, 1981.

[14] JC Gillis and JP Johnston. Turbulent boundary-layer flow and structure on a convex wall and its redevelopment on a flat wall. *Journal of Fluid Mechanics*, 135:123–153, 1983.

[15] Henry Görtler. Instabilität laminarer grenzschichten an konkaven wänden gegenüber gewissen dreidimensionalen störungen. *ZAMM-Journal of Applied Mathematics and Mechanics/Zeitschrift für Angewandte Mathematik und Mechanik*, 21(4):250–252, 1941.

[16] Antti Hellsten. Some improvements in menter's k-omega sst turbulence model. In *29th AIAA, Fluid Dynamics Conference*, page 2554, 1998.

[17] Andrei Khodak and Charles Hirsch. Second-order non-linear k-ε models with explicit effect of curvature and rotation. In *Computational fluid dynamics' 96 (Paris, 9-13 September 1996)*, pages 690–696, 1996.

[18] D Knight and P Saffman. Turbulence model predictions for flows with significant mean streamline curvature. In *16th Aerospace Sciences Meeting*, page 258, 1978.

[19] Tobias Knopp, Nico Reuther, Matteo Novara, Daniel Schanz, Erich Schülein, Andreas Schröder, and Christian J Kähler. Modification of the ssg/lrr-omega model for turbulent boundary layer flows in an adverse pressure gradient. *Flow, Turbulence and Combustion*, 111(2):409–438, 2023.

[20] B.E. Launder and D.B. Spalding. The numerical computation of turbulent flows. *Computer Methods in Applied Mechanics and Engineering*, 3(2):269–289, 1974.

[21] Brian Edward Launder, G Jr Reece, and W Rodi. Progress in the development of a reynolds-stress turbulence closure. *Journal of fluid mechanics*, 68(3):537–566, 1975.

[22] Florian R Menter. Two-equation eddy-viscosity turbulence models for engineering applications. *AIAA journal*, 32(8):1598–1605, 1994.

[23] D Monson, H Seegmiller, and P McConnaughey. Comparison of experiment with calculations using curvature-correctedzero and two equation turbulence models for a two-dimensional u-duct. In *21st Fluid Dynamics, Plasma Dynamics and Lasers Conference*, page 1484, 1990.

[24] DARYL MONSON, HLEE SEEGMILLER, and PAUL MCCONNAUGHEY. Comparison of ldv measurements and navier-stokes solutions in a two-dimensional 180-degree turn-around duct. In *27th Aerospace Sciences Meeting*, page 275, 1989.

[25] KC Muck, PH Hoffmann, and P Bradshaw. The effect of convex surface curvature on turbulent boundary layers. *Journal of Fluid Mechanics*, 161:347–369, 1985.

[26] Nasa turbulence modeling resource. `https://turbmodels.larc.nasa.gov/`, 2024. Accessed: January 31, 2024.

[27] VC Patel and F Sotiropoulos. Longitudinal curvature effects in turbulent boundary layers. *Progress in Aerospace Sciences*, 33(1-2):1–70, 1997.

[28] Virendrakumar Chaturbhai Patel. The effects of curvature on the turbulent boundary layer. 1968.

[29] Ludwig Prandtl. 7. bericht über untersuchungen zur ausgebildeten turbulenz. *ZAMM-Journal of Applied Mathematics and Mechanics/Zeitschrift für Angewandte Mathematik und Mechanik*, 5(2):136–139, 1925.

[30] Ludwig Prandtl. Effect of stabilizing forces on turbulence. Technical report, 1931.

[31] BR Ramaprian and BG Shivaprasad. Mean flow measurements in turbulent boundary layers along mildly curved surfaces. *AIAA Journal*, 15(2):189–196, 1977.

[32] Osborne Reynolds. Iv. on the dynamical theory of incompressible viscous fluids and the determination of the criterion. *Philosophical transactions of the royal society of london.(a.)*, (186):123–164, 1895.

[33] William S Saric. Görtler vortices. *Annual Review of Fluid Mechanics*, 26(1):379–409, 1994.

[34] D. Schwamborn, T. Gerhold, and R. Kessler. Dlr-tau code - an overview. In *1st ONERA/DLR Aerospace Symposium, Paris, 21.-24. Juni 1999*, pages S4–2–S4–10, 1999. LIDO-Berichtsjahr=1999,.

[35] CC Shir. A preliminary numerical study of atmospheric turbulent flows in the idealized planetary boundary layer. *Journal of the Atmospheric Sciences*, 30(7):1327–1339, 1973.

[36] Michael L Shur, Michael K Strelets, Andrey K Travin, and Philippe R Spalart. Turbulence modeling in rotating and curved channels: assessing the spalart-shur correction. *AIAA journal*, 38(5):784–792, 2000.

[37] Anand Pratap Singh, Karthikeyan Duraisamy, and Ze Jia Zhang. Augmentation of turbulence models using field inversion and machine learning. In *55th AIAA Aerospace Sciences Meeting*, page 0993, 2017.

[38] Pavel E Smirnov and Florian R Menter. Sensitization of the sst turbulence model to rotation and curvature by applying the spalart–shur correction term. 2009.

[39] Ronald MC So and George L Mellor. An experimental investigation of turbulent boundary layers along curved surfaces. Technical report, NASA, 1972.

[40] Ronald MC So and George L Mellor. Experiment on convex curvature effects in turbulent boundary layers. *Journal of Fluid Mechanics*, 60(1):43–62, 1973.

[41] Ronald MC So and George L Mellor. Experiment on turbulent boundary layers on a concave wall. *Aeronautical Quarterly*, 26(1):25–40, 1975.

[42] Philippe Spalart and Steven Allmaras. A one-equation turbulence model for aerodynamic flows. In *30th aerospace sciences meeting and exhibit*, page 439, 1992.

[43] PR Spalart and M Shur. On the sensitization of turbulence models to rotation and curvature. *Aerospace Science and Technology*, 1(5):297–302, 1997.

[44] Charles G Speziale, Sutanu Sarkar, and Thomas B Gatski. Modelling the pressure–strain correlation of turbulence: an invariant dynamical systems approach. *Journal of fluid mechanics*, 227:245–272, 1991.

[45] Philip Ströer and Tobias Knopp. Curvature correction for turbulent diffusion inside a differential reynolds-stress model. In *STAB/DGLR Symposium*, pages 465–474. Springer, 2022.

[46] Philip Ströer and Tobias Knopp. General formulation of the gradient richardson number for rans modelling. In *AIAA SciTech 2023 Forum*, page 1801, 2023.

[47] Tecplot 360 ex software. `https://tecplot.com/products/tecplot-360/`, 2024. Accessed: January 31, 2024.

[48] Hendrik Tennekes and John Leask Lumley. *A first course in turbulence*. MIT press, 1972.

[49] DJ Tritton. Stabilization and destabilization of turbulent shear flow in a rotating fluid. *Journal of Fluid Mechanics*, 241:503–523, 1992.

[50] Milton Van Dyke and Milton Van Dyke. *An album of fluid motion*, volume 176. Parabolic Press Stanford, 1982.

[51] Henk Kaarle Versteeg and Weeratunge Malalasekera. *An introduction to computational fluid dynamics: the finite volume method*. Pearson education, 2007.

[52] Bert Vreman, Bernard Geurts, and Hans Kuerten. Realizability conditions for the turbulent stress tensor in large-eddy simulation. *Journal of Fluid Mechanics*, 278:351–362, 1994.

[53] Frank L Wattendorf. A study of the effect of curvature on fully developed turbulent flow. *Proceedings of the Royal Society of London. Series A-Mathematical and Physical Sciences*, 148(865):565–598, 1935.

[54] David C Wilcox. Reassessment of the scale-determining equation for advanced turbulence models. *AIAA journal*, 26(11):1299–1310, 1988.

[55] David C Wilcox et al. *Turbulence modeling for CFD*, volume 2. DCW industries La Canada, CA, 1998.

[56] O Zeman. The persistence of trailing vortices: a modeling study. *Physics of Fluids*, 7(1):135–143, 1995.